Università degli Studi di Napoli “Federico II”

DIPARTIMENTO DI INGEGNERIA INDUSTRIALE

Corso di Laurea Magistrale in
INGEGNERIA AEROSPAZIALE

Tesi di Laurea in *Aerodinamica degli Aeromobili*

Computational Study of an Isolated Proprotor and a Rough Tiltrotor Model in both Helicopter and Conversion Mode

Relatori

Ch.mo Prof. Carlo de Nicola
Ing. Paolo Caccavale
Ing. Michelangelo Giuliani

Candidato

Giuseppina Caizzo
M53/0862

Anno Accademico 2019/2020

Alla mia mamma,
al mio papà

[...]
Ma nei sentieri non si torna indietro.
Altre ali fuggiranno
dalle paglie della cova,
perché lungo il perire dei tempi
l'alba è nuova, è nuova.

(1948)

Rocco Scotellaro – *È fatto giorno*

Abstract

The pre-prototype stage of an airborne vehicle, manned or unmanned it might be, is of vital importance for its development. The evaluation of the aircraft flight mechanics and performance along the mission profile and in all the other situations that may occur within the flight envelope play a crucial role. In order to check whether the vehicle meets the safety requirements for the certification process and the customer demand at the same time, this preliminary design study cannot be overleapt. For instance, the engineering choice of including propellers as propulsion devices radically changes the analysis. The rotational blade motion has to be taken into account since it strongly affects the nearby fluid and thus the aircraft stability and performance. The fluid-flow field around a rotary wing is complex and its evaluation extremely tough due to a strong mutual dependence that exists between the spanwise blade load distribution and the vorticity distribution inside the fluid domain. For unsteady applications, such as those regarding a tiltrotor during conversion from helicopter mode to the turboprop-like configuration, the complexity is even greater.

Nowadays state-of-the-art numerical simulations in fluid-dynamics are represented by Computational Fluid Dynamics (CFD) methods, based on Reynolds Averaged Navier-Stokes equations. They provide an accurate estimation of the results thanks to the high level of detail the rotor wake is detected with. However, its resolution, along with the set-up, is so expensive in terms of computational speed and storage requirements that a direct numerical simulation based on computational fluid dynamics is unfeasible even employing parallel computing, even on a simplified or partial geometry.

A valid alternative way of investigating on the aerodynamic interaction of the propeller wake with the aircraft is supplied by the Vortex Particle Method (VPM): a technique based on the solution of the potential equations, hence in the assumptions of incompressible and inviscid flow. Ph.D. Eng. Paolo Caccavale has developed a new open-source 3D Boundary Elements Method (BEM) solver, called PaMS (Panel Method Solver) that models vorton wakes in panel methods. Then the solution *accuracy is the same as the latter, in addition body-wake interaction phenomena can be evaluated. And the relatively low impact of PaMS on the computational resources makes it particularly appropriate for unsteady multibody simulations which involve relative motions among the different geometries imported.*

The computational study that is going to be presented belongs to this category. Particularly, after an isolated V-22 Osprey proprotor model, the wing-proprotor configuration is analysed in the most delicate phase of a tiltrotor aircraft flight, i.e. when converting from helicopter to airplane mode.

Contents

Abstract

List of Figures i

List of Tables vi

Notation vii

List of Symbols viii

Acronyms xi

Chapter 1: Introduction

1.1 The Dream of Vertical Flight 1

1.1.1 Key Problems in Attaining Vertical Flight 2

1.1.2 Conventional Helicopters Limitations 3

1.2 Non-conventional Helicopters History 5

1.3 The Tiltrotor Concept 11

1.4 Present Dissertation 19

CHAPTER 2: Governing Fluid-Dynamics Equations

2.1 General Outline 21

2.2 Navier-Stokes Equations 22

2.3 Euler's Equations 25

2.3.1 Incompressible Constraint 26

2.4 The Vorticity Equation 27

2.4.1 Properties of the Vorticity Equation 28

2.5 Potential Flows 29

2.5.1 The Helmholtz Decomposition 29

2.6 Laplace and Poisson's equations 32

2.7 Unsteady Bernoulli Equation 34

2.8 Boundary Conditions 35

2.9 General Solution and Singularity Elements 39
2.10 Computation of the Velocity field 50
2.11 Computation of Forces and Moments 51
2.11.1 Trefftz technique 53

CHAPTER 3: Panel Methods
3.1 Synopsis 56
3.2 Numerical Procedure 56
3.2.1 Unsteady Panel Methods 63
3.2.2 Computation of velocities and forces 67
3.3 Vortex Particle Method 69
3.3.1 Formulation 70
3.3.2 Transformation of Wake Panels into Vortons 74
3.4 PaMS Code 77
3.4.1 Main Features 77
3.4.2 Settings 79
3.4.3 Workflow: an example 84
3.4.4 Wake modelling: key variables 85

CHAPTER 4: Propellers: Main Theories
4.1 Generalities and Definitions 91
4.2 Main Theories 94
4.2.1 Momentum Theory 94
4.2.2 Blade Element Momentum Theory 96

CHAPTER 5: An Isolated Proprotor Performance
5.1 V-22 Osprey Technical Specifications 98
5.2 Proprotor CAD Model 103
5.3 Geometry discretisation 104
5.4 Computational Analysis of an Isolated Proprotor in Helicopter Mode 106
5.5 Computational Analysis of an Isolated Proprotor in Pure Tilt Motion 113

CHAPTER 6: A Rough Tiltrotor

6.1 Wing Model and Meshing 120

6.2 Proprotor-Wing Interaction 123

6.2.1 Helicopter Mode 125

6.2.2 Conversion Mode 132

CHAPTER 7: A Design of Experiments

7.1 An UAV Tiltrotor: General Overview 139

7.2 *E-Pteron*: Overall Design 140

7.3 Bench Test 141

7.4 Ground Roll Test 144

Conclusions 146

PaMS DATAIN files

Appendix A – Case: Multibody in hovering flight **a**

Appendix B – Case: Multibody in pure tilt motion **c**

Computer Hardware Specifications **e**

References

Bibliography **f**

Webography **j**

Acknowledgements **k**

LIST OF FIGURES

1.1: Berliner's flying machine (on the left), Lehberger's project (on the right).

1.2: Baynes' patent (on the left), *Focke-Achgelis* FA-269 prototype (on the right).

1.3: Model 1-G tiltrotor aircraft by *Transcendental Aircraft Corporation*

1.4: XV-3 tiltrotor by *Bell Helicopter Company* (on the left), XV-15 by *Tiltrotor Research Aircraft* (on the right).

1.5: V-22 Osprey by *Bell Helicopter – Boeing Vertol*

1.6: *Bell-Agusta* BA-609.

1.7: V-270 Valor (on the left), QTR concept (on the right) by *Bell Helicopter*.

1.8: V-22 Osprey in different flight modes: (a) helicopter, (b) conversion, (c) airplane.

1.9: Rotor aerodynamic efficiency in forward flight.

1.10: Time evolution of helicopter cruise speed.

1.11: Hover – vertical lift efficiency as a function of disk loading

1.12: Comparison between Tiltrotors and Helicopters: payload as a function of range.

1.13: Maximum payload as a function of maximum range.

1.14: Time evolution of specific productivity evaluated on a 200 nm flight range.

1.15: Range specific transport efficiency as a function of unfueled range.

2. 1: Fluid domain in an *Eulerian* (conservative) approach.

2. 2: Logical scheme of a balance equation

2. 3: The fluid domain considered in the derivation of the Green's theorem.

2. 4: Scheme summarising the main fluid model

2. 5: Flow field at the wing trailing edge without (on the left) and with (on the right) the superimposition of the Kutta condition on the same aerodynamic body at the same angle of attack.

2. 6: Vortex line at a wing TE obtained by imposing the Kutta condition.

2. 7: Velocity potential and normal derivative near a solid boundary.

2. 8: Flow-field induced by a free stream.

2. 9: Flow-field induced by a point source (on the left) / point sink (on the right).

2. 10: doublet genesis from a sink and a source aligned (on the left) and flow-field induced by a point doublet (on the right).

2. 11: Flow-field induced by a point vortex.

2. 12: Quadrilateral constant-strength source element (on the left) and flow-field induced by it (on the right).

2. 13: Quadrilateral constant-strength doublet element (on the left) and flow-field induced by it (on the right).

2. 14: Quadrilateral doublet element and its vortex ring equivalent.

2. 15: Panel local reference frame for evaluating the normal and tangential velocity components.

2. 16: Trefftz plane.

2. 17: Velocities induced onto the Trefftz plane.

3. 1: Examples of discretised (thick – above – and thin – below) body and wake geometry

3. 2: Leakage flow that arises from discretisation issues.

3. 3: Influent coefficients: how they work.

3. 4: References for the Kutta condition in case of thick bodies (above) and thin ones (below).

3. 5: Numerical procedure to solve a steady surface singularity distribution problem.

3. 6: Numerical procedure to solve an unsteady surface singularity distribution problem.

3. 7: Creation of a rigid (above) and a flexible (below) unsteady wake.

3. 8: References for the wake panel indices.

3. 9: Computational scheme for the tangential velocity perturbation.

3. 10: Vortex tube and its corresponding vorton.

3. 11: Gaussian core function.

3. 12: Core function employed in PaMS.

3. 13: Flow field induced by a vorton: velocity decay along the vorton axis in red, velocity decay normal to the vorton axis in blue.

3. 14: Example of a vorton wake model (Willis' approach).

3. 15: DIAS vorton wake model. The area enclosed by the red line represents the integration zone employed to compute the vorton strength.

3. 16: Panel (on the left) vs vorton (on the right) wake.

3. 17: PaMS governing equations.

3. 18: PaMS code: a summary example of *DATAIN.dat* file.

3. 19: PaMS code: an example of *.geo* file.

3. 20: PaMS code: search of TE panels.

3. 21: PaMS code: workflow.

3. 22: Fixed wing: flexible (a) and rigid (b) wake models.

3. 23: Hovering rotor: flexible (a) and rigid (b) wake models.

3. 24: Hovering rotor: flexible (a) and 1 D.o.F (b) wake models.

3. 25: Fixed wing, vortex core effect: $r_c/b = 0.01$ (a), $r_c/b = 0.1$ (b), $r_c/b = 1$ (c), where b is the wing span.

3. 26: Hovering rotor, vortex core effect: $r_c/D = 0.01$ (a), $r_c/D = 0.1$ (b), $r_c/D = 1$ (c), where D is the rotor diameter.

4. 1: References for a blade element

4. 2: Propeller characteristic curves.

4. 3: actuator disk model for the simple momentum theory.

4. 4: References for the BEMT.

5. 1: V-22's salient design features and dimensions.

5. 2: V-22's rotor blade chord distribution (on the left) and twist distribution (on the right). Lengths non-dimensionalised to the rotor radius. [Original image is of poor quality].

5. 3: Isometric view of the CAD target proprotor [CATIA Wireframe & Surface Design].

5. 4: CAD proprotor blade [CATIA Wireframe & Surface Design].

5. 5: Single blade mesh, spanwise panel distribution [MSC Software Patran].

5. 6: Single blade mesh, streamwise panel distribution: detail view of the root section with highlighted mesh seeds (on the left) and the tip section (on the right) [MSC Software Patran].

5. 7: Cut-off effect: vorton wake of a proprotor after 15 revolutions with (a) no cut-off; (b) cut-off after 12 revolutions; (c) cut-off after 9 revolutions; (d) cut-off after 6 revolutions; (e) cut-off after 3 revolutions.

5. 8: Comparison between thrust coefficients: C_T based on PaMS results related to a fully free wake simulation with no cut-off and C_T evaluated from the USMC V-22 design weight.

5. 9: Cut-off effect on thrust coefficient. The Prandtl-Glauert correction for compressible flows has been applied to PaMS results.

5. 10: Comparison between thrust coefficients related to a fully free wake simulation with no cut-off: the pressure integral based C_T and the near-field Trefftz based C_T. The Prandtl-Glauert correction has been implemented.

5. 11: Radial (b) and axial (c) positions of vorton wake lines highlighted in (a) during the first revolution after the 6-panel near wake.

5. 12: Lift coefficient distribution along the blade span obtained by means of both pressure integrals and of the near-field Trefftz analysis. The Prandtl-Glauert correction has been implemented.

5. 13: Explanation of the motion law applied in Appendix B. In this layout the proprotor is represented by its actuator disk.

5. 14: Path of the V-22's rotor shaft during a 4-second tilting phase

5. 15: Time history of the proprotor centre position and of the angular displacement between the local and the global reference system

5. 16: Trajectory of a blade tip point in the global reference system during a 4-second tilting phase

5. 17: Time history of the force components acting on an isolated proprotor during a 4-second tilting phase.

5. 18: Velocity magnitude contoured vorton wake of an isolated proprotor in tilting phase at six different instants. The tilt angle θ_t refers to the ZZ_{ang} of Figure 5. 15.

6. 1: (from the top to the bottom) isometric view, front view and plan view of the CAD target rough tiltrotor [CATIA *Wireframe & Surface Design*].

6. 2: Wing mesh, spanwise (above) and chordwise panel distribution (below) [MSC Software Patran].

6. 3: wing-proprotor configuration, reference lengths for the settings.

6. 4: Wing-proprotor configuration, assembly meshes: at $t = 0\ s$ for the hover flight and transition motion simulations (above), at $t = 4\ s$ – end of the transition (below).

6. 5: Comparison between thrust coefficients: C_T based on PaMS results related to the isolated proprotor and to the rough tiltrotor; C_T evaluated from the USMC V-22 design weight. The Prandtl-Glauert correction for compressible flows has been applied to PaMS results.

6. 6: Schematisation of a tiltrotor flow-field.

6. 7: Gauge pressure distribution over the wing at the end of the hovering time ($t \approx 2.65\ s$).

6. 8: Axial-velocity-contoured vorton wake of a rough tiltrotor in hover flight at four different instants.

6. 9: Pressure-contoured vorton wake of a rough tiltrotor in tilting phase at eight different instants. The tilt angle θ_t refers to the ZZ_{ang} of Figure 5. 15.

6. 10: Pressure distribution contour on the wing upper surface (above) and on the wing lower surface (below) of a rough tiltrotor at the end of a tilting phase.

6. 11: Pressure profiles at highlighted wing sections (red – close to the root, blue – close to the tip) at the end of a tilting phase. Proprotor not depicted.

7. 1: E-Pteron's salient design features.

7. 2: Axial-velocity-contoured vorton wake of a 5-bladed propeller in hover flight.

7. 1: Time history of the force components acting on a 5-bladed propeller spinning at 1250 RPM during a 3-second tilting phase (wake cut-off at 100 time steps). Comparison with the axial force during a hover flight simulated at the very same revolutions per minute and same wake truncation.

7. 4: Schematisation of a ground roll test.

LIST OF TABLES

5. 1: V-22 Osprey technical specification.

5. 2: V-22 rotor system characteristics.

6. 1: Estimation of the pressure drag acting on the test case semi-wing due to the proprotor.

7. 1: E-Pteron's main technical specifications.

7. 2: Thrust force in hover flight at different angular speeds.

7. 3: Design parameters of the Epteron fore propellers: a proposal.

NOTATION

Before reading this document it is favourable to introduce some notations employed hereafter in this thesis.

At this purpose it has to be pointed out that the conventional index notation has been used, aiming to readability and simplicity. In this context the so called *Einstein summation convention* applies, so that repeated indices are implicitly summed over. For coherence with notation, the components of the position and velocity vectors are denoted by

$$\underline{x} = (x, y, z) = (x_1, x_2, x_3)$$

$$\underline{V} = (u, v, w) = (V_1, V_2, V_3)$$

respectively. In these statements the vector notation has been pointed out, too. In fact a vectorial quantity is denoted by means of an underlined font, whereas, in a similar fashion, the tensors are underlined twice (*e.g.* $\underline{\underline{\tau}}$).

LIST OF SYMBOLS

Symbol	**Name**	**Definition, Units**
Dimensionless Numbers and Coefficients		
C_p	Pressure Coefficient	$C_p = \frac{p - p_\infty}{q_\infty} = \frac{p - p_\infty}{\frac{1}{2}\rho_\infty V_\infty^2}$
C_P	Power Coefficient	$C_P = \frac{P}{\rho n^3 D^5}$
C_Q	Torque Coefficient	$C_Q = \frac{Q}{\rho n^2 D^5}$
C_T	Thrust Coefficient	$C_T = \frac{T}{\rho n^2 D^4}$, $C_T = \frac{T}{\rho A V_{tip}^2} = \frac{T}{\rho \pi \Omega^2 R^4}$
J	Advanced ratio	$J = \frac{V_\infty}{nD}$
M	Mach number	$M = \frac{V}{a}$
Re	Reynolds number	$Re = \frac{\rho V L}{\mu}$
Greek Symbols		
$\underline{\alpha}$	Vorton strength	m^3/s
α	Angle of incidence	deg
ϵ	Twist angle	deg
η	Efficiency	_
Γ	Circulation of a vector field, Vortex intensity, Dihedral angle	m^2/s m^2/s deg

γ	Vortex intensity per unit length/area/volume	m/s
Λ	Sweep angle	deg
λ	Taper ratio, $^{c_{tip}}/_{c_{root}}$	–
μ	Dynamic viscosity, Doublet strength	$Pa \cdot s$ m^4/s
μ_v	Bulk viscosity	$Pa \cdot s$
Ω	Angular speed	rad/s
$\underline{\omega}$	Vorticity vector	$1/s$
ϕ	Velocity potential	m^2/s
$\underline{\psi}$	Stream function	m^2/s
ρ	Density	kg/m^3
σ	Source strength, Vorton core radius	m^3/s m
$\underline{\underline{\tau}}$	Shear stress tensor	Pa
$\underline{\underline{\tau_d}}$	Deviatoric portion of $\underline{\underline{\tau}}$	Pa
θ	Pitch angle	deg
ξ_ψ	Core function	–

Roman Symbols

a	Laplacian sound speed	m/s
c	Chord	m
D	Drag, Rotor diameter	N, m
e	Internal energy	J/kg
$\underline{f_b}$	Body force	N/kg
k	Fourier's coefficient	$W/(m \cdot K)$
L	Lift, Characteristic length	N, m
n	Revolutions per minute	RPM

$\underline{n}$	Unit vector locally normal to a surface	m
N	Number of blades	_
p	Pressure	Pa
$\overline{r}$	Dimensionless radial coordinate, $^{r}/_{R}$	m
$\underline{r}$, r	Position vector, radial coordinate	m m
R	Gas constant, Rotor radius	$J/(kg \cdot K), m$
T	Temperature, Thrust	K, N
t	Time	s
$\underline{\underline{U}}$	Unit tensor	_
(u, v, w)	Velocity vector components	m/s
$\underline{V}$	Velocity vector	m/s
$\underline{x}$	Position vector	m
(x, y, z)	Position vector components	m
$y, \overline{y}$	Spanwise coordinate Dimensionless spanwise coordinate, $^{2y}/_{b}$	m, _

Subscripts and Superscripts

b	Body
∞	Far-field conditions
l	Lower side
t	Tilting phase
u	Upper side
w	Wake

ACRONYMS

BC	Boundary Condition
BEM	Boundary Element Method
BEMT	Blade Element Momentum Theory
CAD	Computer Aided Design
CFD	Computational Fluid Dynamics
DIAS	Department of Aerospace Engineering, University of Naples “Federico II”.
FFW	Fully Free Wake
JVX	Joint Vertical Experimental
LCTR	Large Civil TiltRotor
LE	Leading Edge
NACA	National Advisory Committee for Aeronautics
NASA	National Aeronautics and Space Administration
NRW	No Roll-up Wake
N-S	Navier-Stokes
OEI	One Engine Inoperative
OGE	Out of Ground Effect
PaMS	Panel Method Solver
PDE	Partial Differential Equation
P-G	Prandtl-Glauert
QTR	Quad TiltRotor
RHS	Right Hand-Side
SL	Sea Level
SOR	Successive Over Relaxation
TE	Trailing Edge
TRRA	TiltRotor Research Aircraft

USMC	U. S. Marine Corps
VPM	Vortex Particle Method
VSTOL	Vertical/Short Take-Off and Landing

CHAPTER 1

INTRODUCTION

1.1 The Dream of Vertical Flight

A rotorcraft is any flying machine that exploits rotating wings (*i.e.*, a rotor with blades that spin around a shaft) to create lift in absence of forward airspeed. This peculiarity allows rotorcraft either to hover and to take off and land vertically from almost any location, prepared or unprepared, and has often led to their classification as *runway independent aircraft*. In addition, to be practical, the machine must also be able to fly forward, climb, cruise at speed, and then descend and go back into a hover for landing. This dream of true flight has only been achieved in nature by hummingbirds and dragonflies. Over the years, Nature has inspired mankind: the idea of a flying machine with the capability of Vertical Take-off and Landing[1] attracted the interest of many inventors and designers which proposed numerous solutions characterised by a wide variety of lifting and propulsion devices.

Compared to fixed-wing aircraft, whose development can be clearly traced to Otto Lilienthal and the first fully controlled flight of a piloted powered aircraft by the Wright brothers in 1903, the origins of successful rotorcraft flight are considerably less clear. As a matter of fact, while the airplane was used extensively during WW1[2], it was not until the mid-1930s that helicopters become technically successful, and not until toward the end of WW2[3] that the first helicopters began to be manufactured in

[1] Commonly referred to by its acronym VTOL aircraft
[2] First World War
[3] Second World War

quantity. The long time lag, about thirty years, and the more turbulent evolution of rotary-wing aircraft, is a result of the greater depth of knowledge required before all the various aerodynamic and mechanical problems could be understood and overcome.

1.1.1 Key Problems in Attaining Vertical Flight

A few fundamental technical issues limited early experiments in attaining vertical flight. Firstly, the need to understand the basic aerodynamics of vertical flight and improve upon the aerodynamic efficiency of the helicopter. Although W. Rankine and R. E. Froude's thrusting rotor theories had been established by the end of the nineteenth century, the first significant application of aerodynamic theory to helicopter rotors came about in the early 1920s indeed. The lack of a suitable powerplant with high power-to-weight ratios was another problem not to be overcome until the beginning of the twentieth century by the development of internal combustion (gasoline) powered engines. Moreover, seeking for high-strength, low-weight materials for the rotor and airframe in order to minimise the structural weight was essential. Aluminium, commonly used on modern aircraft, was not available on the market until about 1890, but even then was inordinately expensive and not widely used in aeronautical applications until 1920. A primary concern was to provide stability and properly control the machine, devising a means of defeating the unequal lift produced on the blades advancing into and retreating from the relative wind when in forward flight. The solution came with the introduction of blade articulation in the form of flapping and lead/lag hinges and with the development of blade cyclic pitch control. With regard to directional control, on most early designs coaxial or laterally side-by-side rotor configurations were preferred, whereas the idea of a tail rotor to counter torque reaction was not used. Yet, building and controlling two rotors was even more difficult than only one. Other technical barriers included high vibrations as a source of many mechanical failures of the rotor and airframe, and which reflected an insufficient understanding of the dynamic behaviour of rotating-wings. As these key problems have been tackled during the last eighty years, the helicopter has grown from a rickety contraption that could barely lift its own weight into a modern and efficient aircraft of considerable engineering sophistication.

1.1.2 Conventional Helicopters Limitations

It is generally acknowledged that the *aerial-screw* designed by the Renaissance genius Leonardo da Vinci is the predecessor to the modern day helicopters, although the concept of vertical flight aircraft is already found in some Chinese toys of about 400 BC, known as Chinese tops, which consisted of feathers at the end of a stick, rapidly spun between the hands to generate lift and then released into free flight. Da Vinci's human-carrying helicopter-like machine (sketch dated to 1483 but first published nearly three centuries later) was an obvious elaboration of an Archimedes' water-screw, but with keen insight to the problem of flight and despite not having been able to take flight due to weight constrictions, it was far ahead of its time. Four men standing on a central platform should power the machine turning cranks to rotate the shaft *"with speed that said screw bores through the air and climbs high"*. Da Vinci realized that to produce enough lift to leave the ground the air-gyroscope rotor needed to be large enough, indeed he designed a diameter of 8 *braccia* (old Florentine unit of measure approximately equal to one arm's length, which translates roughly into a 6-meter rotor in diameter).

Many decades later, from the late 1940s this elementary intuition led to the definition of a parameter as the disk loading DL, commonly defined as the ratio of the thrust to the total main disk area over which it is produced. It allows to understand for a given VTOL aircraft the achievable level of efficiency in the production of the required thrust for hovering. In fact, VTOL aircraft that have a low disk loading will require low values of power per unit of thrust produced and thus become more efficient and consume less fuel with respect to same gross weight aircraft characterised by higher disk loading. It is straightforward that every time lower fuel consumption in hover flight or near-hover conditions is needed, aircraft with low disk loading represent a good solution. However, good performance also in cruise flight, with certain speed and range requirements, is demanded. The problem of designing an aircraft able to have good performance both in hover and in cruise flight at high speed was the major challenging task for the development of Vertical Take-off and Landing aircraft design. In this context, conventional helicopters should appear to be the right choice thanks to their large rotors which imply very low disk loading values. Actually the most common single main rotor layout with a tail rotor offer other many advantages, such as much flight flexibility, good endurance and extreme reliability, low empty weight fraction, low production and maintenance costs.

As known, the purpose of the main rotor in hover flight is to provide a vertical lift force to balance the weight of the rotorcraft, whereas in forward flight condition not only has it to provide a lift force to balance its weight but also a propulsive force to win the drag of the helicopter. It achieves this feat by bending the swashplate in the desired direction of flight. Consequently, the helicopter requires a great deal of power to reach high speeds while sustaining level flight. This is one of the factors that account for the helicopter's speed limitation and make it less suitable for all types of missions where airspeed and range are crucial, such as disaster relief, which is particularly needed in more remote parts of the world where airports may be sparse. Helicopters are rarely able to self-deploy because of their limited unrefuelled ranges, so in such cases they must be transported to the needed areas on ships or inside other aircraft. Other missions that require sustained cruise and maximum speed capabilities are usually poor in range efficiency especially when carrying significant payloads. In this regards, modern helicopters are able to fly in cruise at about 300 km/h with an operative range of about 800 km.

From a structural point of view, a shortcoming in conventional helicopters' forward flight performance comes with the torque limits on the main rotor shaft. The structural load limit reflects a strength versus weight design trade: the greater the shaft torque required to be transmitted, the greater the weight.

Also, the main rotor is affected by strong limitations of aerodynamic nature in forward flight due to an asymmetric velocity field. The main problems are related to the power losses given by compressibility effects on the outer part of the advancing blade with increasing forward airspeed, as well as the likelihood of stall on the main rotor retreating blade that occurs at high forward flight speed or during manoeuvres at high load factors. These are responsible for the production of negative effects on conventional helicopters performance that restrict the scope of their use and often result in trade-offs in their design.

1.2 Non-conventional Helicopters History

The story of the non-conventional helicopters is about innovation by a few people who sought to develop new designs capable of efficient vertical flight, like a helicopter, but with the ability to fly long distances at high speeds, comparable to the performance of fixed-wing aircraft. With the aim of finding an aircraft configuration which is able to overcome the limitations exhibited by conventional helicopters, in the late 1930s, the British Ph.D. J. Bennett issued a patent about his gyrodyne that, with the help of an auxiliary propulsion device and wings to unload the main rotor, managed to fly for the first time in 1954, and finally performed a complete transition from vertical to horizontal flight in March 1955.

Two decades later, the *McDonnell Aircraft Company* proposed the experimental compound XV–1 aircraft, which included a three bladed main rotor, low–mounted wings, and a pusher propeller at the rear to provide the thrust in forward flight. However, the project did not convince: the problem limiting the speed capability of the conventional helicopter in forward flight was still present.

The revolutionary *Lockheed* AH–56 Cheyenne model was proposed in the late 1960s in the frame of compound helicopters and, despite good performances in forward flight at over 407 km/h, the program was cancelled. Lately other high-speed compound helicopters have been developed. The experimental *Sikorsky* X2 model with coaxial rotors reached a speed of 460 km/h in level flight. The experimental compound helicopter X^3 Eurocopter became the World's Fastest Helicopter by reaching a speed of 472 km/h on June 2013.

Although the compound helicopter uses a conventional fixed-wing to produce the required lift in cruise flight mode, thereby unloading the rotor, it still encounters cyclical variations in rotor blade airloads while advancing and retreating at each rotation. Manoeuvre capabilities at high speeds are limited. In addition, the exposed rotor hub and control hardware contribute significantly to drag in high speed forward flight, further limiting maximum airspeed. The compound helicopter also suffered from the weight penalty of carrying the additional cruise mode propulsion system hardware. Collectively, these issues inhibit the performance potential of the compound helicopter that was not the answer to the search for a successful low disc loading VTOL high performance aircraft.

Some years before the Bennett's proposal, the need for an efficient VTOL aircraft led to the tiltrotor aircraft concept. At the beginning of 1920s, Henry Berliner proposed an innovative flying machine that was a fixed–wing biplane with two large diameter fixed–pitch propeller mounted on a vertical shaft at the tip of the upper wing. By tilting forward the shafts, the Berliner helicopter was able to achieve a flight speed of about 64 km/h.

Another design conceived ten years later to provide either vertical lift and forward flight was the G. Lehberger's *Flying Machine* which employed together for the first time the concept of tilting rotor with the low disk loading idea, but not developed any further.

In 1937 the British aeronautical engineer L. Baynes patented the *Heliplane*, a vehicle that looks like a modern tiltrotor aircraft. It employed large diameter propellers on tiltable wingtip mounted nacelles. Unfortunately, for inadequate financial backing, his innovative design never went beyond the patented concept, leaving the exploration of tiltrotor technology to other engineers in the four decades that followed.

In Germany, during the early years of World War II, a model of the *Focke-Achgelis* FA-269 started being fabricated, a trail-rotor convertiplane with pusher propellers that would be tilted below the wing for take-off. The mock-up was destroyed during a bombing raid and the project discontinued.

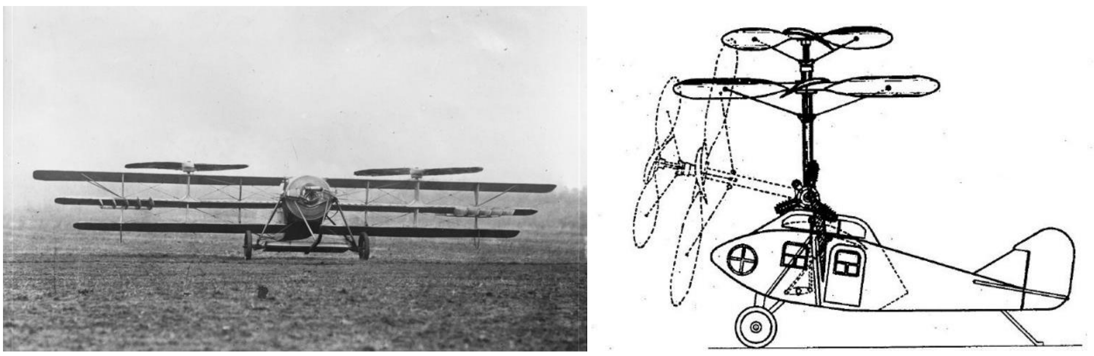

FIGURE 1. 1: Berliner's flying machine (on the left), Lehberger's project (on the right).

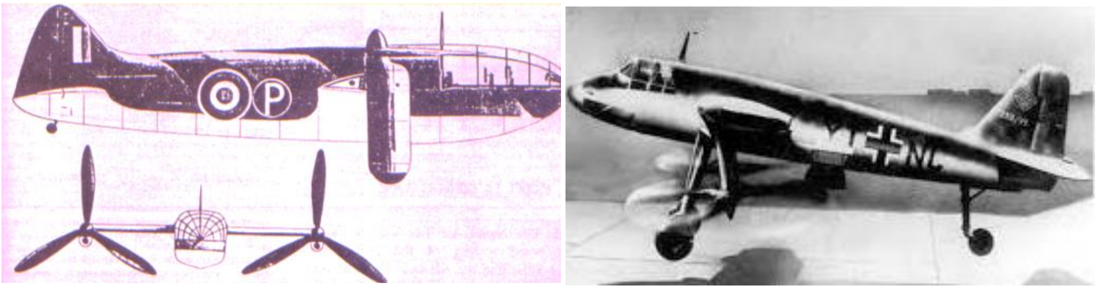

FIGURE 1. 1: Baynes' patent (on the left), *Focke-Achgelis* FA-269 prototype (on the right).

The next significant appearance of a tiltrotor design occurred in 1947 when the *Transcendental Aircraft Corporation* of New Castle, Delaware, proposed the *Model 1-G* tiltrotor aircraft. The experimental aircraft successfully completed more than 100 flights over just one year and it is commonly recognised as the first tiltrotor aircraft which has successfully explored the conversion flight mode. Unfortunately, the prototype met an unfortunate end, crashing on July 20, 1955 and despite its success, the project ceased in 1957 due to the withdrawal of funds by the U.S Air Force.

FIGURE 1. 2: Model 1-G tiltrotor aircraft by *Transcendental Aircraft Corporation*.

In that period, military requirements were strongly conditioning new aircraft design. For these reasons, in 1951 the U.S. Army together with U.S. Air Force started a joint research program to build new aircraft with convertiplane technologies. In a first instance, the XV–3 tiltrotor aircraft by *Bell Helicopter Company* was recognised to have the potential to overcome the main helicopter and compound helicopter limitations. It began its flight test program in 1955 but experienced severe vibrations during conversion to the airplane mode, resulting in a crash that destroyed the aircraft and seriously injured the pilot. Intensive analytical and experimental investigations were conducted by *Bell* and NASA[4] that revealed an aeroelastic instability which involved the rotor, the pylon and the wing. The XV-3 program faced a crisis and made even some supporters question about the readiness of this technology, but then a satisfactory solution was found by introducing a new hinged gimbaled rotor hub design with a pitch change mechanism and on December 18, 1958, it achieved to be the first aircraft to complete a dynamically stable full conversion to the airplane mode. Moreover, at the beginning of the 1970s the design of rotor blade became the objective of new studies. The experiments carried out on both isolated rotors and rotors installed on half–wings in the Ames Research Centre 40-by-80-foot wind tunnel provided a fundamental understanding of the physical phenomenon on the wing-rotor interaction and also represented a basis to develop the first numerical codes to predict tiltrotor aircraft performances.

In spite of the failure of the XV-3 to demonstrate the merits of the tiltrotor aircraft, supporters of the concept were convinced that its technical issues would eventually be resolved and it would meet predicted performance targets. To achieve those objectives, the rotorcraft industry (primarily the *Boeing Helicopter Company* and the *Bell Helicopter Company*) and government agencies (NASA, the Army and the Air Force) initiated focused research efforts involving design studies, analyses, wind tunnel tests and simulations that brought the TiltRotor Research Aircraft (TRRA) Project Office to life. The advantage of multiple participation became clear: in this way it was possible to maintain the project funding even when one agency was experiencing a temporary funding shortfall. The *Bell* XV-15 TRRA program first results were encouraging. As a remedy for the XV-3's speed limitations, it used high twist blades instead of blades designed for helicopter flight. Another significant element was the fabrication and bench tests of the new transmission gearboxes and cross-shaft system.

FIGURE 1. 3: XV-3 tiltrotor by *Bell Helicopter Company* (on the left), XV-15 by *Tiltrotor Research Aircraft* (on the right).

4 National Aeronautics and Space Administration

In 1983, *Bell Helicopter* together with *Boeing Vertol* started to work on a new and bigger tiltrotor aircraft. The *Joint-service Vertical take-off/landing Experimental* (JVX) aircraft program supported by the U.S. Department of Defence conduct the project of the V–22 Osprey tiltrotor aircraft, first tiltrotor which went into production. *Bell*, with its XV-15 experience, was responsible for the design of the wing, nacelles, rotors, drive system and tail surfaces. *Boeing*, having significant experience in composite materials, designed the fuselage and was also responsible for the V-22's cockpit, avionics and flight controls. Full-scale development was authorized in December 1986. The intended multiservice application of the V-22 imposed significant, and often conflicting requirements that influenced the design of the aircraft. Many accidents whose causes were disparate (charged to maintenance or pilot error), plagued the early years of the Osprey program, but none of them was specifically attributable to the tiltrotor concept; they nevertheless provided ammunition to the industries and delayed the improvements. Also in this case, many experimental and numerical studies were conducted. The results of these works led to a better understanding of the wing–rotor aerodynamic interaction, as for example the download effect in hover, the rotor– rotor interaction in the proximity of the aircraft symmetry plane and the presence of the fountain effect.

FIGURE 1. 4: V-22 Osprey by *Bell Helicopter – Boeing Vertol.*

In 1998 the continuous improvements in tiltrotor technologies and the market expansion to the civil aviation gave rise to the *Bell–Agusta* BA609 project, turned into the *AgustaWestland* AW609 project in 2009. Certification of this new aircraft type presented challenges with the regulatory agencies requiring the aircraft to meet helicopter, fixed-wing and new tiltrotor criteria. Generally configured as the V-22, it is the world's first civil tiltrotor. The military certification be hopefully achieved by the end of 2021.

FIGURE 1. 5: *Bell-Agusta* BA-609.

In 2013 *Bell Helicopter* proposed a third-generation tiltrotor V-280 Valor for the Future Vertical Lift (FVL) Program. Unlike the XV-15, the V-22 and the AW-609, the Valor wing is not swept forward and the rotor only tilts, not the engine.

Even though over the last sixty years the tiltrotor design has been an improvement of the initial know-how developed within the XV-3 program, it does not lack alternative configurations and applications. Among these it is possible to cite the Quad TiltRotor (QTR), a four-rotor derivative of the V-22 developed jointly by *Bell Helicopters* and *Boeing*. This ambitious concept – in development since the 1999 – is intended to have a cargo capacity roughly equivalent to the C-130 Hercules, to carry ninety passengers and to cruise at 460 km/h.

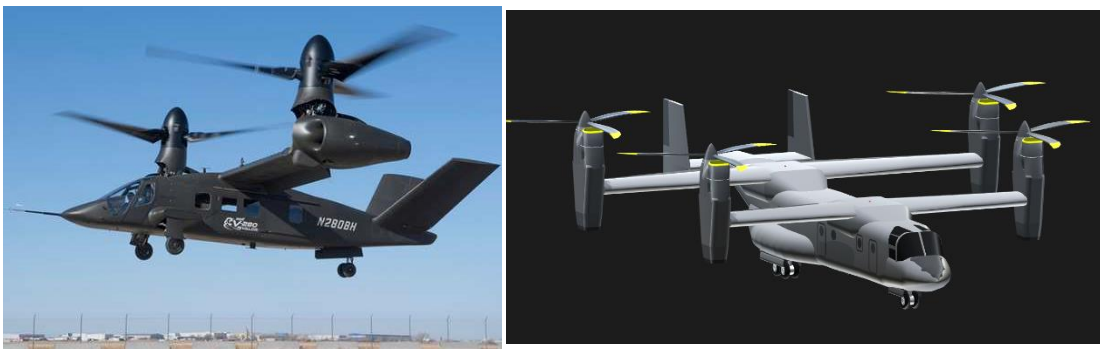

FIGURE 1. 6: V-270 Valor (on the left), QTR concept (on the right) by *Bell Helicopter*.

1.3 The Tiltrotor Concept

The potential of a tiltrotor configuration to revolutionise air transportation, overcoming conventional helicopters drawbacks and bridging the gap between those and fixed-wing aircraft, by matching the peculiarities of both has already been mentioned in the previous section. This paragraph provides limited, but pertinent information relative to the technical viability of the tiltrotor configuration evaluated in terms of potential missions and by performance comparisons with other aircraft configurations in order to place emphasis on identification of complexity differences – which normally impact acquisition and/or operating costs – and thus, of the market segment to whom the product could be attractive. The market potential for civil VTOL aircraft is driven by the ever increasing congestion at major air traffic hubs and ground transportation to/from those airports, aggravated by the fact that both short-haul and long-range aircraft share the same runways, the same approach control systems and the same standard departure procedures[5]. On the other hand, the combination of VTOL capabilities with relatively high cruise speeds and long range could seem to be the answer to military multi-missions.

The most common layout that has been object of research through the years is the *twin-tiltrotor design* and this will be the layout to refer to throughout the present work. It consists of two counter-rotating proprotors, carried by a rotornacelle each that houses powerplant, transmission and pitch control components. The rotornacelles are pivotally mounted about a spanwise axis at the wing tips and according to their position, three flight modes are possible (see Figure 1. 7), providing a great versatility to the convertiplane.

Helicopter mode. The rotor shaft is aligned vertically, then the tiltrotor lifts and hovers the way a normal helicopter does. Also forward flight at moderate speeds can be performed by tilting the swashplate in the desired direction. The collective and cyclic pitch control occurs likewise.

5 This is one of the main reasons which are pushing the NASA to develop the so called LCTR (Large Civil TiltRotor)

Conversion mode. This flight mode refers indistinctly to any degree of nacelle tilt the aircraft can fly at, between the vertical and the horizontal position. The shaft is pivoted towards the front of the fixed wing in order to switch from helicopter mode to airplane mode. On the V-22, the minimum time to accomplish a full conversion from hover to airplane flight mode is 12 seconds. As the tiltrotor starts gaining forward speed to between 75 and 150 km/h, the wing begins to produce lift too and the ailerons, elevator and rudder become effective. At this point, rotary-wing controls are phased out by the automatic flight control system that manages transitions between the three flight modes. At approximately 180 to 220 km/h, the wing is fully effective and the cyclic pitch control of the proprotors is locked out. The conversion from airplane flight to a hover simply reverses the process described. As speed decreases, the rotor-borne lift starts compensating the decrease in wing lift.

Airplane mode. It is identified by the rotor shaft arranged horizontally, making the proprotors act as propellers. The tiltrotor functions exactly like a conventional propeller aircraft. Controls utilised are the ailerons, rudder and elevator.

FIGURE 1. 7: V-22 Osprey in different flight modes: (a) helicopter, (b) conversion, (c) airplane.

The term *proprotor* comes from not being quite as a helicopter rotor and an airplane propeller either. Proprotors are aerodynamically designed to function effectively like both, resulting in a trade-off between efficient hover and flight. Their blades are characterised by high degrees of twist like propellers, but much larger in diameter. Consequently, a proprotor can generate the same amount of thrust as a propeller at much slower RPM[6]: the lower tip speed makes the tiltrotor particularly quiet in cruise flight. Yet due to obvious reasons of interference between the proprotors and the ground, the CTOL[7] capability is limited. Since the blades are designed to optimise the horizontal flight rather than the vertical one, the tiltrotor seeks to be less expensive in terms of fuel consumption compared to the conventional helicopter. In other words, with the same tank capacity, the range of a tiltrotor is greater. The aerodynamic efficiency (*i.e.* the lift to drag ratio) in forward flight is reported in Figure 1. 8 for both the helicopter and the tiltrotor (data referred to the *Bell* XV-15).

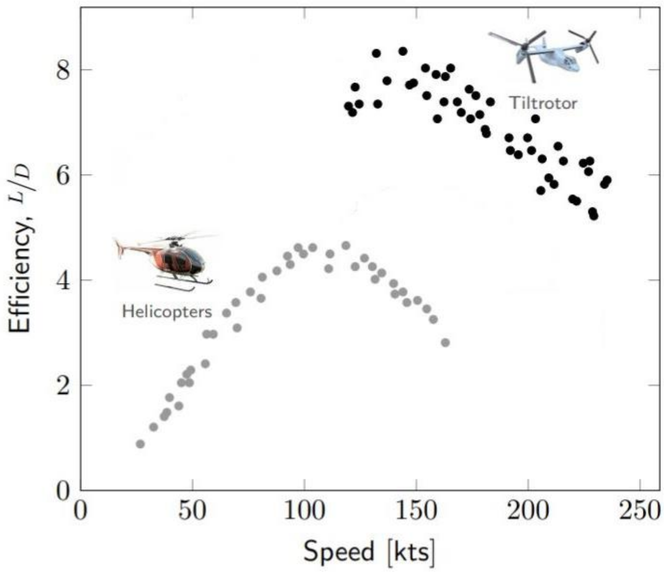

FIGURE 1. 8: Rotor aerodynamic efficiency in forward flight [Johnson, 2013].

Figure 1. 9 underlines the speed advantage of the tiltrotor over the VTOL niche ruler. It could be observed that the gain in speed for a helicopter has been following a decreasing trend through the years which means the reach of a technological barrier, from this point of view, that cannot be broken without employing more innovative technologies or concepts. On the same graph, the *Bell-Boeing* V-22 Osprey (that can be considered the actual state of the art among tiltrotors) demonstrated cruise speeds 35% – 50% faster than a modern helicopter. Nonetheless at that velocities, the

[6] Revolutions per minute
[7] Conventional Take-Off and Landing

productivity ratio of the tiltrotor gives a gain of only 25% over the helicopter at a radius of action of 350 km.

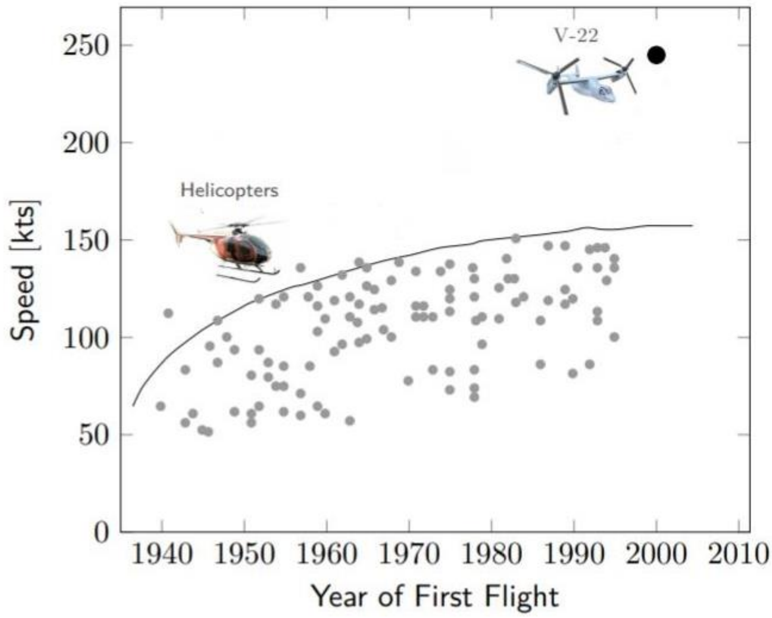

FIGURE 1. 9: Time evolution of helicopter cruise speed [Leishman, 2007].

However, being a hybrid concept, the tiltrotor aircraft is not as aerodynamically efficient as a helicopter in hovering flight nor as a turboprop in forward flight. Due to the fact that proprotors are not as large as rotors, the disk loading is greater and then the hovering efficiency not as high as that of a conventional helicopter (Figure 1. 10). Therefore, it becomes less attractive for missions that involve longer hovering times or for extended flights at low airspeeds, which is where a helicopter is much more efficient[8]. Moreover, the hovering performance and the lifting capability of the tiltrotor is strongly affected by the aerodynamic interaction between wing and proprotors. In helicopter flight mode, the proprotor is only about one wing chord above the wing, so the flows induced by the wing and the proprotors are closely coupled. The presence of the wing under the proprotor significantly modifies the rotor wake and thus is responsible for the loss of rotor performance. In addition, impingement of the rotor

[8] In the design of the Bell-Boeing V-22 Osprey, the proprotor diameter was also limited by the need to operate and hanger the aircraft on board an aircraft carrier.

downwash on the wing causes a download on the wing, which reduces the payload carrying capability of approximately 10% – 15%.

Tiltrotors are not going to replace helicopters as load carriers either: as appears to be clear from Figure 1. 11, the Osprey can carry only about half the payload of the *Sikorsky* CH-53E, irrespective of the range. Furthermore the same picture points out that the V-22 experiences a considerable loss in performance when operating at high altitudes (*i.e.* in low density conditions), and that this loss is even greater than that relative to a medium weight utility helicopter such as the UH-60 Blackhawk. In fact, despite being able to carry a heavier payload at MSL[9], the V-22 is outperformed by the Blackhawk in hot and high conditions.

Compared to fixed-wing aircraft, a tiltrotor has to carry a great deal of fuel to cover long distances. Since this amount of fuel erodes the payload that is possible to carry, maximum range and maximum payload form a trade-off pair. Figure 1. 12 highlights the fact that the V-22 Osprey has almost the same performance as the average helicopter. Note that a helicopter can be designed to carry a significant useful load over short distances by trading against fuel capacity, or a smaller payload over higher ranges by using long-range fuel tanks. Those two extreme points are aligned along a bounding line representing the technological limit of the conventional helicopters. The point related to a carrier aircraft such as the *Lockheed* C-130J is above this bounding line, meaning that cargo planes are almost peerless in high range transportation of heavy payloads.

[9] Mean Sea Level

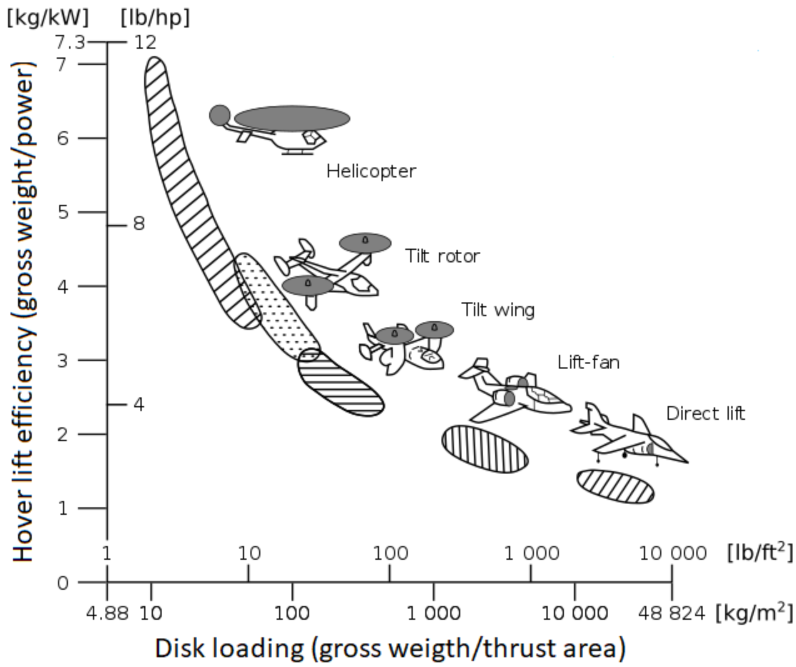

FIGURE 1. 10: Hover – vertical lift efficiency as a function of disk loading.

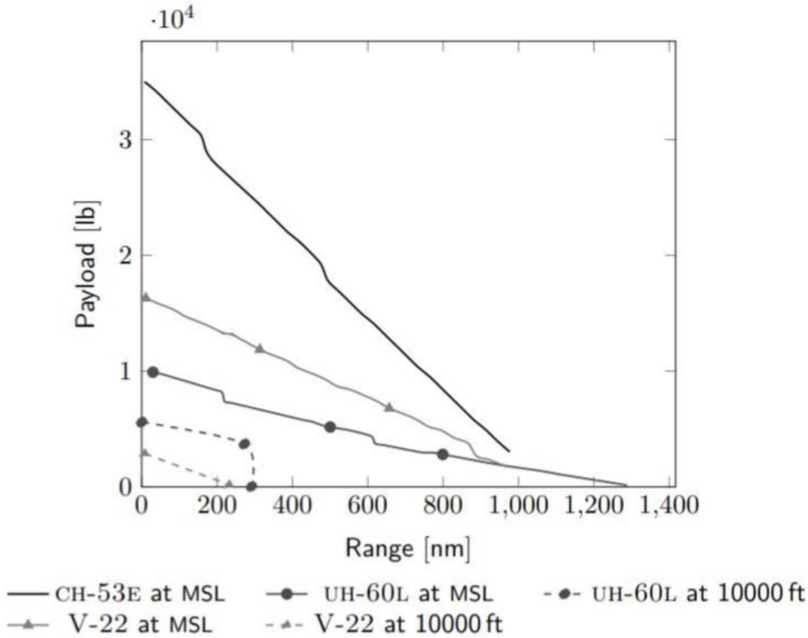

FIGURE 1. 11: Comparison between Tiltrotors and Helicopters: payload as a function of range [Leishman, 2007].

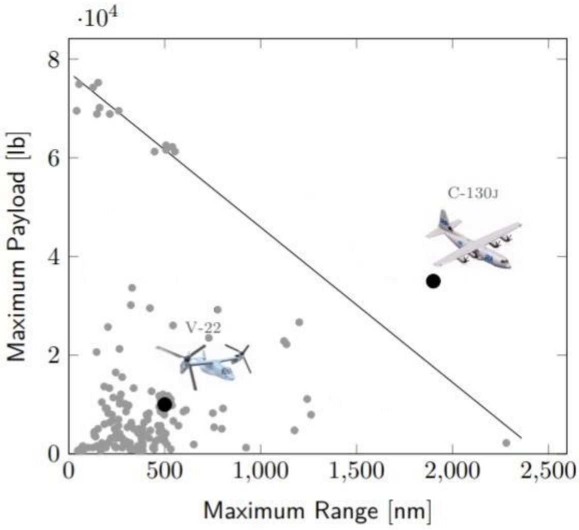

FIGURE 1. 12: Maximum payload as a function of maximum range [Leishman, 2007].

The carried payload and the speed of transportation can be merged in just one parameter: the *specific productivity*, defined as the ratio of the maximum payload transported (over a given distance) times the speed of transportation to the maximum take-off weight of the aircraft,

$$specific\ productivity = \frac{maximum\ payload\ \cdot\ speed}{maximum\ takeoff\ weight}.$$

Specific productivity data in terms of a 200 nm (370 km) stage distance are reported in Figure 1. 13, where the asymptotic trend confirms the reach of technical barriers limiting helicopters' productivity. With regard to the V-22, its ability to cruise up to 50% faster than a modern helicopter is nearly all offset in terms of its specific productivity by both its relatively lower payload capability and its relatively higher empty weight. As a consequence, the tiltrotor (at least in its actual configuration) is again comparable to the average helicopters – thus not the answer to improve vertical-lift productivity – and it is outperformed by the classical fixed-wing airplane.

Aside to the specific productivity ratio, it is possible to define another parameter that takes into account the fuel consumption: the *range specific transport efficiency*, defined the payload weight transported over the fuel weight consumed for a specific transport range,

$$range\ specific\ transport\ efficiency = \frac{payload\ weight}{fuel\ weight}.$$

Figure 1. 14 emphasise how less efficient the helicopter concept becomes, the longer the flight range is and that current tiltrotors do not exceed their capabilities for the typical transportation missions. In fact both the specific productivity and the transport efficiency of the V-22 Osprey are no better than those of conventional helicopters.

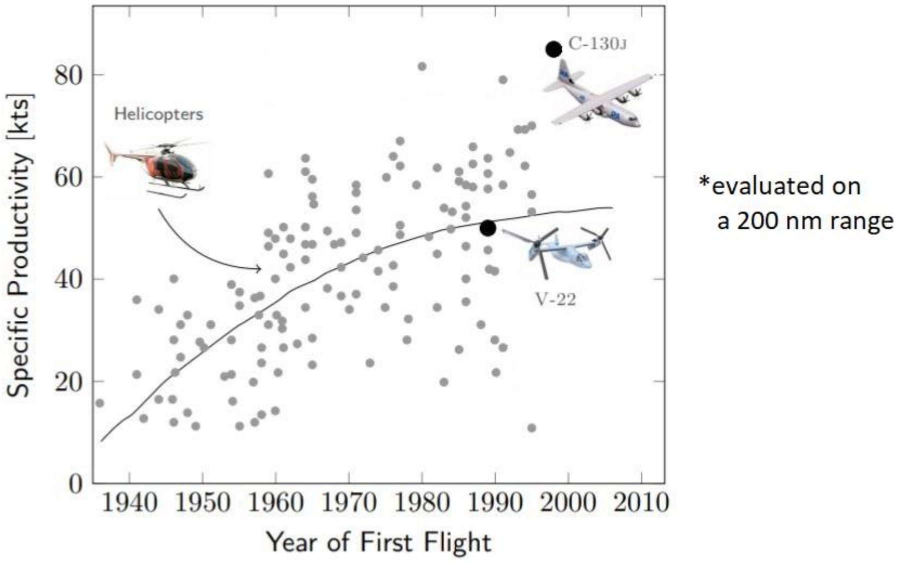

FIGURE 1. 13: Time evolution of specific productivity evaluated on a 200 nm flight range [Leishman, 2007].

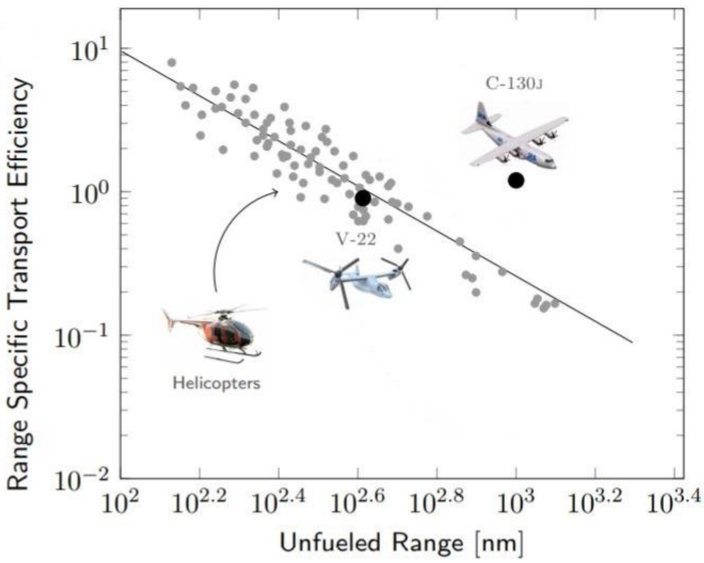

FIGURE 1. 14: Range specific transport efficiency as a function of unfueled range [Leishman, 2007].

In conclusion, it is not negligible the fact that the tiltrotor concept has become history as a cutting-edge idea with the innovative aim of meeting two different designs and making the most of them. This achievement has been mainly restricted by costs, whose form is of technological development, manufacture and operation of the aircraft, due as for example to the coexistence of both conventional aircraft flight controls and rotorcraft ones. Also, the flow field that develops around a tiltrotor is surely more complicated if compared to conventional helicopters and fixed-wing turboprop. Those factors, along with unsteady blade loads historically encountered during the conversion mode, have contributed to its relative success. Furthermore, from the quantitative analysis performed in this section, it appears clear that the tiltrotor does not represent the new incarnation of the helicopter, neither it is the future of cargo transportations. In spite of its poor performance as payload carrier, especially in *high and hot* conditions, it has its niche in both low and medium range transportation at relatively high cruise speed. This peculiarity could be exploited to move regional transportation air traffic off the main runways. From this perspective the future of the tiltrotor seems to be, at least potentially, related to that of the regional civil aviation, as witnessed by the LCTR project.

1.4 Present Dissertation

On the lookout for eco-friendlier solutions, driven by the huge exploitation of the skies and the rise of environmental issues, the aerospace engineering is reconsidering the propeller propulsion, since it is more efficient than the one provided by jets and, thanks to the possibility to be combined with electrical engines, could reduce the emissions even more. In the last fifty years, huge investments have been done on the tiltrotor concept. Nonetheless, the study of the transition phase still presents challenging problems. There is very little aeronautical literature on this unique features owing to fewer applications that have been conducted, compared to research on hover or cruise mode.

The conversion mode is extremely breakable in such a way that flight campaigns should be preceded by a complete set of both wind tunnel tests and numerical simulations. However, it is straightforward that the facilities needed to collect reliable wind tunnel data are not available to small companies and not always affordable for the whole duration of the tests, especially in the pre-prototype stage when the optimum design has not been determined yet. For these reasons, numerical simulations appear to be the most reasonable and doable way to develop a tiltrotor. At the same time, the CFD [10] method requires inordinately large computation consumption and high performance hardware, not suitable for analysing the unsteady flow field of a tiltrotor in conversion due to the complicated blade motion and the blade-tip vortex distortion. Some simplifying assumptions may be enforced: if the propeller under investigation has a diameter and an angular speed such that the resulting flow field can be assumed to be both incompressible and inviscid, then a potential method could be employed.

In this context, the objective of the present dissertation is to validate the effectiveness of the so called Vortex Particle Method applied to a V-22 digital mock-up by comparing the thrust data evaluated on the isolated proprotor model in hover flight at SL [11] to the report data concerning the considered aircraft, with which a good agreement has been found. Then a study regarding a pure tilt motion has been analysed and finally, a rough tiltrotor configuration, composed by the only propeller and wing, carrying out the time evolution of the produced thrust and evaluating the forces acting on the wing due to the flow induced by the rotating proprotor. For this purpose, in order to lead the reader towards the simulations and the results regarding the isolated proprotor and the proprotor-wing model, the theoretical framework is thoroughly descripted hereafter. Great attention has been paid to the theory lying behind the potential flows and their numerical solutions through the panel methods. Furthermore, a short presentation of PaMS, the solver employed, is following, with particular focus to the main parameters involved in modelling the rotor wake.

[10] Computational Fluid Dynamics
[11] Sea Level

CHAPTER 2

GOVERNING FLUID-DYNAMICS EQUATIONS

2.1 General outline

The aim of the current chapter and of the following two is to delineate all the theoretical bases which lay behind the solution methods that are going to be applied further on in the thesis, in order to provide the reader with a full understanding. The main three matters of interest that are going to be described are the classical potential flow theory, the numerical solution of the potential problem through a panel method and a vorton method that stems from the former, and the propeller theory.

In particular, the definition of the inviscid low-speed aerodynamics problem – which classical panel methods are based on – in mathematical terms of both fluid-dynamics differential equations and boundary conditions (*BCs*) is the focus of this chapter. Being modelling a proprotor wake by means of vortex particles the goal of the present work, the velocity field will be defined as sum of two velocity components of kinematic significance by the well-known Helmholtz decomposition. As for the inviscid evolution of the vorticity field generated by the aerodynamic surfaces and shed into the domain, the Kutta condition is introduced. Great attention is paid to the designation of the general solution to the potential problem, whereas the classical basic solutions – whose importance is related to the linearity of the Laplace's equation – are listed below. Albeit beyond the scope of this dissertation, a recall of the general Navier-Stokes equations appears to be dutiful.

2.2 Navier-Stokes Equations

Let us consider as domain of interest of our problem the external flow-field surrounding a three dimensional lifting body and assume it is continuous, that means the matter is uniformly distributed all over and there is no empty space. This is true if the fluid is dense enough, so the number of molecules contained in the volume $\mathcal{V}$ is sufficiently high. In a fixed Cartesian reference system, where the axes *X*, *Y* and *Z* are mutually orthogonal, and $\underline{i}$, $\underline{j}$ and $\underline{k}$ are unit vectors in the *X*, *Y* and *Z* direction, respectively, one can refer to any arbitrary point P that belongs to the domain by its position vector $\underline{r}$:

$$\underline{r} = \underline{r}(x, y, z, t) = x(t)\underline{i} + y(t)\underline{j} + z(t)\underline{k} \quad 2.1$$

The assumption of continuity is punctual: it means the inertial, kinematic and thermodynamic properties of the matter are continuous functions of the spatial coordinates. This is expressed in the formula:

$$\rho(x, y, z, t) = \lim_{dV \to dV_0} \frac{dm}{dV} \quad 2.2$$

where the density is defined as the derivative of the mass *m* with respect to the volume $\mathcal{V}$ which tends to the smallest volume $\mathcal{V}_0$ around *P* for which the fluid can be considered continuous.

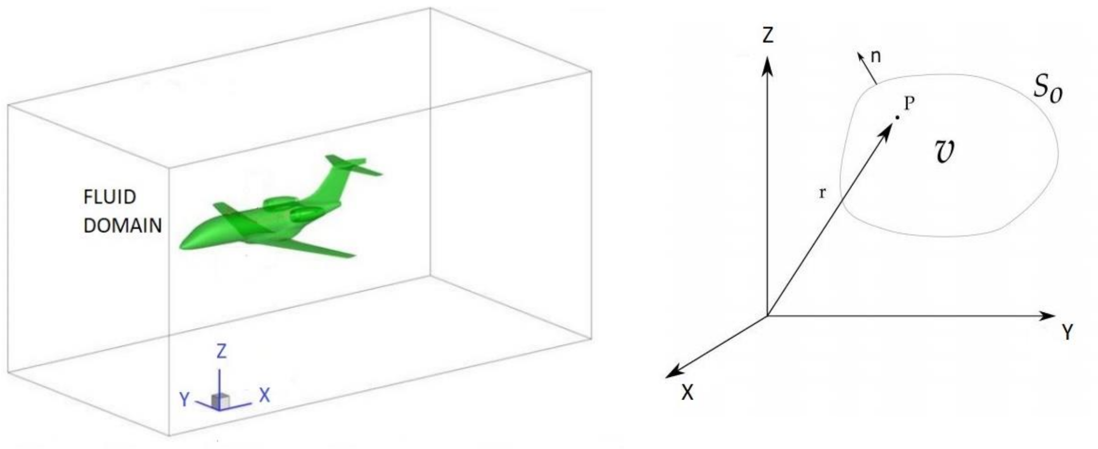

FIGURE 2. 1: Fluid domain in an *Eulerian* (conservative) approach.

The actual problem needs to be interpreted by means of physical laws expressed through equations to solve for the quantities involved. In aerodynamics, we search for a set of equations in which the kinematic and thermodynamic variables are related. If G is any of these variables, a logical balance to evaluate its variation in time can be applied, since it is kept by either an exchange across the outer surface $\mathcal{S}_0$ that bounds the volume $\mathcal{V}$ and/or a production/destruction inside the volume itself.

Variation in time	=	External interaction	+	Internal production

FIGURE 2. 2: Logical scheme of a balance equation.

The analytical tool that evaluates the first element of the right-hand side of the logical scheme is the flux of G (per unit surface per unit time), as a vector:

$$\underline{\Phi}_G = g^+ \underline{V} \qquad 2.3$$

where g^+ is the density per unit volume of the quantity G and $\underline{V}$ is the velocity vector with which G is flowing in (positive flux) or out (negative flux), hence the dimension of a flux is $[\underline{\Phi}_G] = \frac{[G][L]}{[L]^3[t]}$.

As for the second term, the quantity G in the domain may be produced or destroyed by the time due to internal causes, and we call this – positive or negative it might be – production of G per unit volume per unit time $[\dot{g}^+] = \frac{[G][L]}{[L]^3[t]}$.

The general global form of a balance equation of G is expressed by integrals extended to the entire volume of interest where the quantity is defined:

$$\frac{dG}{dt} = \frac{d}{dt}\left[\int_V g^+ dV\right] = \int_{S_0} \left(\underline{n} \cdot \underline{\Phi}_G\right) dS_0 + \int_V \dot{g}^+ dV \qquad 2.4$$

It is useful to express the same balance equation for an infinitesimal volume $d\mathcal{V}$ and obtain the local formulation by applying the Gauss theorem valid under the hypothesis of continuity of the function inside the integral:

$$\int_V \left[\frac{\partial g^+}{\partial t} + \underline{\nabla} \cdot \underline{\Phi}_G - \dot{g}^+\right] dV = 0 \qquad 2.5$$

$$\frac{\partial g^+}{\partial t} + \underline{\nabla} \cdot \underline{\Phi}_G = \dot{g}^+ \qquad 2.6$$

For the sake of precision, it has to be highlighted the fact that the approach the global (Eq. 2. 5) and local (Eq. 2. 6) formulations have been derived through is an *Eulerian* specification of the flow field, having considered the domain fixed in an inertial reference frame.

Summarizing the basic physical aspects (fluids properties, dynamics and thermodynamics) of the problem, the following laws lay the foundations of fluid-dynamics:

- Conservation of mass
- Momentum balance (Newton's law)
- Conservation of energy.

Based on these physical principles, a coupled system of non-linear Partial Differential Equations (PDEs), well-known as Navier-Stokes equations, describes a viscous, compressible, unsteady and heat-conductive single-phase fluid.

The mass balance, often referred to as the continuity equation, can be written as:

$$\frac{\partial \rho}{\partial t} + \frac{\partial (\rho V_i)}{\partial x_i} = 0 \qquad 2.7$$

with $x_i = X, Y, Z$ and where $\rho(\underline{x}, t)$ is the density field and V_i the velocity component along the x_i-direction.

The second N-S equation concerns the balance of momentum:

$$\frac{\partial (\rho V_i)}{\partial t} + \frac{\partial (\rho V_i V_j)}{\partial x_j} = -\frac{\partial p}{\partial x_i} + \frac{\partial \tau_{d_{ij}}}{\partial x_j} + \rho f_{b_i} \qquad 2.8$$

where $p(\underline{x}, t)$ is the pressure field, $\underline{f_b}(\underline{x}, t)$ gathers all the external body force (for instance due to gravity or electromagnetic actions) per unit mass exerted on the infinitesimal fluid volume and $\underline{\underline{\tau_d}}$ is the dissipative portion of the shear stress tensor $\underline{\underline{\tau}}$, defined as follows in the hypothesis of a Newtonian fluid:

$$\underline{\underline{\tau}} = -p\underline{\underline{U}} + \underline{\underline{\tau_d}} \qquad 2.9$$

$$\underline{\underline{\tau_d}} = 2\mu\left(\underline{\nabla V}\right)_0^s + \mu_v\left(\underline{\nabla} \cdot \underline{V}\right)\underline{\underline{U}} \qquad 2.10$$

Being $\underline{\underline{U}}$ the unit tensor, μ and μ_v the dynamic and the bulk viscosity coefficient, respectively.

The last equation of interest in the scope of this thesis is the energy balance, obtained by the equation 2. 8 dot multiplied by $\underline{V}$, yielding:

$$\frac{\partial}{\partial t}\left(\rho e + \frac{1}{2}\rho V^2 + p\right) + \frac{\partial}{\partial x_i}\left[\left(\rho e + \frac{1}{2}\rho V^2 + p\right)V_i\right] = -\frac{\partial p V_i}{\partial x_i} + \frac{\partial}{\partial x_i}\left(\tau_{d_{ij}} V_i + k\frac{\partial T}{\partial x_i}\right) + \rho f_{b_i} V_i \qquad 2.11$$

where $e(\underline{x}, t)$ is the internal energy of the fluid, $T(\underline{x}, t)$ the temperature and k is the Fourier's coefficient of heat conductivity.

In addition to the equations 2. 7, 2. 8 and 2. 11, fluid-dependent relations have to be added for a well-posed problem: the equation of state that links density, temperature and pressure, whose general expression is in the form:

$$f(\rho, p, T) = 0 \qquad 2.12$$

– for instance, for a perfect gas it is represented by the well-known relation $p = \rho RT$, and an equation that shows the dependency between the internal energy e and the system thermodynamic state:

$$e = e(p, T) \qquad 2.13$$

– that becomes $e = c_v T$ for an ideal gas, where c_v is the specific heat at constant volume.

2.3 Euler's Equations

The system of equations presented above is extremely complex and a solution, even by numerical methods, that concerns practical applications is tough to be found. Anyway, it is often possible to model large regions of the flow field by less complicated equations, in which smaller terms with respect to others more important are neglected. In case of inviscid (frictionless, thermally nonconductive and chemically-inert) flows, the N-S equations reduce to a set of quasilinear hyperbolic equations, known as Euler equations:

$$\frac{\partial \rho}{\partial t} + \frac{\partial (\rho V_i)}{\partial x_i} = 0 \qquad 2.14$$

$$\frac{\partial (\rho V_j)}{\partial t} + \frac{\partial (\rho V_i V_j)}{\partial x_i} + \frac{\partial p}{\partial x_j} = \rho f_{b_j} \qquad 2.15$$

$$\frac{\partial}{\partial t}\left(\rho e + \frac{1}{2}\rho V^2\right) + \frac{\partial}{\partial x_i}\left[\left(\rho e + \frac{1}{2}\rho V^2 + p\right) V_i\right] = 0 \qquad 2.16$$

In practice, the hypotheses of adiabatic and inviscid flow imply that, in equations 2. 8 and 2. 11, both the deviatoric stress tensor $\underline{\underline{\tau_d}}$ and the Fourier's thermal transport coefficient k are equal to zero. This approximation is verified the greater the Reynolds number[1] is, so that ideally equations 2. 14 to 2. 16 hold in the limit $Re \rightarrow \infty$. The Euler equations can successfully simulate incompressible and compressible flows, irrotational and rotational, even flow fields characterized by the presence of a discontinuity surface (*e.g.* a shock wave or a vortex sheet). This makes the Euler equations suitable to model a wide range of engineering flows, such as a turbofan exhaust or the interaction between the wake produced by a propeller and a wing.

2.3.1 Incompressible Constraint

A flow in which the density ρ is constant is called incompressible. As well as inviscid flows, really incompressible flow does not occur in nature, nevertheless there are many aerodynamic problems that can be modelled as being incompressible. Like the Reynolds number, the Mach number[2] is another powerful dimensionless parameter in

[1] The Reynolds number is defined as the ratio of inertial forces to viscous forces in a flow $Re = \frac{\rho_{ref} V_{ref} L_{ref}}{\mu_{ref}}$ and includes information about the fluid properties of density and viscosity, the kinematics and the geometry by means of a characteristic length that is a matter of convention. For many practical problems, if it is sufficiently high – although finite – compared to other non-dimensional parameters, the viscous effects can be concentrated on a thin layer close to the solid surface of the body well-known as boundary layer and neglected anywhere else in the field. The analysis of the boundary layer is accounted for with a set of equations named as Prandtl equations.

[2] The Mach number is defined as the ratio of a reference velocity of the flow to the speed of sound $M = \frac{V_{ref}}{a}$.

the study of gas-dynamics since theoretically, a flow is assumed to be incompressible for M < 0.3[3].

The incompressible constraint leads to a decoupling of the energy equation from the other conservation laws and hence, the continuity equation holds for the internal energy, having the pressure no thermodynamic meaning, and states that the velocity vector has zero divergence (*i.e.* it is solenoidal):

$$\underline{\nabla} \cdot \underline{V} = \frac{\partial V_i}{\partial x_i} = 0 \qquad 2.17$$

Therefore, the velocity and pressure fields are computed initially, and subsequently the energy equation may be solved for the temperature field. Moreover, this system of equations for incompressible flow presents a particular situation in which the unknown pressure does not appear under a time dependence form due to the non-evolutionary character of the continuity equation.

2.4 The Vorticity Equation

At this point, the vorticity will be briefly examined in order to introduce the role played by the vortex wake in the following paragraphs. In a velocity field, the vorticity, denoted by the vector $\underline{\omega}$, is the curl of the velocity and is twice the angular velocity:

$$\underline{\omega} = \underline{\nabla} \times \underline{V} \qquad 2.18$$

A fluid is defined irrotational if $\underline{\omega} = 0$.

Taking the curl from the Euler's momentum equation for incompressible flows leads to the vorticity equation:

$$\frac{D\omega}{Dt} = \frac{\partial\omega}{\partial t} + \underline{V} \cdot \underline{\nabla\omega} = \underline{\omega} \cdot \underline{\nabla V} \qquad 2.19$$

3 By starting from the definition of speed of sound and using as reference pressure the reference dynamic pressure, it yields: $\Delta\rho = \frac{\Delta p}{a^2} = \frac{1}{2}\rho\frac{V_{ref}^2}{a^2} \Rightarrow \frac{\Delta\rho}{\rho} = \frac{1}{2}M^2$. The limit condition of M=0, obtained when a → ∞, means that the fluid density does not vary. When M«1 the fluid is considered incompressible owing to the fact that, for instance, density variations are smaller than 5% if M=0.3.

which shows that the vorticity of a fluid particle changes because of gradients of $\underline{V}$ in the direction of $\underline{\omega}$.

2.4.1 Properties of the Vorticity Equation

- If $\underline{\omega} = 0$ everywhere initially, then $\underline{\omega}$ remains zero. Thus, flows that start off irrotational remain so.

- In a two-dimensional planar flow, $\underline{V} = (u(x,y,t), v(x,y,t), 0)$, the vector vorticity has only one non-zero component, $\underline{\omega} = \left(\frac{\partial v}{\partial x} - \frac{\partial u}{\partial y}\right)\underline{k}$, so that:

$$\underline{\omega} \cdot \underline{\nabla V} = \omega \frac{d}{dz}\underline{V}(x,y) = 0 \qquad 2.20$$

  Hence, the vorticity equation, reduced to:

$$\frac{D\omega}{Dt} = \frac{\partial \omega}{\partial t} + \underline{V} \cdot \underline{\nabla \omega} = 0 \qquad 2.21$$

  shows that the vorticity of a fluid particle is conserved. If, in addition the flow is steady, $\frac{\partial \omega}{\partial t} = 0$ then the vorticity is constant along streamlines.

- The stretching of a vortex which is represented by the term $\underline{\omega} \cdot \underline{\nabla V}$ leads to the increase of its vorticity as it is exposed to velocity gradients in the fluid field. This mechanism can be interpreted as the conservation of angular momentum of fluid particles. In an incompressible steady flow, the vorticity is proportionally amplified by the converging vortex tube cross-section and whereas the density within the tube itself has to remain constant, any shrinking of the cross-sectional area comes with a longitudinal stretching.

It is anticipated that for inviscid flows (*i.e.* in the scope of applicability of equation 2. 21, the vorticity that the presence of the body creates is convected along with the flow at a rate infinitely greater than the one associated to viscous diffusion across the flow. Actually the viscous form of the vorticity evolution equation would include a term proportional to the reciprocal of the Reynolds number. The ultimate implication of this fact is that the vorticity is confined into a thin region occupied by the wake. In other words, the flow is rotational only on the thin wake region ($\underline{\nabla} \times \underline{V} \neq 0$ at every point in the wake), whereas it is assumed to be irrotational otherwise ($\underline{\nabla} \times \underline{V} = 0$ at every point in the remaining domain).

Moreover, another important result has to be pointed out which is the relation existing between vorticity and circulation. Let *C* be a closed material curve, hence formed of fluid particle, inside the fluid domain. From Stokes' theorem:

$$\Gamma = -\oint_C \underline{V} \cdot \underline{ds} = -\iint_S (\underline{\nabla} \times \underline{V}) \cdot \underline{dS} \qquad 2.22$$

the circulation about the closed curve *C* is equal to the flux of vorticity through an arbitrary surface *S* that spans *C*. Hence, if the flow is irrotational everywhere within the contour of integration, then $\Gamma = 0$, otherwise the circulation results different from zero.

2.5 Potential Flows

The lowest level of approximation of N-S equations leads to potential flows which we are interested in. The fluid field can be efficaciously considered as ideal and irrotational and, in case of low-speed aerodynamic problems, as incompressible, thus reducing the study at linear equations with consequent mathematical simplifications.

2.5.1 The Helmholtz Decomposition

Before introducing the potential flows, it is favourable to spend some words about the so called Helmholtz decomposition. This fundamental result, obtained by Hermann Ludwig Ferdinand von Helmholtz in 1958, is based on the idea that the motion of a volume element of a continuous fluid media in $\mathbb{R}^3$ consists of:

- expansion/contraction in three orthogonal directions
- rotation about an instantaneous axis
- translation.

Particularly, due to its irrotationality, any expansion or contraction can be represented by the gradient of a scalar potential function. Similarly, the portion relative to the rotation can be described as the curl of a vector potential function owing to the hypothesis of fluid incompressibility. As a consequence, according to Helmholtz representation any sufficiently smooth, rapidly decaying vector field in three dimensions can be resolved into the sum of two parts: the first one – written as the gradient of a scalar potential function – represents both the degrees of freedom of translation and expansion/compression; the second part is related to the rotation and can be expressed as the curl of a vector potential function. Since these scalar and vector potentials can be computed from the divergence and the curl of the vector field, a vector field is uniquely defined whenever both its divergence and curl are known. This dissertation can be formalized as follows:

Theorem (Helmholtz decomposition). The motion of a fluid $\underline{V}(\underline{r})$ in an infinite space ($\underline{r} \in \mathbb{R}^3$) such that it vanishes at infinity is determinate when we know the values of $\theta(\underline{x})$ and $\underline{\omega}(\underline{x})$, where

$$\theta(\underline{r}) = \underline{\nabla} \cdot \underline{V}(\underline{r}) \qquad \text{(divergence)}, \qquad 2.23$$

$$\underline{\omega}(\underline{r}) = \underline{\nabla} \times \underline{V}(\underline{r}) \qquad \text{(curl)} \qquad 2.24$$

On the other hand, if the motion of the fluid is limited to a simply connected region $\Omega \subset \mathbb{R}^3$ with boundary $\partial\Omega$, it is determinate if $\theta(\underline{r})$ and $\underline{\omega}(\underline{r})$ and the value of the flow normal to the boundary, $V_n(\underline{r}) = \underline{V}(\underline{r}) \cdot \underline{n}$ for $\underline{x} \in \partial\Omega$, are known.

An inverse formulation is admitted, consisting in the decomposition of a vector field (satisfying appropriate smoothness and decay conditions) into its irrotational $\underline{\nabla}\phi$ (curl-free, *i.e.* $\underline{\nabla} \times \underline{\nabla}\phi = \underline{0}$) and solenoidal $\underline{\nabla} \times \underline{\psi}$ (divergence-free, *i.e.* $\underline{\nabla} \cdot \left(\underline{\nabla} \times \underline{\psi}\right) = 0$) components.

Theorem (Helmholtz decomposition – Inverse). Every smooth field $\underline{V} \in \mathbb{R}^3$ on a bounded domain, defined in a simply connected region can be expressed as the sum of the gradient of a scalar potential and the curl of a vector potential:

$$\underline{V} = \underline{\nabla}\phi + \underline{\nabla} \times \underline{\psi} \qquad 2.\ 25$$

where the scalar potential ϕ and the vector one $\underline{\psi}$ are evaluated from θ and $\underline{\omega}$ respectively, as:

$$\phi(\underline{r}) = \frac{1}{4\pi}\int_V \frac{\theta(r)}{|\underline{r'}|}dV \qquad 2.\ 26$$

$$\underline{\psi}(\underline{r}) = \frac{1}{4\pi}\int_V \frac{\underline{\omega}(r)}{|\underline{r'}|}dV \qquad 2.\ 27$$

Where $\frac{1}{4\pi|\underline{r'}|}$ is the Green function.

Note that the functions into the volume integral must be evaluated at the position $\underline{r}$, referring from the origin. Then $\underline{r}$ coincides with the evaluation point of ϕ (or $\underline{\psi}$), while $\underline{r'}$ is the relative position between the evaluation point and any point swept by the volume integral (see Figure 2. 3).

Moreover, it should be noted that the vanishing condition at infinity is required in order to have converging integrals in equations 2. 26 and 2. 27 and that the potentials ϕ and $\underline{\psi}$ are unique up to a constant, meaning that the decomposition is unique.

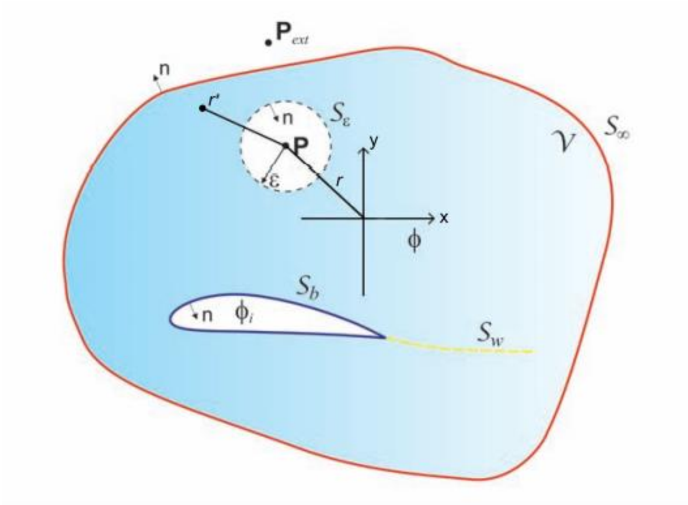

FIGURE 2. 3: The fluid domain considered in the derivation of the Green's theorem.

2.6 Laplace and Poisson's equations

It is known from the vector calculus that the curl of the gradient of any scalar potential function ϕ is always the zero vector and, similarly, that it is equal to zero the divergence of the curl of any vector potential function $\underline{\psi}$:

$$\underline{\nabla} \times (\underline{\nabla}\phi) = 0 \qquad 2.28$$

$$\underline{\nabla} \cdot \left(\underline{\nabla} \times \underline{\psi}\right) = 0 \qquad 2.29$$

Then for the vector function $\underline{V}$, the following identities result to be valid:

$$\underline{\nabla} \cdot \underline{V} = \underline{\nabla} \cdot \left(\underline{\nabla}\phi + \underline{\nabla} \times \underline{\psi}\right) = \nabla^2\phi \qquad 2.30$$

$$\underline{\nabla} \times \underline{V} = \underline{\nabla} \times \left(\underline{\nabla}\phi + \underline{\nabla} \times \underline{\psi}\right) = \underline{\nabla}\left(\underline{\nabla} \cdot \underline{\psi}\right) - \nabla^2\underline{\psi} \qquad 2.31$$

Now, if both the vector potential $\underline{\psi}$ and the vector function $\underline{V}$ are solenoidal, equations 2. 30 and 2. 31 become:

$$\nabla^2\phi = 0 \qquad 2.32$$

$$-\nabla^2\underline{\psi} = \underline{\nabla} \times \underline{V} \qquad 2.33$$

which, in order, are known as the Laplace and Poisson's equations, and whose respective solutions are expressed by equations 2. 26 and 2. 27.

Please note that the irrotationality is a necessary and sufficient condition for the existence of the velocity potential ϕ. This scalar potential consents the substitution of a three-component vector by a single scalar as the principle unknown in theoretical investigation. In this case the definition of $\underline{\psi}$ is statement of the mass conservation. In fact, $\underline{V}_{\psi} = \underline{\nabla} \times \underline{\psi}$ automatically satisfies the continuity equation for ideal, irrotational and incompressible flows (see equation 2. 29). From a physical point of view, this result suggests that the iso-ψ lines are coincident with the streamlines and that the difference between two streamlines represents the volumetric flow rate between the two. The velocity potential is analogous to the stream function in the sense that derivatives of ϕ yield the velocity but there are distinct differences between ϕ and $\underline{\psi}$. First, the velocity is obtained by differentiating ϕ in the velocity direction, whereas $\underline{\psi}$ in the direction normal to the velocity direction. Second, the velocity potential is defined only for irrotational flow, whereas the stream function can be defined either for rotational and irrotational flows.

Moreover, remembering Eq. 2. 18, the Poisson's equation shows the relation that exists between the vector potential and the vorticity field:

$$\nabla^2 \underline{\psi} = -\underline{\omega} \qquad 2.34$$

Therefore, the problem can be worked out by solving one Laplace's equation for the irrotational component and one Poisson's equation for the solenoidal component.

It should be remarked that Eq. 2. 32 is a linear elliptic differential equation which results in a boundary-value problem, whose non-trivial solutions are harmonic functions. This implies the fact that the superposition of the effects can be employed and the solution of a complicated flow pattern for an incompressible flow can be obtained as the sum of a number of elementary incompressible flow solutions from the scalar potential ϕ. Panel methods are based on this consideration. However a further clarification about the wake and the linear behaviour of the Laplace's equation has to be done. The wake surface in panel methods is part of the domain boundary. Then if its shape is known *a priori*, there is no problem in determining the velocity field by linearity. The most common issues concern bodies of various geometries around which it is desired to know the velocity field and the wake. The Helmholtz conservation theorems about circulation establish a link between velocity field and the wake, thus to calculate the velocity it is needed to know the vorticity distribution which is in turn linked to the unknown velocity. This is obviously a non-linearity that can be overcome though. Prandtl simply nailed down the wake of wings to a plane, made it rigid, and recent algorithms take this great intuition as starting guess within iterative procedures, thus the wake data are known and the velocity field can be calculated, although by attempts.

Finally, in order to help the reader to fix in mind the hypothesis chain which leads to the Laplace's equation starting from the Navier-Stokes system, a summarizing scheme is reported in Figure 2. 4.

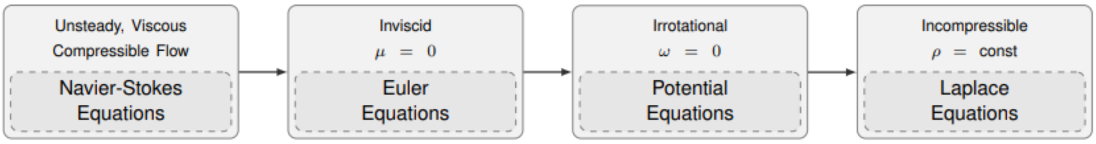

FIGURE 2. 4: Scheme summarising the main fluid model.

2.7 Unsteady Bernoulli Equation

The pressure field (required for determining the aerodynamic forces acting on the body object of our study) can be computed by Bernoulli equation, once the flow field has been determinate. The Bernoulli equation, the most widely used equation in fluid mechanics, is derived starting from the Eulerian momentum equation (2. 15 – so assuming frictionless flow with no work or heat transfer – which, under the hypothesis of incompressible flow, becomes:

$$\frac{\partial \underline{V}}{\partial t} + \underline{V} \cdot \underline{\nabla V} = \underline{f_b} - \frac{\nabla p}{\rho} \qquad 2.35$$

Moreover, standing the vectorial identity such that: $\underline{\nabla}\left(\frac{V^2}{2}\right) = \underline{V} \cdot \underline{\nabla V} + \underline{V} \times \left(\underline{\nabla} \times \underline{V}\right) = \underline{V} \cdot \underline{\nabla V} + \underline{V} \times \underline{\omega}$, it follows:

$$\frac{\partial \underline{V}}{\partial t} + \underline{\nabla}\left(\frac{V^2}{2}\right) - \underline{V} \times \underline{\omega} = \underline{f_b} - \frac{\nabla p}{\rho} \qquad 2.36$$

Thus, for an irrotational flow (*i.e.* $\underline{\omega} = 0$, $\underline{V} = \underline{\nabla}\phi$), that is the entire domain of interest excluding the trailing vortex wake region:

$$\frac{\partial \underline{V}}{\partial t} = \frac{\partial}{\partial t}\underline{\nabla}\phi = \underline{\nabla}\left(\frac{\partial \phi}{\partial t}\right) = \underline{f_b} - \underline{\nabla}\left(\frac{V^2}{2}\right) - \frac{\nabla p}{\rho} \qquad 2.37$$

If, furthermore, the body force $\underline{f_b}$ is conservative (*i.e.* if a scalar potential E of the field $\underline{f_b}$ does exist such that $\underline{f_b} = -\underline{\nabla}E$, as in the case of the gravitational force where $E = -gz$) then equation 2. 37 yields:

$$\underline{\nabla}\left(\frac{\partial \phi}{\partial t} + \frac{V^2}{2} + \frac{p}{\rho} + E\right) = \underline{0} \qquad 2.38$$

$$\frac{\partial \phi}{\partial t} + \frac{V^2}{2} + \frac{p}{\rho} + E = C(t) \qquad 2.39$$

this latter well-known as the unsteady Bernoulli equation for inviscid, irrotational and incompressible flows, where *C(t)* is a time dependent integration variable. A more useful formulation is found by evaluating Eq. 2. 39 in two different points of the flow field at the same time instant. In particular, a convenient choice is a point located at the infinity and characterized by the following reference conditions: $V_\infty = 0$, $E_\infty = 0$ and thus $\phi_\infty = const$. Under these assumptions, the pressure field at any point and at any time, can be evaluated by means of this relation:

$$\frac{p-p_\infty}{\rho} = \frac{\partial \phi}{\partial t} + \frac{V^2}{2} + E \qquad 2.\,40$$

Also for steady, incompressible and rotational fluids Eq. 2. 39 holds along each streamline (the time derivative is obviously set to zero), if the integration parameter *C(t)* is allowed to vary from a streamline to another one. In fact, the cross product $\underline{V} \times \underline{\omega}$ is locally normal to the streamline $\underline{d\ell}$, so that their dot product vanishes along the streamline itself.

2.8 Boundary Conditions

As stated in the previous paragraph, due to the simplifying assumptions, the ultimate problem under analysis consists in the Laplace (2. 32) and Poisson's (2. 34) equations that results to be unclosed, meaning that – as it is – its solution is neither unique nor physically consistent with the particular geometric and free-stream conditions. Being a differential model, to be in close form it requires additional conditions to be specified on the borders of the domain of interest, namely the boundary conditions. Those provide information about the specific geometry of the body, the flow conditions at an ideally infinite distance away from the body and, for lifting bodies, the smoothness of the solution at the wing trailing edge. As for unsteady flow problems – due to time variations of the asymptotic velocity vector, or body deformations, or changes in time of other flexible surfaces like the wake – time function BCs have to be taken into account for the solution uniqueness at each time. Therefore, the boundary conditions need to be specified and updated in time in order to solve the Laplace's equation – that instead has no time dependence – in the variable ϕ and then the velocity field associated to it.

Free stream. Since the domain boundary is located far away from the body, it could be assumed that the flow properties are not influenced by the body itself and the disturbances inside the flow field decays to zero. Hence, at infinity,

$$\lim_{|\underline{x}|\to\infty} \phi = \phi_\infty \qquad 2.41$$

where ϕ_∞ represents the undisturbed velocity field.

Wall. The problem that has been formulating is inviscid, so the no-slip condition with regard to the tangential component generally imposed for the viscous case and which reflects the absence of relative motion between the wall and the nearby fluid layers due to the friction, cannot be employed. Yet in the case of interest, the only velocity component V_n locally normal to the body surface can be prescribed. One could deal with two distinct situations:

- non-porous wall: the flow is tangent to the solid surface point by point, which implies a zero component of velocity normal to the surface
- transpiration velocity.

In formulae, defining $\underline{n}(\underline{x}, t)$ the unit vector locally normal to the surface in the point $P(\underline{x})$ at the time t and V_{tr} the transpiration velocity, the wall BC can be written as:

$$\underline{n} \cdot \underline{\nabla}\, \phi = V_{tr} \qquad 2.42$$

where $V_{tr} = 0$ for non-porous surfaces.

Equation 2. 42 represents a direct formulation of the wall BC, well-known as a Neumann boundary condition, although the same concept can be expressed by assigning a value to the potential ϕ on the boundary. In this latter case, the impermeability condition is imposed indirectly through a Dirichlet BC. Obviously a combination of these two methods can be employed, obtaining a mixed BCs problem.

Kutta condition. For potential flows, having added the free stream and body surface boundary conditions to the problem governed by the Laplace's equation does not guarantee the solution uniqueness. In fact, this latter, for a multiple connected region, *i.e*. the case of a 3-dimensional wing shedding a wake, is ensured when the circulation Γ is fixed by means of a physical condition. Moreover we assume that the physical condition is then related to the shape of the solid bodies, as their geometries influence the way the flow approaches, flows and then leaves their borders.

Kutta condition applies to aerodynamic bodies, by definition those with a sharp trailing edge, because the fluid flowing on their surface would eventually encounter an infinite curvature, hence it would require an infinite acceleration. The effect of viscosity would decelerate the fluid in the proximities of the solid surfaces and neutralise the increasing acceleration trend at the trailing edge. When the flow field is approximated as potential, thus inviscid, this circumstance must be specifically treated.

The fluid velocity characteristics at the airfoil TE are fixed in such a way that it does not follow the curvature but instead leaves the cusp smoothly: there the velocity field is continuous and its module finite. Since the TE angle is finite, in order to satisfy the Kutta condition, the flow is imposed to be parallel to its bisector line, meaning that the normal component of the velocity, from both sides of the airfoil, has to vanish. This is possible only if the TE is a stagnation point. Hence no pressure jump across it:

$$\Delta p_{TE} = 0 \tag{2.43}$$

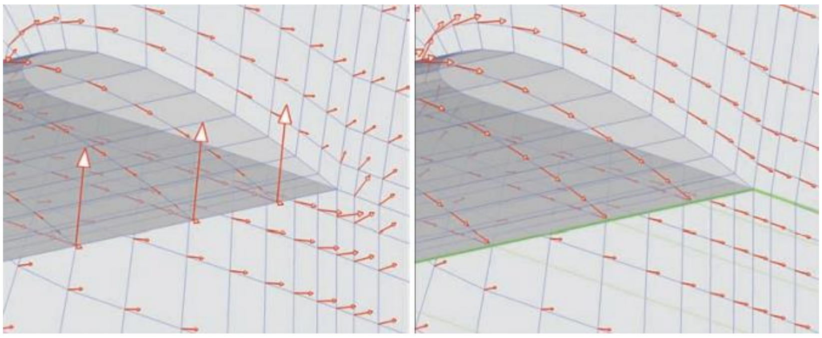

FIGURE 2. 5: Flow field at the wing trailing edge without (on the left) and with (on the right) the superimposition of the Kutta condition on the same aerodynamic body at the same angle of attack.

Additionally, this can be obtained by requiring for the circulation around the trailing edge to be null, and thus for the vorticity component parallel to the TE to be zero:

$$\gamma_{TE} = 0 \tag{2.44}$$

Either way, in order to prescribe the streamwise vorticity release at the trailing edge – equal to the spanwise circulation, a linearised formulation of the pressure continuity at the TE is used that yields a discontinuity in the velocity potential there:

$$\Gamma = \phi_U - \phi_L = \Delta\phi_w \qquad 2.45$$

with the subscripts U and L for points on the upper and lower surface at the wing TE, whereas w stands for wake.

The superimposition of the Kutta condition therefore entails the introduction of an appropriate vorticity into the domain that is identified with a swirling line coincident with the trailing edge of the wing. According to Kelvin and Helmholtz theorem, this vortex line cannot start nor end inside the fluid, but it has either to be convected indefinitely downstream or to loop back on itself, and keeps its magnitude constant in time and in each section. Also, assumed to be thin, it is necessary that the wake does not produce any lift. In general, the aerodynamic force $\underline{\Delta F}$ generated by a vortex sheet whose specific intensity is denoted by γ is given by the Kutta-Joukowski theorem:

$$\underline{\Delta F} = \rho\underline{V} \times \underline{\gamma} \qquad 2.46$$

Hence, imposing $\underline{\Delta F} = 0$ and assuming $\gamma \neq 0$, the wake cannot but be carried out by the flow:

$$\underline{V} \times \underline{\gamma_w} = \underline{0} \Longrightarrow \underline{\gamma_w} \parallel \underline{V} \qquad 2.47$$

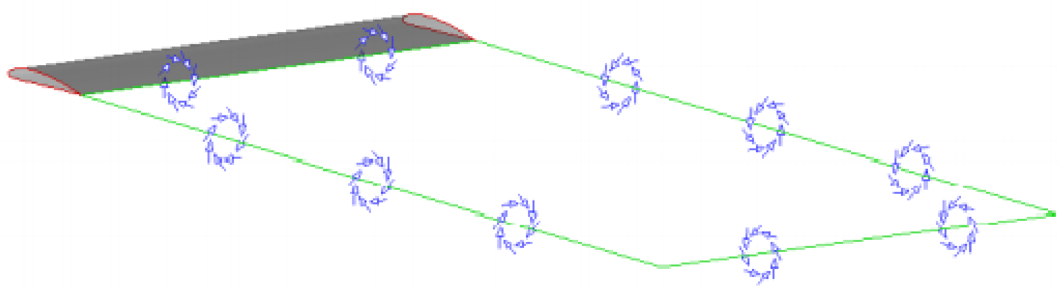

FIGURE 2. 6: Vortex line at a wing TE obtained by imposing the Kutta condition.

For unsteady flows, a time dependent Kutta condition has to be enforced. Holding the Helmholtz vortex theorem (stating that the rate of change in time of the circulation around a closed curve consisting of the same fluid elements is zero), any increase in bound vorticity on the wing must be balanced by an equivalent increase in vorticity shed into the wake.

Other conditions. Other kinds of BCs may be required to be imposed, according to the physical problem that one is analysing, as for example a free-surface condition is needed in case more than one fluid with different densities are present and the gravitational field is taken into account. This is typical in naval applications where boats navigate across the water surface. In general, in steady situations, a kinematic condition (tangency of velocities) and a dynamic one (balance of pressures) have to be enforced at the fluid interphase; in addition they are coupled due to the surface being free by definition. One is not going into details, not being functional for the case of interest.

2.9 General Solution and Singularity Elements

In aerospace engineering applications, the mathematical model that has been outlined might define an outer flow problem such as the study of the aerodynamic forces acting on a wing like the fluid volume depicted in Figure 2. 3. It should be pointed out the outward definition of the local normal $\underline{n}$ to the boundaries S_b and S_∞ of the volume $\mathcal{V}$.

As previously stated, the sought general solution to the potential flow problem is based on Green's integral theorem. More specifically, let us name Φ_1 and Φ_2 two scalar functions of position defined in $\mathcal{V}$ and here continuously differentiable twice; the Green's second identity, derived from Gauss' integral theorem, can be written as:

$$\iint_S (\Phi_1 \underline{\nabla}\,\Phi_2 - \Phi_2 \underline{\nabla}\Phi_1) \cdot \underline{n}\, dS = \iiint_V (\Phi_1\, \nabla^2 \Phi_2 - \Phi_2 \nabla^2 \Phi_1)\, dV \qquad 2.48$$

where $S = S_\infty \cup S_b \cup S_w$, namely the surface integral is taken over all the boundaries, including a wake surface S_w which a discontinuity in either velocity or velocity potential may occur across.

In order to derive Green's fundamental formula of potential theory, one sets the function Φ_1 equal to the reciprocal of the distance d between a given field point P, with position vector $\underline{r}$ and an arbitrary point of the integration domain identified by $\underline{r}'$ from P, such that $d = |\underline{r}'|$ (please refer to Figure 2. 3) and the function $\Phi_2 = \phi$ equal to the potential of the flow of interest, both harmonic (*i.e.* they satisfy the Laplace's equation).

Three different cases may happen. If the point P does not belong to the domain $\mathcal{V}$, the equation 2. 48 yields:

$$\iint_S \left(\frac{1}{d}\underline{\nabla}\phi - \phi\underline{\nabla}\frac{1}{d}\right)\cdot \underline{n}\, dS = 0, \qquad P \notin \mathcal{V} \tag{2. 49}$$

Nevertheless, of particular interest is when the field point P is situated in the integration domain. If $|\underline{r}'| = 0$, P is a singular point. One excludes this point from the integration domain by surrounding it with a small sphere with centre at P and radius ε. Be S_ε the surface of this sphere. The use of Green's integral theorem on the domain that is contained between the spherical surface S_ε and the surface S, in the limit $\varepsilon \rightarrow 0$, yields:

$$\phi(P) = \frac{1}{4\pi}\iint_S \left(\frac{1}{d}\underline{\nabla}\phi - \phi\underline{\nabla}\frac{1}{d}\right)\cdot \underline{n}\, dS, \qquad P \in \mathcal{V} \tag{2. 50}$$

known as Green's third identity, this formula gives the value of $\phi(P)$ at any point in the flow, within the region $\mathcal{V}$, in terms of the values of ϕ and $\underline{\nabla}\phi \cdot \underline{n} = \frac{\partial\phi}{\partial n}$ on the boundaries S.

In general, an internal potential ϕ_i can be defined, meaning that the flow is located inside the boundaries S_b, so that the point $P \in \mathcal{V}$ is exterior to S_b. Furthermore, assuming the wake surface S_w to be thin, so that the quantity $\frac{\partial\phi}{\partial n}$ is continuous across it, and thus given by the potential difference between the upper and lower wake surface itself, and defining the far-field potential ϕ_∞ as:

$$\phi_\infty(P) = \frac{1}{4\pi}\iint_{S_\infty} \left(\frac{1}{d}\underline{\nabla}\phi - \phi\underline{\nabla}\frac{1}{d}\right)\cdot \underline{n}\, dS \tag{2. 51}$$

the combination of the inner and the outer potential leads to:

$$\phi(P) = \phi_\infty(P) + \frac{1}{4\pi}\iint_{S_b}\left[\frac{1}{d}\underline{\nabla}(\phi - \phi_i) - (\phi - \phi_i)\underline{\nabla}\frac{1}{d}\right]\cdot \underline{n}\, dS$$
$$-\frac{1}{4\pi}\iint_{S_w}(\phi_U - \phi_L)\underline{n}\cdot\underline{\nabla}\frac{1}{d}dS$$

2. 52

This formula provides the value of ϕ(P) in terms of ϕ and $\partial\phi/\partial$n on the boundaries. The flow problem is reduced to determining these values all over the domain boundaries, once the internal potential has been fixed.

At the end, if the point *P* lies on the boundary S_b, the potential $\phi(P)$ becomes singular, therefore the surface integration should occur around the hemisphere with radius ε. Equation 2. 52 becomes:

$$\phi(P \in S_b) = \phi_\infty(P) + \frac{1}{4\pi}\iint_{S_b}\frac{1}{d}\underline{n}\cdot\underline{\nabla}(\phi - \phi_i)\, dS - \frac{1}{4\pi}\iint_{S_b - P}(\phi - \phi_i)\underline{n}\cdot\underline{\nabla}\frac{1}{d}dS$$
$$\pm\frac{1}{2}(\phi - \phi_i)_P - \frac{1}{4\pi}\iint_{S_w}(\phi_U - \phi_L)\underline{n}\cdot\underline{\nabla}\frac{1}{d}dS$$

2. 53

where the factor $^1/_2$ is due to the use of the hemisphere instead of the sphere, and the sign depends on which face of S_b the point *P* belongs to.

Of course the solution 2. 53 must satisfy the Neumann condition (2. 42) on the surface S_b, whereas no condition in terms of potential results a necessity on the surface S_w, because it represents itself the imposition of the wing trailing edge Kutta condition. The jump in potential in the wake surface integral is encountered in (2. 45) where it must assure that the velocity does not rotate round the trailing edge. This way the $\Delta\phi$ on the wake does not introduce additional unknowns to the problem, because it is associated to the unknown potentials at the TE, and thus its contribution has to be considered as a known term. However, a constraint does exist for the wake and is related to its shape. As previously commented, due to its flexible nature, the wake cannot support load, therefore a condition of tangency to the local flow direction is established (Eq. 2. 47). In order to enforce it, it is necessary to know the flow field $\underline{V}$, which is the goal of the analysis though. This non-linearity can be tackled by approaching the wake with a fixed form, independent from the flow field (as already stated with a Prandtl wake model), or with iterative techniques[4].

Going back to equation 2. 53, it is a good practice to choose as singularity combination among the infinite that solve the problem, the one whose potential jump across the boundary is minimum and hence the one that minimise the perturbation introduced by the singularity itself with respect to the undisturbed flow field. This is achieved by setting a Dirichlet boundary condition on the internal potential such that $\phi_i = \phi_\infty$

Now let us consider a segment of the boundaries S_b, as shown in Figure 2. 7, and relate the differences between internal and external potentials and between their normal derivatives respectively to the *doublet* and the *source* singular solutions of Eq. 2. 32, since they are both singular as d approaches zero and, at the same time, the free-stream BC 2. 41) is automatically fulfilled, given that these quantities vanish in the limit $d \to \infty$. Equation 2. 53 can be rewritten with the singularities established at the outset as:

$$\iint_{S_b} \frac{\sigma}{d} dS - \iint_{S_b - P} \mu \, \underline{n} \cdot \underline{\nabla} \frac{1}{d} dS + 2\pi\mu_P - \iint_{S_w} \mu_w \underline{n} \cdot \underline{\nabla} \frac{1}{d} dS = 0 \qquad 2.\,54$$

where:

$$4\pi\mu = \phi - \phi_\infty \qquad \textit{doublet} \qquad 2.\,55$$

$$4\pi\sigma = -\underline{n} \cdot \left(\underline{\nabla}\phi - \underline{\nabla}\phi_\infty\right) = -V_n + V_{n_\infty} \qquad \textit{source} \qquad 2.\,56$$

$$\mu^w = \frac{\phi_U - \phi_L}{4\pi} \qquad 2.\,57$$

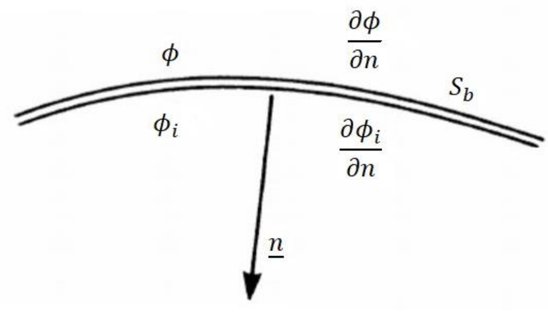

FIGURE 2. 7: Velocity potential and normal derivative near a solid boundary.

[4] The fluid field is solved on the basis of a first attempt wake shape, hereafter corrected once the velocity field has been determined. These two steps may be repeated until the difference between two successive solutions is less than a desired value.

Note that sources and doublets have a physical sense: thickness effects can be simulated by means of sources, non-symmetrical conditions are given by means of doublets. Equation 2. 56 shows that the Neumann condition is satisfied straightaway by the only sources which, as a consequence, are known.

So far thick configurations having a distinct internal volume enclosed by a surface have been concerned. When there is an indistinct internal volume, parts of the configuration are extremely thin and can be represented by open surface. In this case, Equation 2. 52 becomes:

$$\phi(P) = \phi_\infty(P) + \frac{1}{4\pi}\iint_{S_b}\left[\frac{1}{d}\underline{\nabla}(\phi_U - \phi_L) - (\phi_U - \phi_L)\underline{\nabla}\frac{1}{d}\right]\cdot \underline{n}\, dS - \frac{1}{4\pi}\iint_{S_w} \mu_w \underline{n}\cdot\underline{\nabla}\frac{1}{d}\, dS \tag{2.58}$$

In case of continuity of normal velocity through the sheet, naming $\mu = \frac{\phi_U - \phi_L}{4\pi}$ the jump in total potential across:

$$\phi(P) = \phi_\infty(P) - \iint_{S_b} \mu\, \underline{n}\cdot\underline{\nabla}\frac{1}{d}\, dS - \iint_{S_w} \mu^w \underline{n}\cdot\underline{\nabla}\frac{1}{d}\, dS \tag{2.59}$$

Applying the external Neumann BC, then:

$$\underline{n}\cdot\underline{\nabla}\phi(P) = \underline{n}\cdot\underline{\nabla}\phi_\infty(P) - \iint_{S_b} \mu\, \underline{n}\cdot\underline{\nabla}\left(\underline{n}\cdot\underline{\nabla}\frac{1}{d}\right) dS - \iint_{S_w} \mu^w \underline{n}\cdot\underline{\nabla}\left(\underline{n}\cdot\underline{\nabla}\frac{1}{d}\right) dS \tag{2.60}$$

At the end, 2. 54 and 2. 60 are the basic equations for the solution of a flow problem. Thanks to Laplace's equation linearity, in order to determine the velocity potential ϕ at any point in the region $\mathcal{V}$, the flow-field may be modelled by means of singularity superposition distributed all over the boundaries whose strengths have to be evaluated by enforcing the BCs. Thus the differential equation does not have to be solved individually for flow fields having different geometry at their boundaries. Instead, the elementary solutions will be distributed in a manner that will satisfy each individual set of geometrical boundary conditions. There is no unique combination of sources and doublets distribution: the choice is driven by the physics of the problem.

At present, it is favourable to analyse the main *basic solutions* to the Laplace's equation.

Free stream. A polynomial first order function is the simplest basic solution to Laplace's equation, often employed for the free stream potential, as it models the constant velocities of undisturbed flow:

$$\phi_\infty(x,y,z) = u_\infty x + v_\infty y + w_\infty z = V_{\infty_i} x_i \qquad 2.61$$

so that the velocity vector field is expressed by:

$$\underline{V_\infty} = \left(\frac{\partial \phi_\infty}{\partial x}, \frac{\partial \phi_\infty}{\partial y}, \frac{\partial \phi_\infty}{\partial z}\right) = (u_\infty, v_\infty, w_\infty) \qquad 2.62$$

And depicted in the following figure with both iso-ψ (*i.e.* the streamlines) and equipotential lines (*i.e.* iso-ϕ) are highlighted.

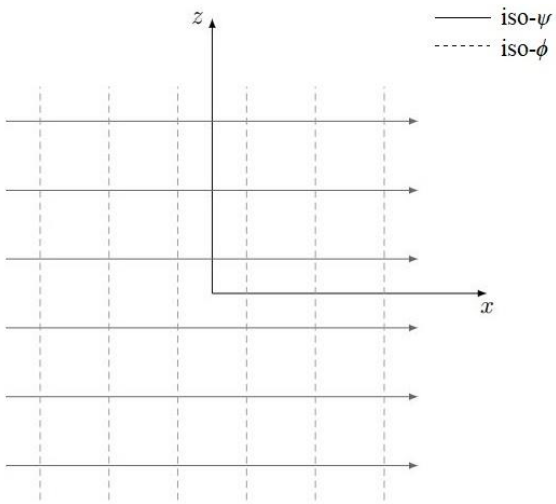

FIGURE 2. 8: Flow-field induced by a free stream.

Point source/sink. This singular element, already introduced in equation 2. 54 and 2. 56, represents a concentric motion directed away (towards) the point where it is located. In a local spherical reference frame (r, θ, φ), it is characterized by the potential:

$$\phi(P) = -\frac{\sigma}{4\pi r} \qquad 2.63$$

where r is the distance of a point P from the origin. So it can be observed that σ expresses the volumetric flow rate through a spherical surface of radius r. The velocity induced by the point source/sink in the surrounding space has got only the radial component, that decays as $1/_{r^2}$ and is singular in $r = 0$:

$$\underline{V} = \left(V_r, V_\theta, V_\varphi\right) = \left(\frac{\partial\phi}{\partial r}, 0{,}0\right) = \left(\frac{\sigma}{4\pi r^2}, 0{,}0\right) \qquad 2.\,64$$

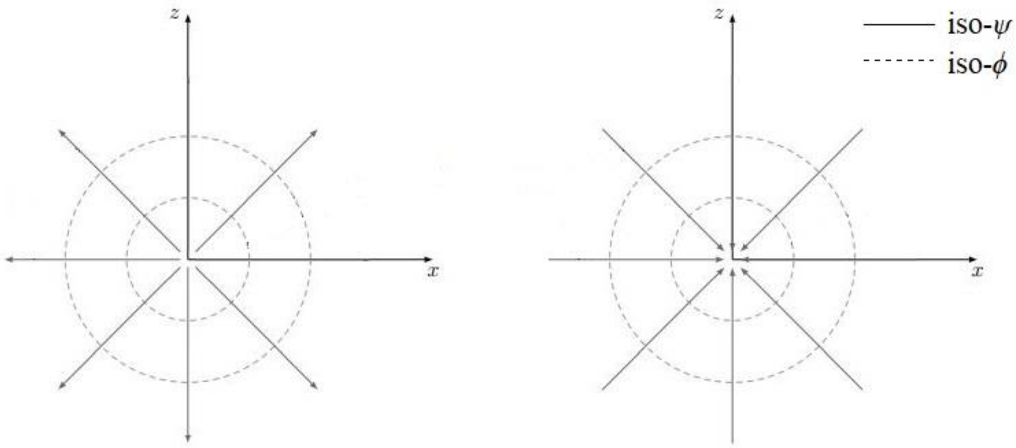

FIGURE 2. 9: Flow-field induced by a point source (on the left) / point sink (on the right).

Point doublet. Aside the source, Eq. 2. 54 contains terms related to this other singularity element, whose potential is expressed by:

$$\phi(P) = \frac{\mu}{4\pi}\underline{n} \cdot \underline{\nabla}\frac{1}{r} \qquad 2.\,65$$

It can be demonstrated by referring to Figure 2. 9 that a doublet is generated by a source and a sink of same intensity σ aligned along the x-axis and separated by a distance ℓ, for $\ell \rightarrow 0$ and $\sigma \rightarrow \infty$, so that the product $\ell\sigma$ is finite and $\ell\sigma \rightarrow \mu$. The relation that exists between the doublet and the source in formulae is:

$$\phi_\mu = -\frac{\partial\phi_\sigma}{\partial n} \qquad 2.\,66$$

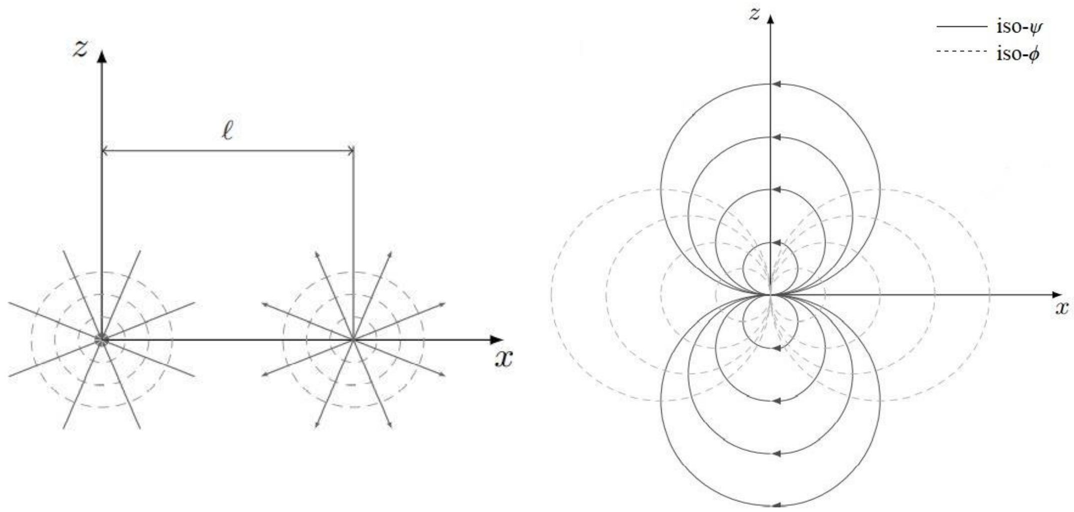

FIGURE 2. 10: doublet genesis from a sink and a source aligned (on the left) and flow-field induced by a point doublet (on the right).

Moreover, it can be proven that the velocity field has got a directional behaviour: in particular, the doublet axis ($\underline{e_\mu}$ its unit vector) is defined as the direction where both the originating sink and source lie on and for this reason, the quantity μ can be interpreted as a vector: $\underline{\mu} = \mu\underline{e_\mu}$.

Point vortex. Although the general solution to the Laplace's equation has been given as superposition of sources and doublets, other basic solutions do exist. Indeed, it is possible to show that doublet elements are equivalent to vortex elements of one order of polynomial approximation lower. A vortex is defined as the dual element of the source. Therefore it is a singularity characterised by a purely circular motion and thus by the only presence of the tangential velocity component:

$$\phi(P) = -\frac{\Gamma}{2\pi}\theta \qquad 2.\,67$$

$$V_\theta = -\frac{\Gamma}{2\pi r} \qquad 2.\,68$$

where Γ is the circulation evaluated along a generic path which surrounds the vortex itself located at the origin. Note that the velocity potential of a vortex is multivalued, depending on the round of revolutions performed around the vortex point.

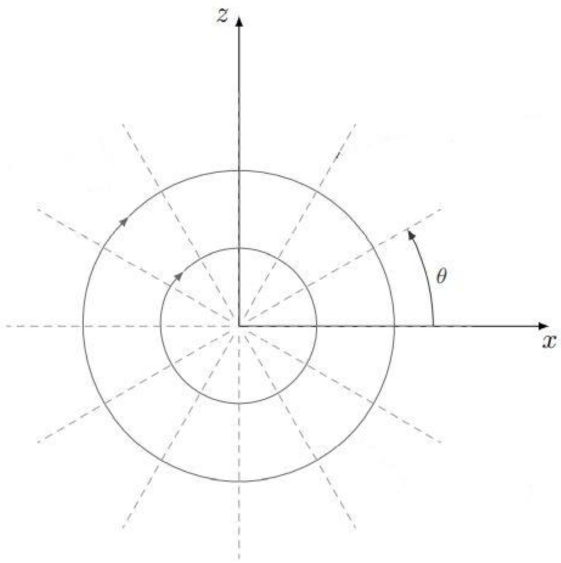

FIGURE 2. 11: Flow-field induced by a point vortex.

In the general case, the potential may be integrated over a curve, surface or volume, in order to generate the corresponding singularity elements. In these cases, it must not be addressed to strength (like in the case of point elements), but strength density per unit of length, area or volume, respectively. Let us take a quick look to a 3-D generalisation of the basic solutions. The simplest 3-D elements have a quadrilateral geometry with a constant-strength singularity.

The quadrilateral source shown in Figure 2. 12 is a surface element bounded by four straight lines, with a constant strength σ; its potential induction on a point *P(x, y, z)* whose coordinates are expressed in a local reference frame with origin in the quadrilateral centre and the z-axis normal to it, is developed using the point source elements distributed on the surface S, obtaining:

$$\phi(x, y, z) = -\frac{\sigma}{4\pi}\iint_S \frac{dS}{r} \qquad 2.\ 69$$

where $r = \sqrt{(x - x_0)^2 + (y - y_0)^2 + (z)^2}$.

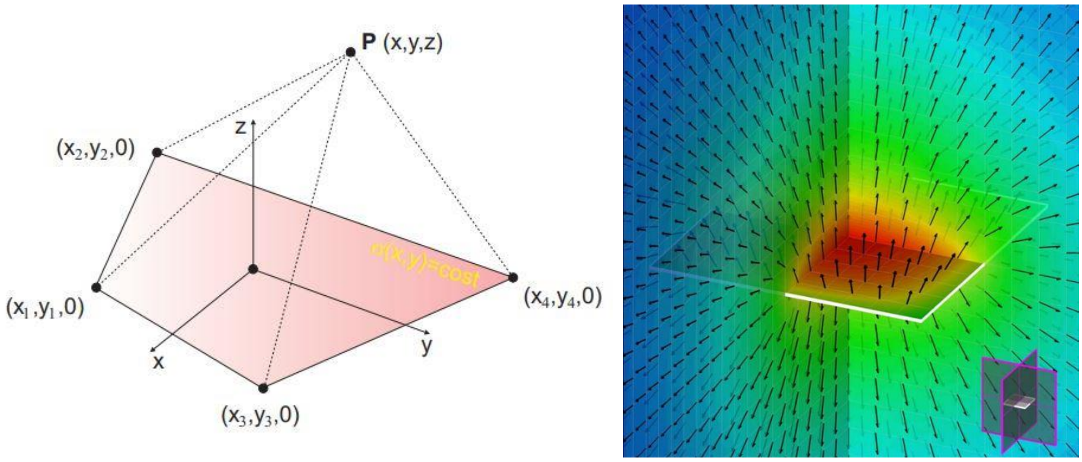

FIGURE 2. 12: Quadrilateral constant-strength source element (on the left) and flow-field induced by it (on the right).

Since – as previously discussed – each source element emits flow in all directions, it is straightforward that the resulting velocity will be away from the surface and hence a discontinuity in the w component, evaluated at $z = 0$ is generated, if the point of interest lies on the quadrilateral. For this reason, a pure-source distribution is suitable to model a symmetric flow-filed. In particular, denoting with the plus sign the upper side of the surface and with a minus the lower one, it could be proved that:

$$w(z = \pm 0) = \frac{\pm\sigma}{2} \qquad 2.70$$

Hence the discontinuity value across the surface amounts to:

$$\Delta w = w^+ - w^- = \sigma \qquad 2.71$$

Whereas by writing Eq. 2. 69 by means of the Hess and Smith procedure in function of the coordinates of the four quadrilateral vertexes, it can be demonstrated that the velocity component u and v are defined everywhere, except on the quadrilateral boundary.

The other limit case when $z = 0$ but P is outside of the quadrilateral is:

$$w(z = \pm 0) = 0 \qquad 2.72$$

A quadrilateral element with a constant-strength doublet distribution which points in the z-direction, and whose potential may be written as:

$$\phi(x,y,z) = -\frac{\mu}{4\pi}\iint_S \frac{dz}{r^3}\,dS \tag{2. 73}$$

is shown below.

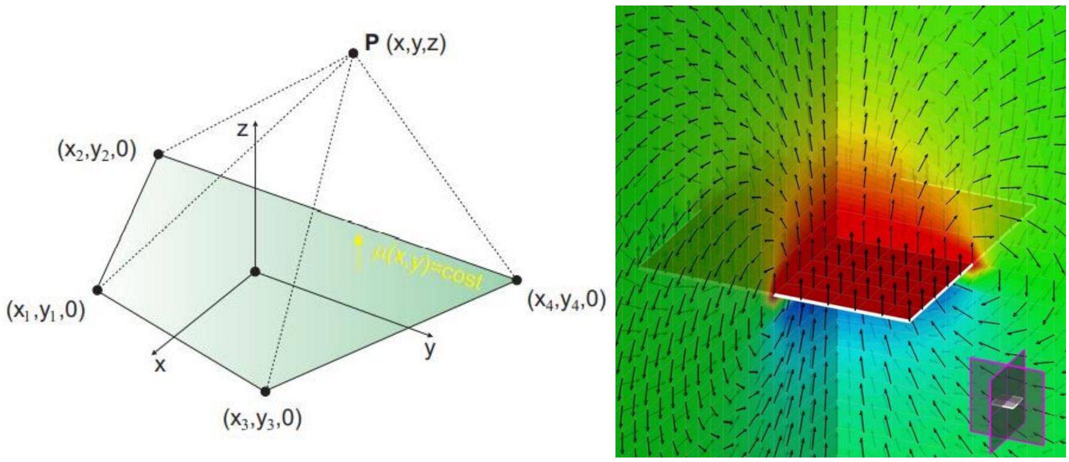

FIGURE 2. 13: Quadrilateral constant-strength doublet element (on the left) and flow-field induced by it (on the right).

The doublet potential may be developed from the source according to their relation through the gradient operator (2. 66) and thus, similarly to the source case, it is characterised by a discontinuity at $z = 0$:

$$\phi(z = \pm 0) = \frac{\pm\mu}{2} \tag{2. 74}$$

Finally, let us consider a constant-strength vortex filament of circulation Γ along the curve C bounding the panel. It can be demonstrated by exploiting the Stokes' theorem that the velocity induced by the vortex-ring – calculated as the sum of the components induced by its 4 sides by means of the Biot-Savart law – corresponds to the velocity of the doublet quadrilateral if $\Gamma = \mu = \Delta\phi$, confirming the equivalence that holds between a vortex distribution and a doublet one of higher order.

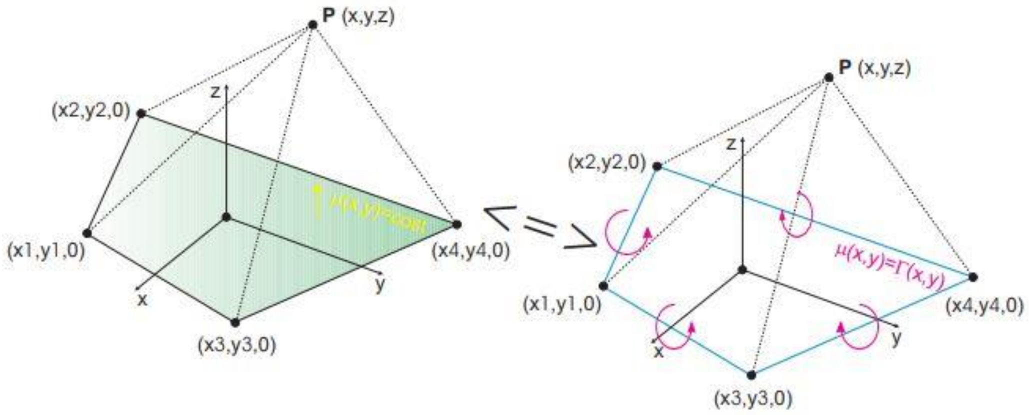

FIGURE 2. 14: Quadrilateral doublet element and its vortex ring equivalent.

2.10 Computation of the Velocity field

Once the singularity distribution strengths are known, it is possible to compute the total velocity in every point of the domain by taking the gradient of the scalar potential (Eq. 2. 52):

$$\underline{V}(P) = \underline{V_\infty}(P) - \iint_{S_b} \mu \, \underline{\nabla}\left(\underline{n} \cdot \underline{\nabla}\frac{1}{d}\right) dS + \iint_{S_b} \sigma \, \underline{\nabla}\frac{1}{d} \, dS - \iint_{S_w} \mu_w \, \underline{\nabla}\left(\underline{n} \cdot \underline{\nabla}\frac{1}{d}\right) dS$$

2. 75

Instead, when the point P lies on the boundary, it is necessary to consider equation 2. 53 and to use following equation:

$$\underline{V}(P \in S_b) = \underline{V_\infty}(P) - 2\iint_{S_b - P} \mu \, \underline{\nabla}\left(\underline{n} \cdot \underline{\nabla}\frac{1}{d}\right) dS + 2\iint_{S_b} \sigma \, \underline{\nabla}\frac{1}{d} \, dS$$
$$- 2\iint_{S_w} \mu_w \, \underline{\nabla}\left(\underline{n} \cdot \underline{\nabla}\frac{1}{d}\right) dS$$

2. 76

However, as the particular choice of the source values, it is possible to compute the velocity by taking the gradient of the potential in a local reference frame centred in the point of interest, as showed in Figure 2. 15. In fact, as the normal component of velocity disturbance has been established thanks to the source intensity, it is possible to compute the tangential ones by means of the derivatives of the doublet intensity:

$$\underline{v}(P) = v_{t_1}\underline{i_{t_1}} + v_{t_2}\underline{i_{t_2}} + v_n\underline{i_n} = \frac{\partial\mu}{\partial t_1}\underline{i_{t_1}} + \frac{\partial\mu}{\partial t_2}\underline{i_{t_2}} - \sigma\underline{i_n} \qquad 2.77$$

These components will be summed at the undisturbed local velocity in order to obtain the total velocity:

$$\underline{V}(P \in S_b) = \underline{V_\infty}(P) + \underline{v}(P) \qquad 2.78$$

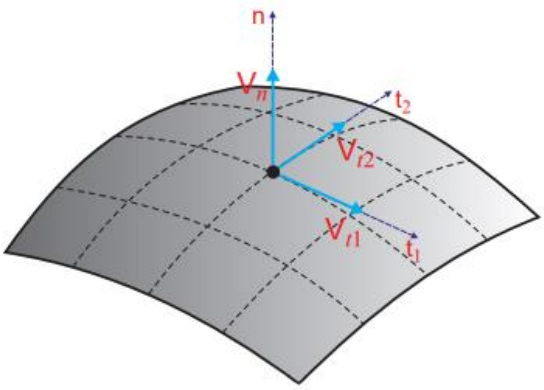

FIGURE 2. 15: Panel local reference frame for evaluating the normal and tangential velocity components.

2.11 Computation of Forces and Moments

Having found a solution to the Laplace's equation, so having determined the flow field, as previously stated, the pressure field can be computed by Bernoulli equation and after that, the aerodynamic forces and moments on the lifting body can be finally evaluated.

In general, the way the aerodynamic force takes place on a body moving through a still fluid is by means of two forces per unit area:

- the pressure distribution (normal to the surface)
- the shear stress distribution (acting tangentially, due to the frictional effect of the fluid flowing around the body)

over the body surface. Their integration all over gives as result the aerodynamic force $\underline{F}$ and moment $\underline{M}$ acting on the body of interest. Within the inviscid formulation, from the unsteady Bernoulli equation, those can be computed as follows:

$$\underline{F}(t) = \int_{S_b} \big(p_\infty(t) - p(t)\big)\underline{n}\, dS \qquad 2.\,79$$

$$\underline{M}(t) = \int_{S_b} \underline{r} \times [\big(p_\infty(t) - p(t)\big)\underline{n}]\, dS \qquad 2.\,80$$

where $\underline{r}$ depends on the reference point which the moment is calculated with respect of; in aeronautics the most common choice is the aerodynamic centre.

The resultant force can be usefully decomposed along the relative wind reference frame, thus obtaining the lift $\underline{L}$ – perpendicular to the wind flow – and the $\underline{D}$ – parallel instead. It is dutiful to point out that being the theory viscosity-free, the only computable contribution to the total drag is the one induced by the lift, *i.e.* D_i, whereas the skin friction drag D_f and the pressure drag D_p, due respectively to shear stresses at the wall and flow separation, are neglected.

In fluid-dynamics, it is a common practice to refer to non-dimensional coefficients, rather than dimensional forces and moments. Firstly, let us introduce the pressure coefficient C_p whose usefulness in aerodynamics is widely known:

$$C_p = \frac{p - p_\infty}{q_\infty} = \frac{p - p_\infty}{\frac{1}{2}\rho_\infty V_\infty^2} \qquad 2.\,81$$

By exploiting equation 2. 40 under the hypothesis of negligible mass forces (*e.g.* those due to the gravitational field – which implies no valuable fluctuation in height of fluid particles), the pressure coefficient can be evaluated in terms of the velocity and of unsteady variations of its potential:

$$C_p = 1 - \frac{V^2}{V_\infty^2} + \frac{\partial \phi}{\partial t}\frac{2}{V_\infty^2} \qquad 2.\,82$$

Similarly for lift, induced drag and moment coefficients:

$$C_L = \frac{L}{q_\infty S} = \frac{L}{\frac{1}{2}\rho_\infty V_\infty^2 S} \qquad 2.\,83$$

$$C_{D_i} = \frac{D}{q_\infty S} = \frac{D_i}{\frac{1}{2}\rho_\infty V_\infty^2 S} \qquad 2.\,84$$

$$C_M = \frac{M}{q_\infty Sc} = \frac{M}{\frac{1}{2}\rho_\infty V_\infty^2 Sc} \qquad 2.\,85$$

where S and c are the lifting body's area and chord of reference.

2.11.1 Trefftz technique

The approach just described to evaluate the aerodynamic forces through a direct integration of the pressure field over the body, may require a great number of panels, especially where pressure gradients are high, *i.e.* at the airfoil leading edge, in order to have an acceptable accuracy, above all with regard of the induced drag that is two orders of magnitude smaller than the lift. This may result in elevated computational times, partially mining one of the greatest advantages of the methods based on the Laplace's equation. Alternatively, another technique can be exploited to achieve the goal by means of an indirect analysis conducted in the Trefftz plane S_T, defined as the one located at an infinite distance downstream the body and perpendicular to its wake, as depicted in Figure 2. 16.

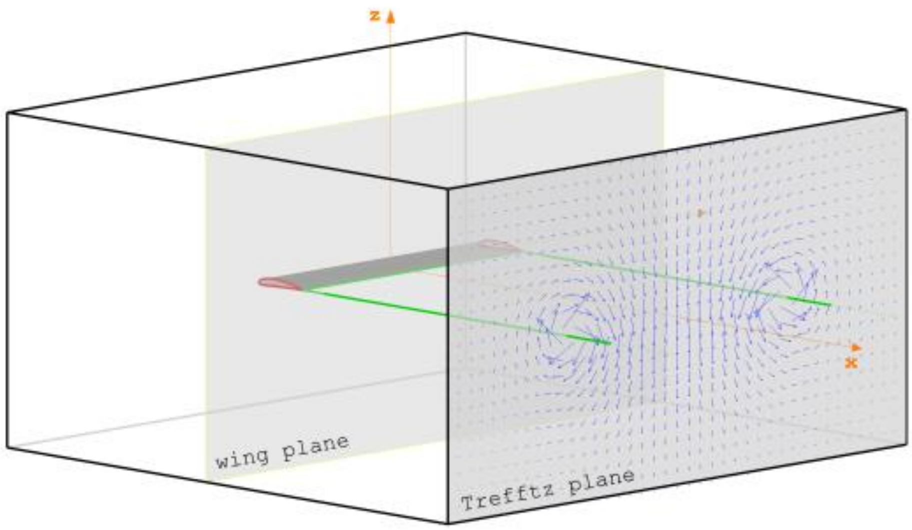

FIGURE 2. 16: Trefftz plane.

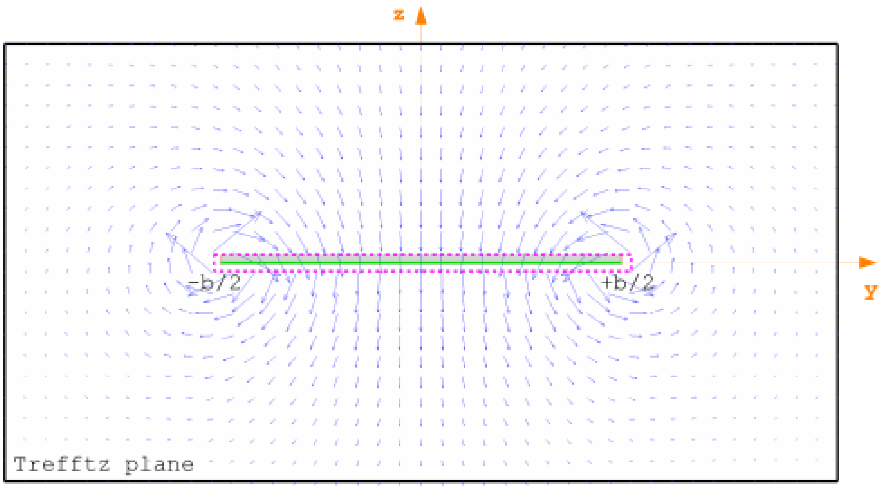

FIGURE 2. 17: Velocities induced onto the Trefftz plane.

Under the assumptions of incompressible and inviscid flow, whose vorticity is only enclosed in the thin wake, the integral form of the momentum equation, after having expressed the pressure by the steady Bernoulli equation with no mass forces, leads to:

$$\underline{F} = \iint_{S_\infty} \rho \underline{V} \left(\underline{V} \cdot \underline{n} \right) dS + \iint_{S_\infty} \frac{1}{2} \rho V^2 \, \underline{n} dS \qquad 2.86$$

Projecting it along the unperturbed wind-parallel x-axis, where to define the velocity field its decomposition into the far-field and the perturbation induced by the presence of the body has been emphasised so that $\underline{V} = (V_\infty + u, v, w)$, if the control volume is large enough so that the perturbation velocity components will vanish everywhere but on the wake, *i.e.* $u^2 \ll v^2, w^2$, and taking into account $\underline{V}$ is solenoidal, then (2. 86) yields:

$$D_i \approx \frac{\rho}{2} \iint_{S_T} (v^2 + w^2) \, \underline{n} dS, \qquad dS = dydz \qquad 2.87$$

A first issue is the evaluation of the far-away perturbations: this can be overcome by substituting the velocity disturb with its potential ϕ'. Then, thanks to the divergence theorem the surface integral and naming l_w the wake projection onto the Trefftz plane:

$$D_i \approx -\frac{\rho}{2} \int_{l_w} \Gamma(\mathrm{Y}) \, w \, dy \qquad 2.88$$

where Γ is the circulation evaluated on the l_w path and w the component of the velocity induced by the wake orthogonal to the wake itself.

The challenge of evaluating the line integral infinitely far away over a very large area still remains. The Trefftz analysis may be led in a *near-field* plane, if the doublets located nearby the wing TE are considered. In this context, according to the *lifting line* theory, evaluating the downwash at the start of a streamwise trailing vortex wake one obtains half of the downwash at the Trefftz plane (because the wake extends infinitely in both directions from the Trefftz plane but only in one direction from its start). As a consequence, the near-field technique differs from the classical far-field method by a factor $^1/_2$, *i.e.*

$$D_i \approx -\frac{\rho}{2}\int_{l_w}\Gamma(\mathrm{Y})\, w\, dy\Big|_{Trefftz} = -\rho\int_{-\frac{b}{2}}^{\frac{b}{2}}\Gamma(\mathrm{Y})\, w\, dy\Big|_{wing} \qquad 2.89$$

Moreover, this technique allows to avoid either the numerical issues that may arise whenever in the field there are some vortices located far away from the body and the difficulty in obtaining a regular shape at great distances far from the body both for time dependent and independent calculations. In fact, since the wake is inherently fluctuating, it may be hardly handled even for a steady case. Obviously, the same far-field technique can be employed to compute the lift:

$$L \approx \rho V_\infty \int_{l_w}\Gamma(\mathrm{Y})\, dy\Big|_{Trefftz} = 2\rho V_\infty \int_{-\frac{b}{2}}^{\frac{b}{2}}\Gamma(\mathrm{Y})\, dy\Big|_{wing} \qquad 2.90$$

CHAPTER 3

PANEL METHODS

3.1 Synopsis

In Chapter 2 it has been pointed out that a possible analytical technique to solve an inviscid, incompressible and irrotational flow field, either steady or unsteady – held by the Laplace's equation and an appropriate set of BCs – is by means of the Green's identities. The fluid field can be modelled using singularity entities located at the boundaries of the computational domain whose strength is unknown. This approach allows to face engineering problems otherwise impossible to study and, compared to those that are aimed to solve the fluid-dynamic equation in the whole flow-field (*e.g.* finite-difference methods), it appears to be much more cost-effective in terms of computational resources. Nevertheless, the limitations due to the simplifying assumptions employed should be kept in mind, since the introduction of other techniques is related to the need to treat more complex (*e.g.* viscous or compressible) situations.

3.2 Numerical Procedure

Solving the mathematical problem presented above is not unchallenging, since it is required for equations 2. 54 and 2. 60 to be satisfied and enforced in each point belonging to the boundary surface. Obviously this cannot be achieved in a real problem, so that, in practice, those could be specified just in a limited number of points (called either *collocation* or *control points*), resulting thus in a set of linear algebraic equations.

From the numerical point of view, a solution can be obtained if body and wake geometries are discretized separately into a proper number of quadrilateral and/or triangular elements called *panels*, after which the method is named. N_b the number of body surface panels, N_w the wake panels. These quadrilateral regions, identified by *grid points*, are described by a function $z = f(x, y)$. For simplicity, f is usually in the form of a piecewise polynomial: the higher the order, the greater the accuracy level to reproduce the real geometry. In particular, due to increasing computational cost, typically the most employed polynomials are of the first order:

$$z = a_0 + b_1 x + b_2 y \qquad 3.1$$

where a, b_1 and b_2 are constant.

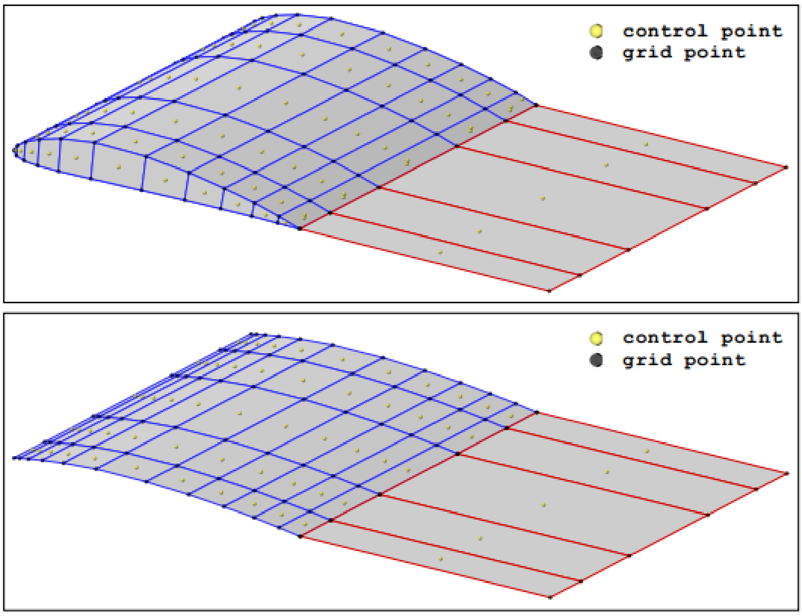

FIGURE 3. 1: Examples of discretised (thick – above – and thin – below) body and wake geometry.

Howbeit, since in general the three-dimensional real geometry is characterized by two different principal radii of curvature, the discretization could rise some issues, such as the one depicted in Figure 3. 2, where a leakage flow does occur. This problem may result in difficulties in specifying the BC, since the leakage between adjacent panels could compromise the satisfaction of zero normal flow across the boundary, for instance.

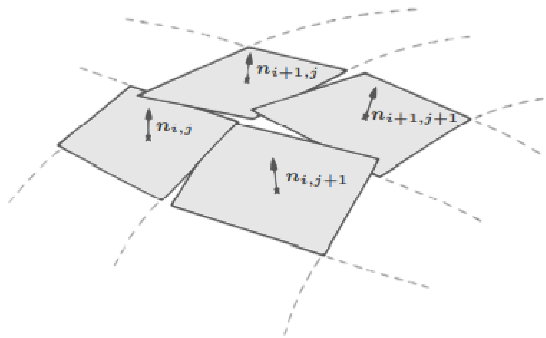

FIGURE 3. 2: Leakage flow that arises from discretisation issues.

Aside with the geometry and wake discretization, a similar process is required for the singularity distribution. This task is typically accomplished by means of polynomial approximations either: the singularity strength may be assumed constant (low-order), linearly variable (first order) or parabolic (second order). It should be underlined that the level of approximation employed for both geometry and singularities should be the same, since the lowest order rules and no gain in accuracy is obtained despite a greater computational effort. The most common choice is constant-strength singularities over flat quadrilateral panel with straight borders. This discretization allows to have a notable simplification in calculus and in numerical implementation, although requires several panels in order to compensate the loss in accuracy due to a low polynomial order.

The Boundary Condition, either Dirichlet (Eq. 2. 54) or Neumann (Eq. 2. 60), will be enforced at the control point of each panel, automatically individuated as its centroid – N_b^D of Dirichlet type and N_b^N of Neumann type. Let J be the panel's collocation point where the BC is imposed and r_J the distance of J to the panel where the effect is going to be computed:

$$\sum_{K=1}^{N_b} \iint_{panel\ K} \mu_K \underline{n} \cdot \underline{\nabla} \frac{1}{r_J} dS + \sum_{L=1}^{N_w} \iint_{panel\ L} \mu_L^w \underline{n} \cdot \underline{\nabla} \frac{1}{r_J} dS = \sum_{K=1}^{N_b} \iint_{panel\ K} \sigma_K \frac{1}{r_J} dS$$

$$J = 1, \dots, N_b^D \qquad 3.2$$

$$\sum_{K=1}^{N_b} \underline{n}_J \cdot \iint_{panel\ K} \mu_K \underline{\nabla} \left(\underline{n} \cdot \underline{\nabla} \frac{1}{r_J} \right) dS + \sum_{L=1}^{N_w} \underline{n}_J \cdot \iint_{panel\ K} \mu_L^w \underline{\nabla} \left(\underline{n} \cdot \underline{\nabla} \frac{1}{r_J} \right) dS$$
$$= \sum_{K=1}^{N_b} \underline{n}_J \cdot \iint_{panel\ K} \sigma_K \underline{\nabla} \frac{1}{r_J} dS - \underline{n}_J \cdot \left(\underline{V} - \underline{V_\infty} \right)_J$$

$$J = 1, \dots, N_b^N \qquad 3.3$$

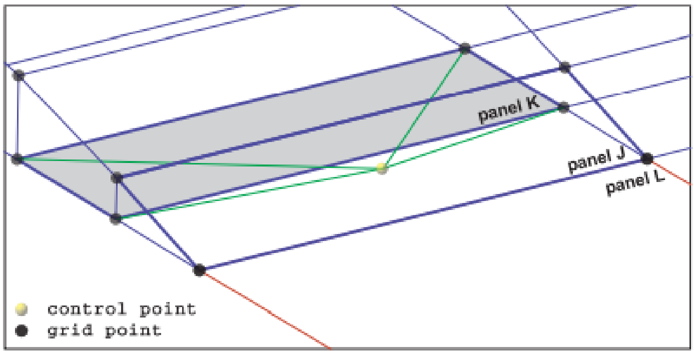

FIGURE 3. 3: Influent coefficients: how they work.

The integrals in the above equations are computed over the single panel surface, and each one represents the influence that the generic panel *K* or *L* produces on the control point of the panel *J*. Moreover, as illustrated in Figure 3. 3, these integrals may be substituted through the Hess and Smith procedure with summations extended to the corresponding grid points. For those elements whose singularity strengths are constant and unitary, this influence is only due to the panel geometry and it may be synthesised using some coefficients, called *influence coefficients*:

$$B_{JK}^D = \iint_{panel\ K} \frac{1}{r_J} dS \qquad 3.4$$

$$B_{JK}^{N} = \underline{n}_J \cdot \iint_{panel\,K} \underline{\nabla}\frac{1}{r_J}\,dS \qquad 3.5$$

$$C_{JK}^{D} = \iint_{panel\,K} \underline{n} \cdot \underline{\nabla}\frac{1}{r_J}\,dS \qquad 3.6$$

$$C_{JK}^{N} = \underline{n}_J \cdot \iint_{panel\,K} \underline{\nabla}\left(\underline{n} \cdot \underline{\nabla}\frac{1}{r_J}\right)dS \qquad 3.7$$

where the apexes *D* and *N* are always indicative of the imposed condition type.

Therefore, equations 3. 2 and 3. 3 become:

$$\sum_{K=1}^{N_b} \mu_K\, C_{JK}^{D} + \sum_{L=1}^{N_w} \mu_L^w\, C_{JK}^{D} = \sum_{K=1}^{N_b} \sigma_K B_{JK}^{D}$$
$$J = 1, \dots, N_b^D \qquad 3.8$$

$$\sum_{K=1}^{N_b} \mu_K C_{JK}^{N} + \sum_{L=1}^{N_w} \mu_L^w C_{JK}^{N} = \sum_{K=1}^{N_b} \sigma_K B_{JK}^{N} - \underline{n}_J \cdot \left(\underline{V} - \underline{V_\infty}\right)_J$$
$$J = 1, \dots, N_b^N \qquad 3.9$$

According to Eq. 2. 56, the strength of the sources is assigned for thick bodies or fixed to zero for thin bodies, so the influence coefficients B_{JK}^{D} and B_{JK}^{N} can be computed, letting the doublet-related terms still unknown. Moreover, as already described in paragraph 2.7, having imposed the Kutta condition at the TE, the strength of the wake doublets μ_L^w can be written as functions of the unknown intensities of the respective body doublets μ_K. In fact, in case of thick bodies, each wake panel shares one side with a trailing edge body panel. Let μ_L^u and μ_L^l be respectively the doublet strength of the upper panel and the lower panel, the Kutta BC yields:

$$\mu_L^w = \mu_L^u - \mu_L^l \qquad 3.10$$

In contrast, as for bodies with no thickness, there is no difference between upper and lower, therefore:

$$\mu_L^w = \mu_L^u \qquad 3.11$$

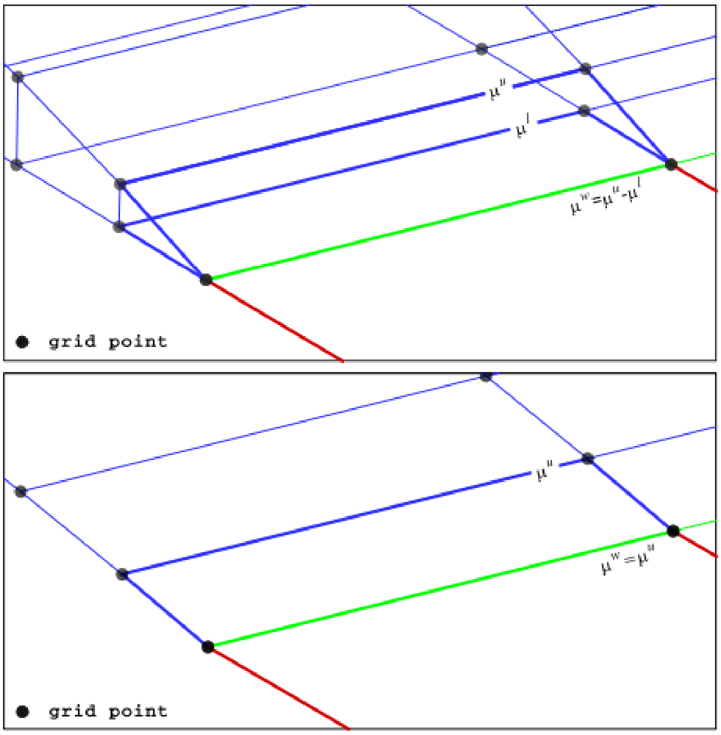

FIGURE 3. 4: References for the Kutta condition in case of thick bodies (above) and thin ones (below).

So the influence of a generic panel wake becomes:

$$C_{JL}^{D}\mu_{L}^{w} = C_{JL}^{D}(\mu_{L}^{u} - \mu_{L}^{l}) \qquad \textit{thick bodies} \qquad 3.\ 12$$

$$C_{JL}^{N}\mu_{L}^{w} = C_{JL}^{N}\mu_{L}^{u} \qquad \textit{thin bodies} \qquad 3.\ 13$$

And it can be led back to the body panel doublet at the TE, by simply correcting the coefficients C_{JK}^{D} and C_{JK}^{N} in this way:

$$A_{JK}^{D} = \begin{cases} C_{JK}^{D} & \textit{panel K not at the TE} \\ C_{JK}^{D} - C_{JL}^{D} & \textit{upper panel K at the TE} \\ C_{JK}^{D} + C_{JL}^{D} & \textit{lower panel K at the TE} \end{cases} \qquad 3.\ 14$$

$$A_{JK}^{N} = \begin{cases} C_{JK}^{N} & \textit{panel K not at the TE} \\ C_{JK}^{D} + C_{JL}^{D} & \textit{panel K at the TE} \end{cases} \qquad 3.\ 15$$

Finally:

$$\sum_{K=1}^{N_b} \mu_K\, A_{JK}^D = \sum_{K=1}^{N_b} \sigma_K B_{JK}^D \qquad J = 1, \dots, N_b^D \tag{3.16}$$

$$\sum_{K=1}^{N_b} \mu_K A_{JK}^N = \sum_{K=1}^{N_b} \sigma_K B_{JK}^N - \underline{n}_J \cdot \left(\underline{V} - \underline{V_\infty}\right)_J \qquad J = 1, \dots, N_b^N \tag{3.17}$$

An additional condition to 3. 16 and 3. 17 is required in case of free wake: it may be imposed by annulling the normal velocity component in each control points of the wake:

$$\underline{V} \cdot \underline{n}_L = 0 \qquad L = 1, \dots, N_w \tag{3.18}$$

Equations 3. 17 and 3. 18, written for each control point of the body, lead to a set of N_b linear algebraic equations with N_b unknowns which are the body surface doublet strengths μ_K:

$$\begin{pmatrix} A_{1,1}^D & A_{1,2}^D & \cdots & A_{1,N_b}^D \\ A_{2,1}^D & A_{2,2}^D & \dots & A_{2,N_b}^D \\ \vdots & \vdots & & \vdots \\ A_{N_b,1}^N & A_{N_b,2}^N & \dots & A_{N_b,N_b}^N \end{pmatrix} \begin{pmatrix} \mu_1 \\ \mu_2 \\ \vdots \\ \mu_{N_b} \end{pmatrix} = \begin{pmatrix} B_{1,1}^D & B_{1,2}^D & \cdots & B_{1,N_b}^D \\ B_{2,1}^D & B_{2,2}^D & \dots & B_{2,N_b}^D \\ \vdots & \vdots & & \vdots \\ B_{N_b,1}^N & B_{N_b,2}^N & \dots & B_{N_b,N_b}^N \end{pmatrix} \begin{pmatrix} \sigma_1 \\ \sigma_2 \\ \vdots \\ \sigma_{N_b} \end{pmatrix} - \begin{pmatrix} 0 \\ 0 \\ \vdots \\ (V_n - V_{n\infty})_{N_b} \end{pmatrix} \tag{3.19}$$

Furthermore, it should be pointed out that employing the decomposition of the total potential Φ into a free-stream contribution ϕ_∞ and a perturbation one ϕ, jointly with the choice $\Phi_i = \phi_\infty$ (see paragraph 2.8), results into relatively small values of μ, and hence the problem 3. 19 is expect to be stable.

The numerical procedure aimed at the resolution of a steady surface singularity distribution problem described in this section has been summarised below.

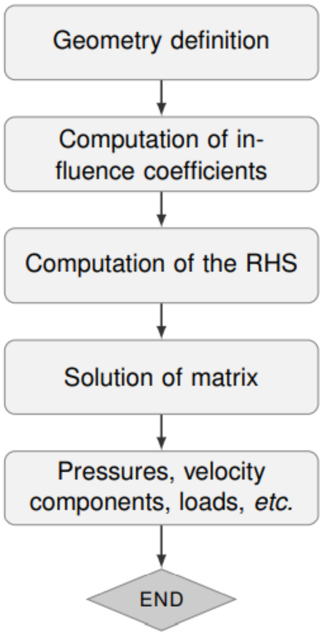

FIGURE 3. 5: Numerical procedure to solve a steady surface singularity distribution problem.

3.2.1 Unsteady Panel Methods

Although the method just presented holds for steady flows only, it can be made more general by introducing a time-dependency through the BCs and the unsteady formulation of the Bernoulli equation.

Time is discretised as well as geometry in *time-steps* Δt whose amplitude is not necessarily constant. As depicted in Figure 3. 6, in unsteady panel methods the procedure summarised in Figure 3. 5, is embedded into a time stepping loop, starting from $t = 0$. The unsteady solution is obtained by repeating the loop as many times as many time-steps have been considered. At each time-step boundary conditions have been updated in time and a new row of wake panels is shed.

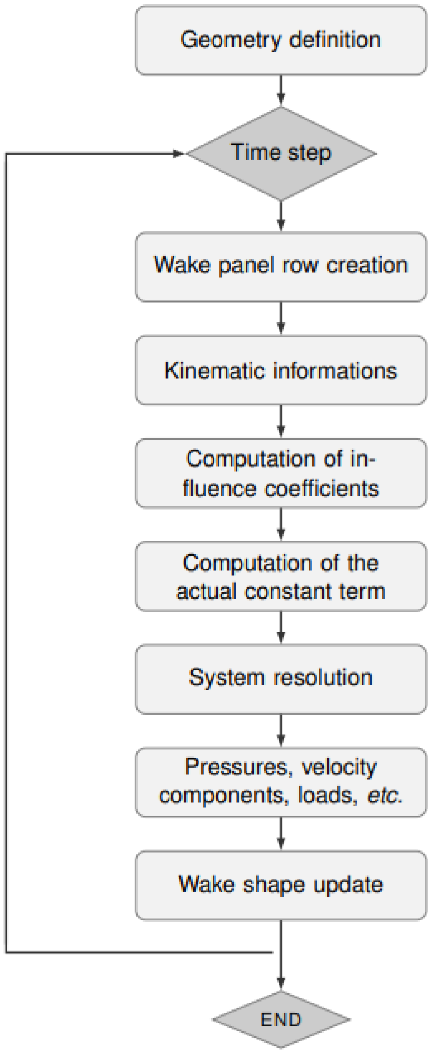

FIGURE 3. 6: Numerical procedure to solve an unsteady surface singularity distribution problem.

The choice of the coordinate systems is very important for the formulation of the unsteady problem. In order to prescribe correctly the boundary conditions on the solid body surfaces, consider a body-fixed coordinate system *(0, x, y, z)* and a fixed-in-space global reference frame *(0, X, Y, Z)*. Supposing the body motion law to be known, the normal flow boundary condition on the surface becomes:

$$\frac{\partial \phi}{\partial t} = (\underline{V_\infty} - \underline{V_r} - \underline{\Omega} \times \underline{r}) \cdot \underline{n}$$

where $\underline{r} = \underline{r}(x, y, z)$, $\underline{V_r}$ and $\mathbf{\underline{\Omega}}$ identify the position of any point in the body reference frame, the relative velocity and the angular speed of the moving coordinate system, respectively.

Supposing that at the time $t = 0$ the two reference frames introduced above are coincident, the calculation starts at the time $t = \Delta t$, where Δt is the duration of a time-step. That is to say that the first row of wake panels is generated near the TE and their strengths can be therefore evaluated by means of the Kutta condition. Once the first row of wake panels has been shed, similar developments of those applied in the previous paragraph (Figure 3. 5) can be carried out. At $t = 2\Delta t$ the second time-step begins and a new wake panel row is created. In order to achieve this task, since a relative motion between the two different coordinate systems here taken into account has occurred, the row generated in the previous time-step should be considered fixed with respect to the inertial frame (O, X, Y, Z). In fact, in this way a gap between the actual TE and the existing wake panels takes place and will be filled with the new shedding wake row that, being adjacent to the TE as well as the one created at the first time-step, can be evaluated by means of the Kutta condition, once again. It has to be highlighted that, at each time-step, only the wake panel row to be computed has its singularity strengths unknown, whereas all the others keep the values previously evaluated.

Moreover, it should be pointed out that, typically, the characteristic length of the wake panels adjacent to the TE amounts to 0.2 ÷ 0.3 times the space travelled by the TE itself in a time Δt (*i.e.* $V_\infty \Delta t$) in order to minimise the numerical error introduced having discretised the wake.

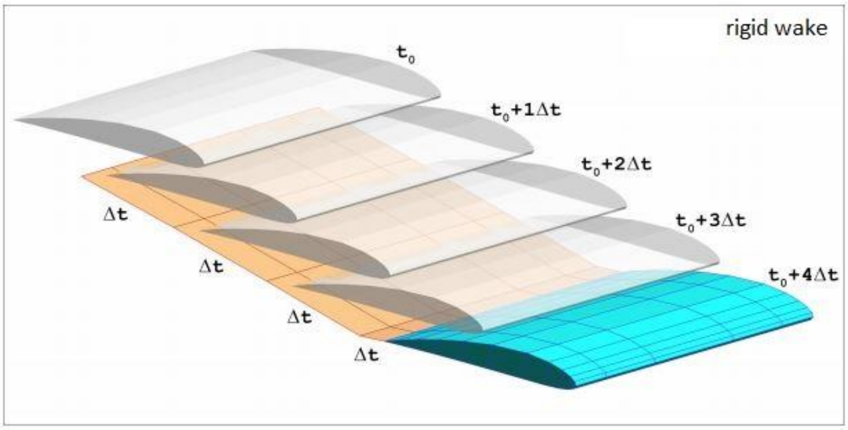

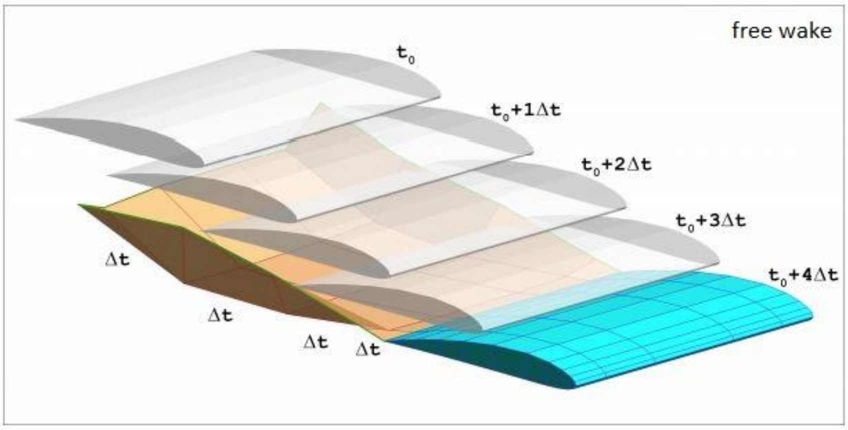

FIGURE 3. 7: Creation of a rigid (above) and a flexible (below) unsteady wake.

Let N_{ts} be the time-step which the solution is going to be computed at and M_w the number of wake panels formed at each time step. Equations 3. 17 and 3. 18 are corrected in this way:

$$\sum_{K=1}^{N_b} \mu_K A_{JK}^D = \sum_{K=1}^{N_b} \sigma_K B_{JK}^D - \sum_{I=1}^{N_{ts}-1} \sum_{L=1}^{M_w} C_{JIL}^D \mu_{IL}^w \qquad J = 1, \dots, N_b^D \tag{3. 20}$$

$$\sum_{K=1}^{N_b} \mu_K C_{JK}^N = \sum_{K=1}^{N_b} \sigma_K B_{JK}^N - \sum_{I=1}^{N_{ts}-1} \sum_{L=1}^{M_w} C_{JIL}^N \mu_{IL}^w - \underline{n}_J \cdot \left(\underline{V} - \underline{V_\infty}\right)_J \qquad J = 1, \dots, N_b^N \tag{3. 21}$$

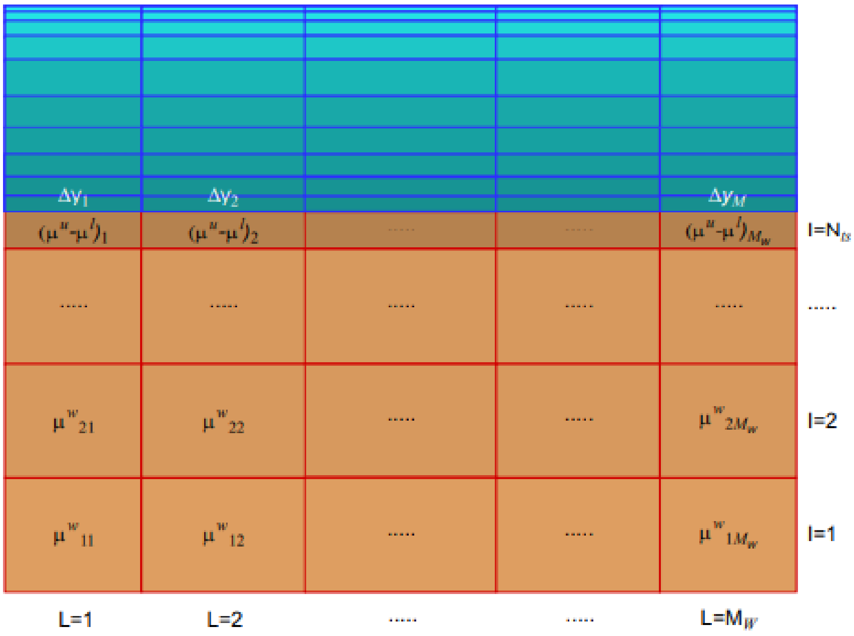

FIGURE 3. 8: References for the wake panel indices.

Clearly, equations 3. 20 and 3. 21 are valid for any choice of N_{ts}, supposing that the wake has been solved in all the previous $N_{ts}-1$ time-steps; particularly, equations 3. 20 and 3. 21 correspond to equations 3. 16 and 3. 17 when $N_{ts}=1$, respectively.

As far as the constraint related to the shape of the wake is concerned, if the wake is flexible, it will be necessary to evaluate the velocity field at each wake panel's grid point and/or control point and to deform these panels in order to fulfil equation 3. 18 correctly. In case of rigid wake, the problem is linearised imposing the wake geometry (*i.e.* the local flow field cannot influence the wake). The wake model might also be a combination of the two.

3.2.2 Computation of velocities and forces

For the computation of the total velocity at any point P belonging to the fluid field, equation 2. 75 should be rewritten in a discrete formulation:

$$\underline{V}(P) = \underline{V_\infty}(P) - \sum_{K=1}^{N_b} \mu_K \underline{V_K^\mu} + \sum_{K=1}^{N_b} \sigma_K \underline{V_K^\sigma} - \sum_{K=1}^{N_b} \mu_K^w \underline{V_K^\mu} \qquad 3.\,22$$

where the coefficients

$$\underline{V}_K^{\sigma} = \iint_{panel\ K} \underline{\nabla}\frac{1}{d}\,dS \qquad 3.23$$

$$\underline{V}_K^{\mu} = \iint_{panel\ K} \underline{\nabla}\left(\underline{n}\cdot\underline{\nabla}\frac{1}{d}\right)dS \qquad 3.24$$

have the same physical meaning of 3. 6 and 3. 7.

Similarly, if P lies on the boundary surface, equation 2. 76 should be evaluated at the grid points and the control points. However, the use of equation 2. 77 is more advantageous and the computation of the tangential components of the velocity perturbation may be derived from a scheme such as the one reported in Figure 3. 9 which is extremely simple:

$$v_{t_1} = \frac{\mu(J_3)-\mu(J_1)}{d_1+d_3} \qquad 3.25$$

$$v_{t_2} = \frac{\mu(J_4)-\mu(J_2)}{d_2+d_4} \qquad 3.26$$

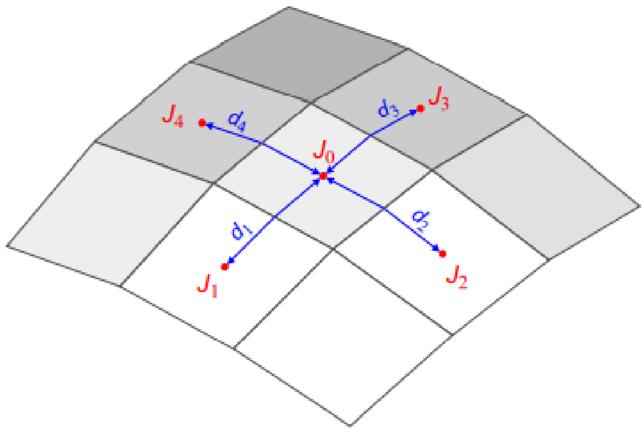

FIGURE 3. 9: Computational scheme for the tangential velocity perturbation.

In reality, the panel distribution is not as regular as in the picture and more complex computational techniques are required, for example by building a doublet strength distribution function on a large number of control points chosen in the nearby point of interest.

Now it is possible to compute the discrete pressure distribution or, alternatively, the pressure coefficient:

$$p = p_\infty + \frac{1}{2}\rho_\infty (V_\infty^2 - V^2) - \rho_\infty \frac{\mu(t) - \mu(t-\Delta t)}{\Delta t} \tag{3. 27}$$

$$C_p = 1 - \frac{V^2}{V_\infty^2} + \frac{\mu(t) - \mu(t-\Delta t)}{\Delta t}\frac{2}{V_\infty^2} \tag{3. 28}$$

and then the force acting on each body panel:

$$\underline{F} = \sum_{K=1}^{N_b} p_K \underline{n} S_K \tag{3. 29}$$

In some circumstances, the forces acting on the body can be evaluated by means of the near field Trefftz analysis. The integrals in (2. 89) and (2. 90) become summations over the wake panels at the trailing edge:

$$D_i \approx \rho \sum_{L=1}^{M_w} \mu_{N_{ts}L}^{w} w_L \Delta y_L \tag{3. 30}$$

$$L \approx 2\rho V_\infty \sum_{L=1}^{M_w} \mu_{N_{ts}L}^{w} \Delta y_L \tag{3. 31}$$

3.3 Vortex Particle Method

Hitherto the present dissertation has dealt with a panel-only representation of the wake shed at the back of an aerodynamic body, though this choice is not the only one possible. In particular, this paragraph is aimed to define the concept of *vorton* (also known as *vortex particle*): a three dimensional point vortex singularity whose cluster is equivalent to a wake panel. This singularity is employed in the so called *Vortex Particle Methods* to model the domain vorticity lying only on the thin wake, rather than – as usual in 3D problems – either vortex sheets or doublet panels.

The vorton methods have been introduced in the computational aerodynamics in order to overcome one of the main limits inherent the panel methods in their classical formulation: the intersection of the wake with downstream body surfaces. In fact, whenever a doublet wake intersects with a downstream body (*e.g.* the wing portion located downstream with respect to a propeller), the physical meaning of the solution to the potential flow problem is irremediably lost. Moreover vorton methods allow to reduce the numerical instabilities related to discretized vortex sheets, do not require an excessively high density of vortex particle on equal accuracy terms and do not require elevated computational times.

3.3.1 Formulation

Consider a vorticity region of volume $\mathcal{V}$ discretized in a set of cubes whose side length is denoted by h. By this decomposition a vorton can be simply defined as a three-dimensional point vortex which discretises the vorticity field:

$$\underline{\omega}(\underline{r}, t) = \sum_P \underline{\omega_P}(t) h^3 \delta(\underline{r} - \underline{r_P}(t)) = \sum_P \underline{\alpha_P}(t) \delta(\underline{r} - \underline{r_P}(t)) \qquad 3.32$$

where $\underline{\alpha_P}(\underline{r}, t)$ is the vorton vector, given by the product of the vorticity times the volume of the element (*i.e.* $\underline{\alpha_P} = \underline{\omega_P} h^3$), $\underline{r}$ is the position vector of the evaluation point, $\underline{r_P}$ is the one related to the location of the P^{th} vortex particle and $\delta(\underline{r})$ the three-dimensional delta function. Therefore a vorton is a vector quantity identified by a position vector $\underline{r_P}$, a strength vector $\underline{\alpha_P}$ and eventually a core radius.

In Figure 3. 10 the equivalence between a vortex tube with constant cross-sectional area and a vorton is depicted. Obviously a single vortex tube may be discretised into several vortex particles and, consequently, a vorton may be thought as a small section of a vortex tube.

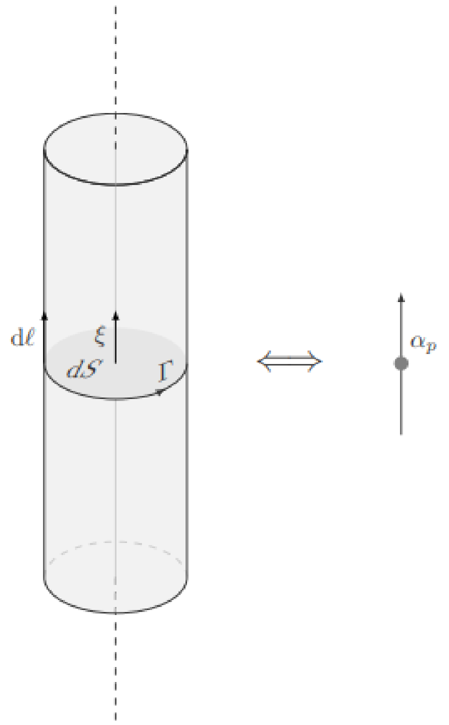

FIGURE 3. 10: Vortex tube and its corresponding vorton.

Furthermore, even though in equation 3. 32 the velocity field $\underline{V}(\underline{r},t)$ is clearly not given, its vorticity induced component V_ψ (see Eq. 2. 25) can be computed by taking the curl of the stream function $\underline{\psi}(\underline{r},t)$ which solves the Poisson's equation (2. 33). In particular, it could be proved that the vector potential may be written in the form:

$$\underline{\psi}(\underline{r},t) = \frac{1}{4\pi}\sum_P \frac{\underline{\alpha_P}(t)}{\left|\underline{r}-\underline{r_P}(t)\right|} \tag{3. 33}$$

It appears to be clear that (3. 33) is singular for $\left|\underline{r}-\underline{r_P}(t)\right| = 0$ and hence a core-function ξ_ψ is required to make the vector potential regular as $\left|\underline{r}-\underline{r_P}(t)\right| \rightarrow 0$. Be σ the core-radius associated to the vorton and r_σ the ratio of the absolute distance of the evaluation point from the vortex particle core to σ (*i.e.* $r_\sigma = \frac{\left|\underline{r}-\underline{r_P}(t)\right|}{\sigma}$), the core-function ξ_ψ is such that, when $r_\sigma < 1$, the vector potential $\underline{\psi}$ decays linearly to zero. Moreover, it should be noted that, in order to preserve the form (3. 33) and being

$$\underline{\psi_\sigma}(\underline{r},t) = \frac{1}{4\pi}\sum_P \frac{\underline{\alpha_P}(t)}{\left|\underline{r}-\underline{r_P}(t)\right|}\xi_\psi \tag{3. 34}$$

ξ_ψ has to approach the unity for values of r_σ greater than one. A wide variety of core-functions do exist. For example, the one represented in Figure 3. 11 is the Gaussian smoothing function that reaches the unity for about $r_\sigma > 1.5$ ($\xi_\psi = 1 - e^{-q r_\sigma}$, $q = 1.354 + 0.842 r_\sigma + 0.559 r_\sigma^2$).

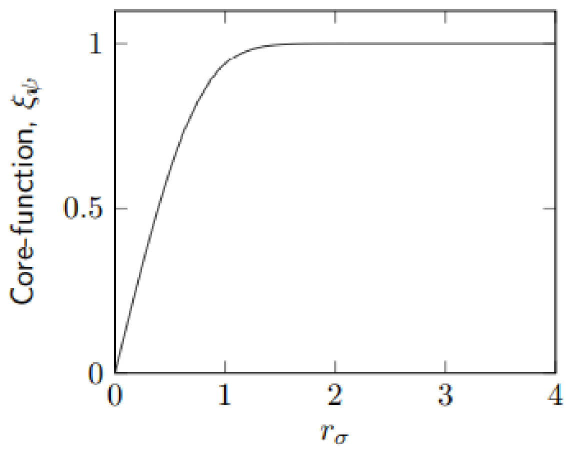

FIGURE 3. 11: Gaussian core function.

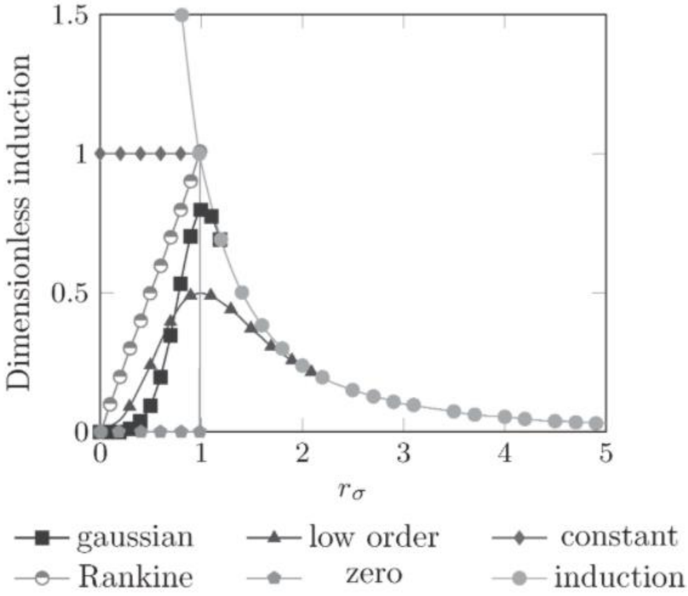

FIGURE 3. 12: Core function employed in PaMS.

Taking into account the definitions (2. 25) and (3. 33) for a single vorton, the velocity field magnitude decays as $1/\left|\underline{r}-\underline{r_P}(t)\right|^2$ as illustrated in Figure 3. 12 and Figure 3. 13, and as well as the vector potential, is singular for $\left|\underline{r}-\underline{r_P}(t)\right| = 0$, so a core-function ξ_V similar to the one already introduced for $\underline{\psi}$ is required.

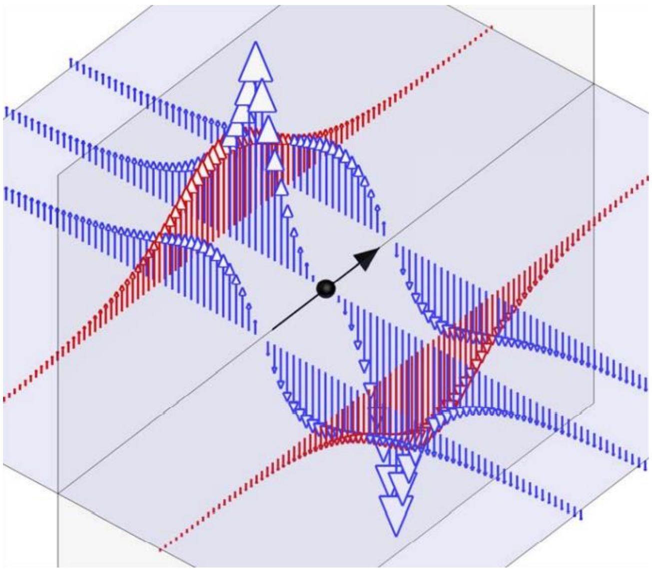

FIGURE 3. 13: Flow field induced by a vorton: velocity decay along the vorton axis in red, velocity decay normal to the vorton axis in blue.

A peculiar characteristic of the vortons is that these elements are governed by the vorticity evolution equation (2. 19) and hence each vortex particle is convected by the local velocity and stretched by the local velocity gradient. In particular, in this context the vortex stretching term is:

$$\underline{\nabla}\left(\underline{\nabla} \times \underline{\psi}(\underline{r}, t)\right) = \frac{1}{4\pi} \sum_P \underline{\nabla}\left[\underline{\nabla}\left(\frac{1}{\left|\underline{r} - \underline{r_P}(t)\right|}\right) \times \underline{\alpha_P}(t)\right] \tag{3. 35}$$

At this point, it should be noted that the particle vorticity field (3. 32) is not divergence-free. This fact makes the method inconsistent in a certain way, because a basis which is not divergence-free is employed to represent a vector field that should be solenoidal for all times. Similarly, since the Poisson's equation is solved with $\underline{\omega}$ generally not divergence-free, the vector potential is also not generally solenoidal.

Of particular interest in the scope of this thesis is the conversion of a wake modelled by means of doublet panels (or equivalent vortex rings) into vortex particles, that is to say how to assign the strength to a vorton so that the vorticity region it represents is equivalent to the one modelled through a common panel element. A possible conversion approach is made of three different steps:

- determine the equivalent vortex representation for each doublet panel to be converted into vortex particles;
- establish the number of vortons to be emitted from each panel;
- divide the panel into equal area segments and generate a vortex particle at the centroid of each of the segments.

Therefore, the vorton strength vector $\underline{\alpha_P}$ can be evaluated by integrating the strength of the vortex line surrounding each panel area segment, *i.e.*

$$\underline{\alpha_P}(\underline{r}, t) = \oint_{S_P} \Gamma(t) \underline{dl} \tag{3. 36}$$

and again, taking into account equations (2. 25) and (3. 33), the rotational velocity field may be calculated as a linear combination of a set of velocities induced by the vortons (Eq. 3. 32).

A consequence of the velocity locally induced by a vortex particle is that the vortons themselves are characterized by a time evolution, consisting on a change in time of strength and position. These two effects can be respectively written, in a Lagrangian representation, as:

$$\frac{D\underline{r_P}}{Dt} = \underline{V_P}\left(\underline{r_P}(t), t\right) \tag{3.37}$$

$$\frac{D\underline{\alpha_P}}{Dt} = \underline{\alpha_P}(t) \cdot \underline{\nabla}\underline{V_P}\left(\underline{r_P}(t), t\right) \tag{3.38}$$

At this point, the evolution equations of the vortons are discretised using a forward Eulerian scheme. Firstly, the vorton position is updated:

$$\underline{r_P}(t + \Delta t) = \underline{r_P}(t) + \underline{V_P}\left(\underline{r_P}(t), t\right)\Delta t \tag{3.39}$$

And then, the vorton strength:

$$\underline{\alpha_P}(t + \Delta t) = \underline{\alpha_P}(t) + \underline{\alpha_P}(t) \cdot \underline{\nabla}\underline{V_P}\left(\underline{r_P}(t), t\right)\Delta t \tag{3.40}$$

Clearly, the use of higher order time stepping method will be beneficial for a solution accuracy increase.

3.3.2 Transformation of Wake Panels into Vortons

It has been already highlighted that the VPM can be efficaciously employed to model the thin wake in three dimensional, unsteady, inviscid and incompressible flows since they are easier to handle with respect to the classical panel methods. In fact if for a doublet wake the evaluation of the flow field induction is computed on the four segments of each quadrilateral panel, in a vorton method the induction is due only to a point for each vortex particle. Hence, the vorton method results to be more attractive because it has also the advantage that the vorton elements are somehow independent as they do not necessarily belong to a specific wake panel at every time-step.

Now, the goal of this paragraph is to describe the conversion of the wake panels into vortons for an unsteady wake model which consists of a distribution of panels and a distribution of vortons.

A vorton wake model consists of two parts: a near wake and a far wake. The former (trailing every lifting surface) is made of a doublet sheet with as many panels as the wing TE spanwise and at least two rows of panels streamwise. In particular, the wake panels of the first row (*i.e.* the one closer to the TE) have strengths unknown that is going to be determined by the fulfilment of the Kutta condition and a characteristic length of $c_w V_\infty \Delta t$ where $c_w = 0.2 \div 0.3$, as seen in the section above. Whereas the second row of the wake buffer has known strengths corresponding to the trailing edge potential jump evaluated at the previous time-step and a length of $V_\infty \Delta t$ ($c_w = 1$). At this stage, it should be clear that the doublet buffer wake is required in order to achieve the closure of the potential problem through the imposition of the Kutta condition. By contrast, the far wake region is modelled through vortex particles: at each time-step, the previous time-step second row of wake panels is converted into vortons. This wake decomposition is presented in Figure 3. 14.

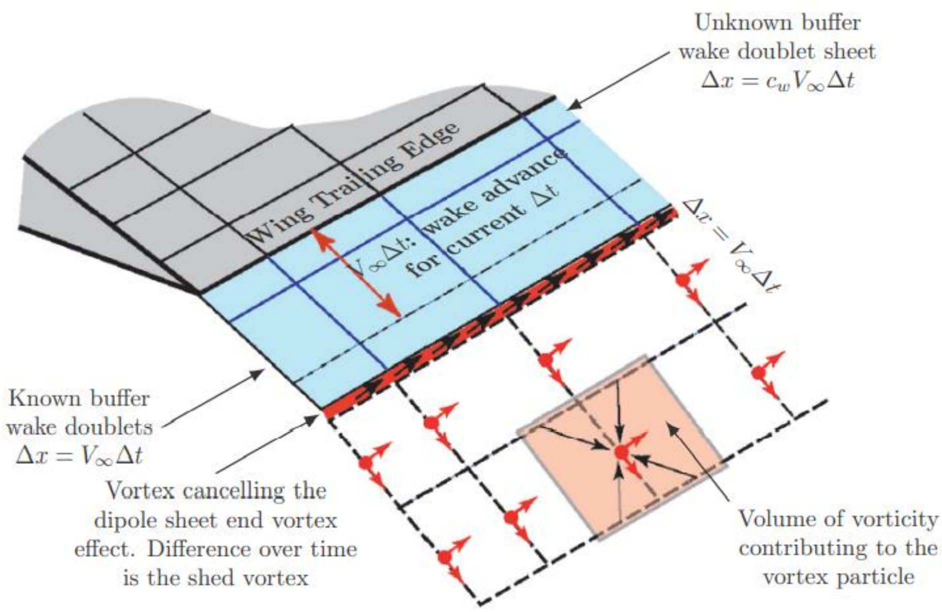

FIGURE 3. 14: Example of a vorton wake model (Willis' approach).

This task may be accomplished considering the doublet-vortex equivalence discussed in section 2.8 (Figure 2. 14): for the particular case of a constant doublet panel, this corresponds to a vortex ring around the perimeter, implying that the strength of the vortex line segment between two adjacent constant strength dipole panels is merely the difference in their strengths. Therefore, the vorton is computed by integrating the strength of the vortex line segments between adjacent panels.

It should be noticed that several strategies to convert a panel into a vorton element do exist: in this scenario the Willis' approach reported in Figure 3. 14 represents just an example, whereas, for instance, the one adopted by the solver PaMS employed in this work is characterised by the conversion into vortex particles localised at the four vertices of the transformed quadrilateral panel (Figure 3. 15).

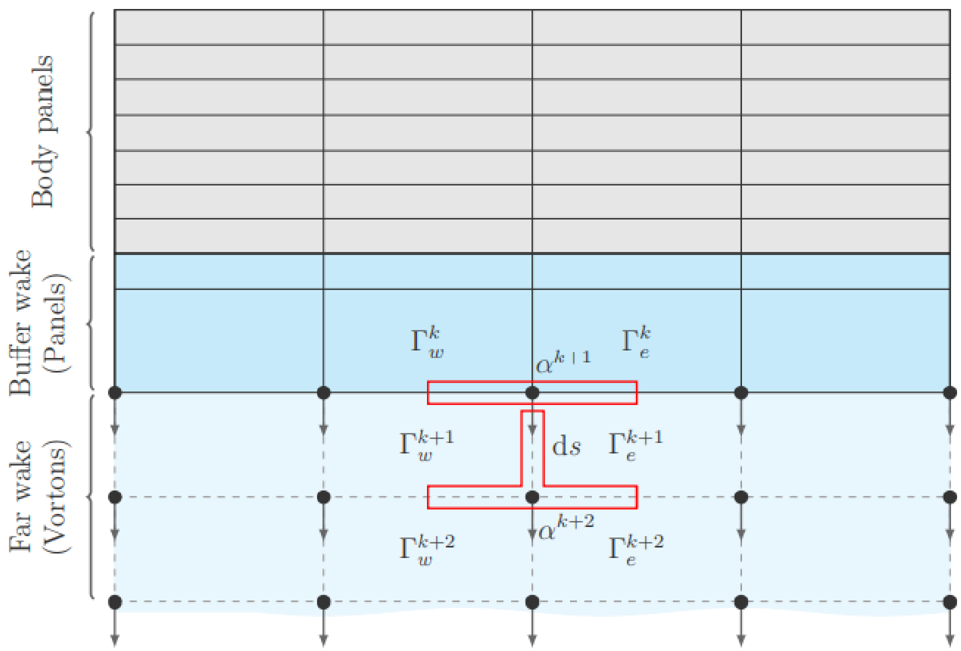

FIGURE 3. 15: DIAS[1] vorton wake model. The area enclosed by the red line represents the integration zone employed to compute the vorton strength.

[1] Department of Aerospace Engineering, University of Naples "Federico II".

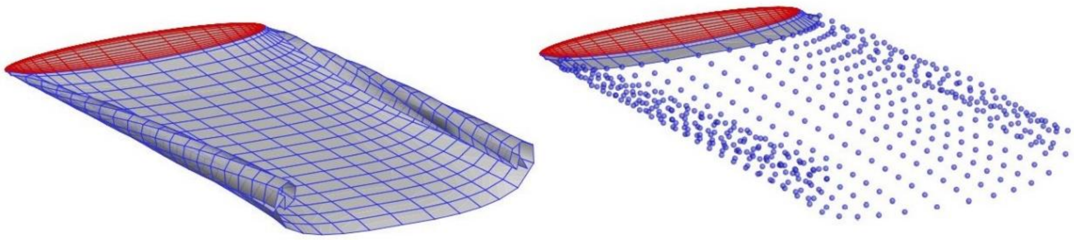

FIGURE 3. 16: Panel (on the left) vs vorton (on the right) wake.

3.4 PaMS Code

In order to give a complete understanding of the code employed for the simulations carried out in the present work of thesis, this final section is dedicated to a short description of PaMS (**Pa**nel **M**ethod **S**olver), developed by Dr. P. Caccavale and created to have a powerful, flexible and almost costless analysis tool whose scope encompasses a variety of aeronautical and naval unsteady calculations on generic geometries, within the applicability limitations of potential flows.

The main topics covered are a description of the main features, of the settings the solver requires and of the key variables involved in the wake modelling. The analysis of a test case for its validation is the goal of the last chapters.

3.4.1 Main Features

PaMS is an open source software written in *Fortran* programming language to solve potential flow fields by means of the panel method technique and suitable for 3D, unsteady, low-order, unstructured and multi-body applications. As all the other numerical analysis software, to be exploited in a design cycle, it has to show satisfactory reliability in the prediction of the phenomena under study, require affordable costs in terms of simulation time and computational resources, be as much user-friendly as possible and eventually be customisable with specific routines that can may be introduced. For the purpose of achieving these objectives, innovative features characterise the PaMS code and make it different from other similar panel solvers.

The first important peculiarity concerns operating on unstructured grids with both quadrilateral and triangular panels, resulting in a greater simplicity and rapidity in the approach without altering the result accuracy. Also the use of stereolithography models, a numerical representation of CAD[2] designs, is allowed, skipping over the geometry panelling step. Another option enables to treat possible interpenetrations between two or more bodies (for instance the wing-fuselage group of an airplane): they can be panelled separately and the meshes located as desired with no changes in the original CAD.

Another important feature is the computation of pressure loads at the very grid points, by means of direct derivation of the potential function and not by interpolation of the surrounding point values. This gives the possibility to couple the fluid dynamic solver to a solver for structural analyses through the same mesh.

Moreover, PaMS can deal with bodies whose geometry may change in time, so unsteady calculations regarding fluid-structure interactions can be performed, as aeroelastic problems (vibrations of wing/ailerons, deformation of a sail), if new routines are introduced on purpose or other commercial software for structural analyses are employed jointly.

The possibility to interface directly with the most common pre- and post-processors (*Gambit*, *Nastran*, *Hypermesh*, *Tecplot*) is another selling point to make the most of the code.

Also, PaMS is available both in a serial and in a – shared memory only – parallelised version (both of which exploit the dynamic memory allocation), so that the computational effort related to the composition of the equations system and to its solution can be distributed among different processing units hosted on a single machine.

Finally, the physical and mathematical core of PaMS is unveiled in Figure 3. 17, where the simplifying hypothesis and the consequent problem are pointed out.

[2] Computer-Aided Design.

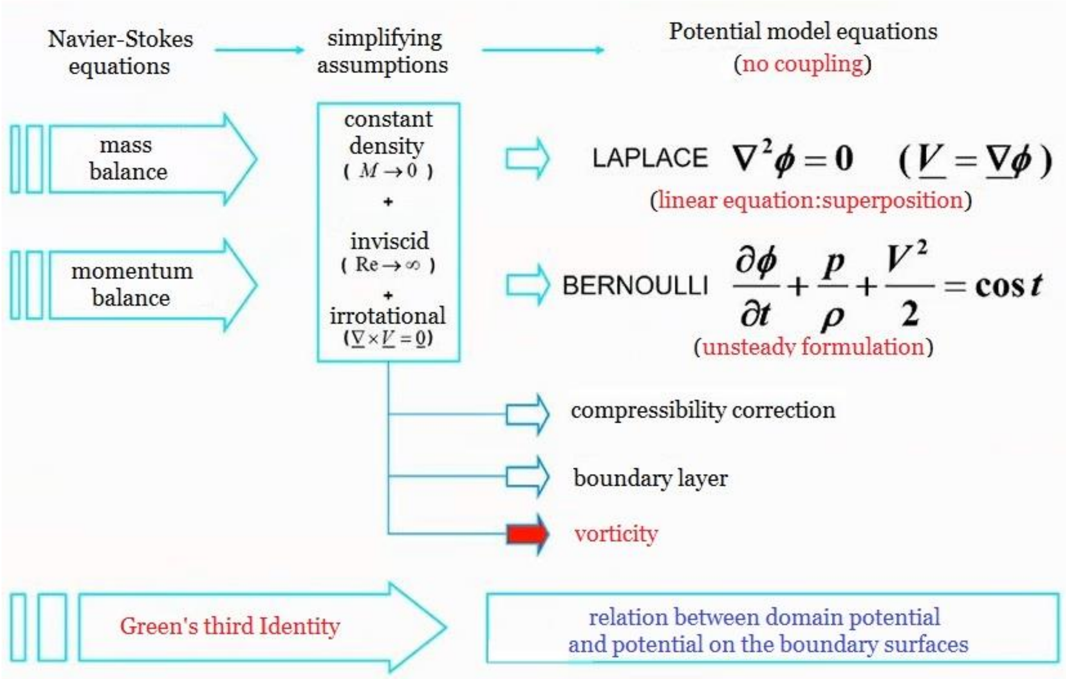

FIGURE 3. 17: PaMS governing equations.

3.4.2 Settings

The flow chart on which PaMS is based follows the numerical procedure already presented in Figure 3. 6: acquisition of all the information needed to set up the simulation and, within a cycle on the time-steps, BCs update, resolution of the linear system, processing and writing of the results.

For more thorough information, the reader is invited to consult the official website http://www.fluere.it/HTML/homepage.html .

Here, close attention is paid to the input phase. This latter consists of two main steps:

- read *DATAIN.dat* file
- read *.geo* file

The *DATAIN.dat* file is composed of *namelists* (an example is reported in Figure 3. 18) to set to specific numbers/text, globally arranged in two blocks: the *JobData* and the *GeoInfo*.

JobData

```
----------------------------------------------------------------------
&RUN       runname="PaMS-simulation"                    ver='BS'   &END
----------------------------------------------------------------------
&INFTY     velinf(1,1)=1.0     velinf(2,1)=0.0     velinf(3,1)=0.0     &END
&INFTY     omginf(1,1)=0.0     omginf(2,1)=0.0     omginf(3,1)=0.0     &END
&INFTY     density( 1)=2.0     stpress( 1)=0.0     soundsp( 1)=340.3 &END
----------------------------------------------------------------------
&TIME      dt=5.0              tstart=0.0          tend=60.0           &END
----------------------------------------------------------------------
&INVERTER omegainv=0.0         convinv=1.E-6       maxiter=100         &END
----------------------------------------------------------------------
&BODY      nbody =1            relmot='N'          symplane=0          &END
----------------------------------------------------------------------
```

GeoInfo

```
----------------------------------------------------------------------
&GEOIN     geoname="filename.geo"
&SCALE     sclfac(1)=1.0       sclfac(2)=1.0       sclfac(3)=1.0
&KWAKE     ang=140.
&KWAKE     nkwts=200           nkwtsrig=0          nkwtspan=200
&KWAKE     xanru = 0.          yanru = 0.          zanru = 0.
&BC        bctype(1)='D'       bctype(2)='R'       bctype(3)='I'
&BCLIM     corerad  =0.01      coremod  ='R'
----------------------------------------------------------------------
&GEOTRA    GT(1,1)=0.0         GT(1,2)=0.0         GT(1,3)=0.0         &END
&GEOTRA    GT(2,1)=0.0         GT(2,2)=0.0         GT(2,3)=0.0         &END
&GEOTRA    GT(3,1)=0.0         GT(3,2)=0.0         GT(3,3)=0.0         &END
&GEOROT    GR(1,1)=0.0         GR(1,2)=0.0         GR(1,3)=0.0         &END
&GEOROT    GR(2,1)=0.0         GR(2,2)=0.0         GR(2,3)=0.0         &END
&GEOROT    GR(3,1)=0.0         GR(3,2)=0.0         GR(3,3)=0.0         &END
&SYSTRA    ST(1,1)=0.0         ST(1,2)=0.0         ST(1,3)=0.0         &END
&SYSTRA    ST(2,1)=0.0         ST(2,2)=0.0         ST(2,3)=0.0         &END
&SYSTRA    ST(3,1)=0.0         ST(3,2)=0.0         ST(3,3)=0.0         &END
&SYSROT    SR(1,1)=0.0         SR(1,2)=12.0        SR(1,3)=0.0         &END
&SYSROT    SR(2,1)=0.0         SR(2,2)=0.0         SR(2,3)=0.0         &END
&SYSROT    SR(3,1)=0.0         SR(3,2)=0.0         SR(3,3)=0.0         &END
----------------------------------------------------------------------
```

FIGURE 3. 18: PaMS code: a summary example of *DATAIN.dat* file.

All the general information concerning the set-up and the simulation features belong to the *JobData* block:

- *runname*: name of the simulation
- far-field conditions in the inertial reference frame (X, Y, Z)
    - *velinf*: asymptotic velocity components
    - *omginf*: rotational speed components

thermodynamic properties

- *density*
- *static pressure*
- *sound speed*

- unsteady variable management
    - *dt*: time-step
    - *tstart*: start time
    - *tend*: finish time
- iterative method parameters: convergence check and solution speed up
    - *omegainv*: relaxation coefficient
    - *convinv*: convergence criterion
    - *maxiter*: maximum number of iterations
- geometry and motion-related features
    - *nbody*: number of bodies
    - *relmot*: presence or not of relative motion
    - *symplane*: symmetry planes in the inertial reference frame

There are as many *GeoInfo* blocks as many *nbody*. For each we find:

- *geoname*: this namelist recalls the *.geo* file with the mesh
- *sclfact*: scale factors in the body-fixed reference frame (x, y, z)
- setting of the wake
    - ang: reference angle to identify the TE
    - *nkwts*: maximum number of wake time-steps
    - *nkwtsrig*: number of rigid wake time-steps
    - *nkwtspan*: number of panel wake time-steps
- *xanru / yanru / zanru*: normal to the plane in the global reference frame where the wake self-induction is neglected
- *bctype*: type of BC
    - Dirichelet/Neumann
    - rigid/flexible
    - wake permeability/impermeability
- singularity core
    - *corerad*: core radius
    - *coremod*: core function model

- body position and motion
  - *GEOTRA & GEOROT*: kinematic parameters of the body in its local reference frame in terms of translational and rotational displacement, velocity and acceleration
  - *SYSTRA & SYSROT*: kinematic parameters of the local reference frame with respect to the global one, in terms of translational and rotational displacement, velocity and acceleration

The *.geo* file is arranged as reported in Figure 3. 19 and contains data regarding the body discretisation into panels. The coordinates of every grid point expressed in the body reference frame are listed in the *GRIDP* section. In the block underneath (PANEL) each line denotes a panel, identified by 4 (if quadrangular) or 3 (if triangular) indices that refer to its grid points. Obviously, the criterion the grid points are taken to define a panel has to be the same for all of them, so their normal vectors are characterised by a common orientation, that is to say that the edges shared by two adjacent panel should be travelled in two opposite directions.

```
GRIDP
-.5000000000000000E+00 0.0000000000000000E+00 0.0000000000000000E+00
0.0000000000000000E+00 -.5000000000000000E+00 0.1224606353800000E-15
0.0000000000000000E+00 0.5000000000000000E+00 -.6123031769100000E-16
...                    ...                    ...
...                    ...                    ...
PANEL
          1        70       115         7
         70        71       116       115
         71        72       117       116
        ...       ...       ...       ...
        ...       ...       ...       ...
          3       105       347
          3       347        34
         97         1       350
        ...       ...       ...
        ...       ...       ...
```

FIGURE 3. 19: PaMS code: an example of *.geo* file.

Having read the geometry file, an algorithm seeks for neighbouring panels (*i.e.* at least one edge in common) to speed up and simplify the calculations. This plays a role of fundamental importance because, as previously mentioned, the input mesh might be unstructured, that means it is not characterised by an order that would allow the identification of a panel, and therefore of its neighbors, simply through a pair of *ij* indices, as within a two-dimensional matrix.

Further on, those panels of which one edge is part of the trailing edge have to be spotted in order to superimpose the closure condition. As for thick bodies (where Dirichlet BCs apply), the angle between two normal vectors whose panels share one edge has to be greater than the namelist *ang* reported above.

Instead, for thin bodies (Neumann BCs hold), the edges where the wake sheds from, are chosen, among all the outer panels (*i.e* of which at least one edge is not shared), as those such that the angle between the undisturbed wind direction and the control-point/free-edge-mid-point is less then *ang*.

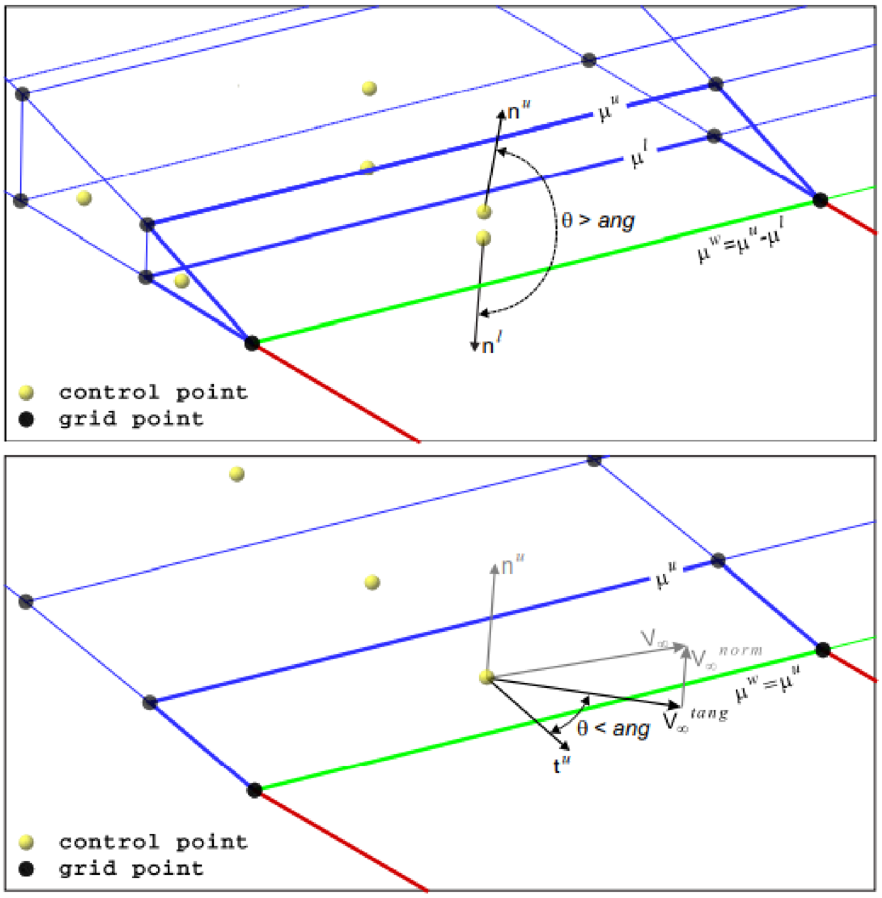

FIGURE 3. 20: PaMS code: search of TE panels.

3.4.3 Workflow: an example

Figure 3. 21 shows an example of PaMS workflow. The first thing we need is a digital model of the object of study that is going to be panelled. By means of specific commercial software (*Gambit*, *Hypermesh*, *Fluent*, *Nastran*, …), every surface will be meshed. In some cases, as said before, this step is skipped over and the analysis is performed based upon the stereolithography related to the body under consideration. The pre-processing phase is concluded once the discretised model has been translated into a file suitable to PaMS input. A dedicated routine named *Converter* has been written in this regard: it is capable of reading several mesh formats like *.neu* (*Gambit*), *.nas* (*Nastran*), *.stl* (*stereolithography*) and it gives as output a *.geo* file (Figure 3. 19).

Having a geometry-related file ready, the *DATAIN.dat* file has to be set up.

As for the results, the velocity and pressure fields can be viewed through the use of the most common post-processors (*Tecplot*, *Paraview*, *Patran*, …), while for solution time-history and the solution convergence, any software for two-dimensional graphics can be accessed.

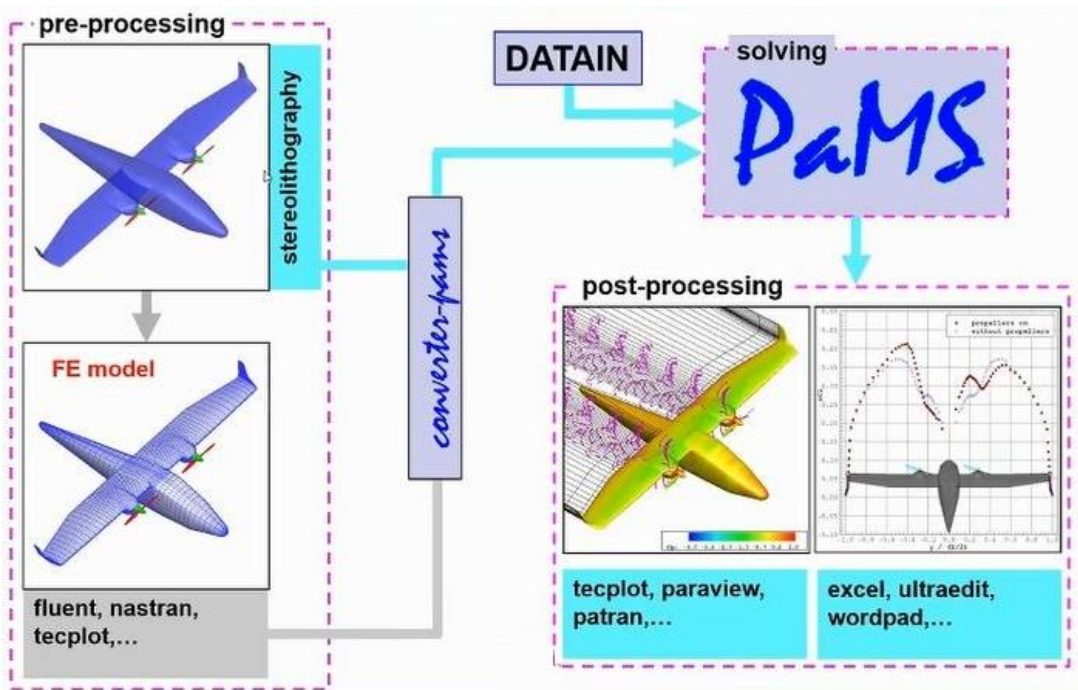

FIGURE 3. 21: PaMS code: workflow.

3.4.4 Wake modelling: key variables

By the occurrence of a wake present, to model it in an accurate way is of fundamental importance for a correct evaluation of the aerodynamic loads. In this paragraph, a quick recap concerning three key features involved in shaping a wake is reported:

- wake length
- wake D.o.F.[3]
- vortex core radius effect
- panel-to-vorton conversion position

Let us review these characteristics, by making some references to the variables already listed in section 3.4.2.

Wake length. This parameter is established beforehand by fixing (*nkwts*), the maximum number of time steps every computational element will last inside the domain for, that is equivalent to set the maximum number of elements used for modelling the entire field. It is straightforward that if *nkwts* is less than the total number of time steps defined for that specific simulation, the numerical wake is cut off and the computational elements neglected after *nkwts*.

On the one hand, the truncation of panels/vortons simplifies and lightens the simulation, due to a reduction in the computational element number; on the other hand, the correspondent loss of information may imply a decrease in the solution accuracy according to the particular analysis. For example, for a fixed wing in a uniform flow field, if the truncation of the wake takes place once a steady state condition has been reached, there is no significant variation in the final solution, as the elements disposed are those far away from the body whose influence on the fluid field is not much relevant. In the case of a hovering rotor, it has already been pointed out that being null the asymptotic flow, the velocities induced by the singularities play a primary role and their suppression determines a significant change in the shape of the wake. This effect will be evaluated on a validating test case and is reported further ahead (see Figure 5. 7).

[3] Degrees of Freedom

Wake D.o.F. As presented in section 3.2.1, according to the way a wake can develop, it is possible to differentiate between:

- *flexible wake*: this model of wake takes into account all the computational elements inside the domain: in fact it is necessary to evaluate the local velocity field – given by the superposition of the far-field flow and the effect of all sources and doublets – at each wake panel's grid point and/or control point and to deform these panels in order to fulfil equation 3. 18 correctly. The leading parameters to set are (*xanru, yanru, zanru*) = (0, 0, 0).

- *rigid wake*: the geometry of the wake is imposed *a priori*, so the evolution is only due to the asymptotic flow that makes the wake translate downstream and no deformation to the panels is introduced by the local flow field. Obviously, the descriptive ability is strongly limited given that there is no chance of characterise deformations a real wake shows (*e.g.* the roll-up effect) and interactions with other bodies. Also, this model is not suitable for a hovering rotor, and in general for all those cases where the asymptotic velocity is zero, because this makes the development of the wake impossible to determine. The number of wake rows to be set as rigid is chosen in *nkwtsrig.*

In Figure 3. 22 and Figure 3. 23 a comparison between a flexible and a rigid wake is depicted.

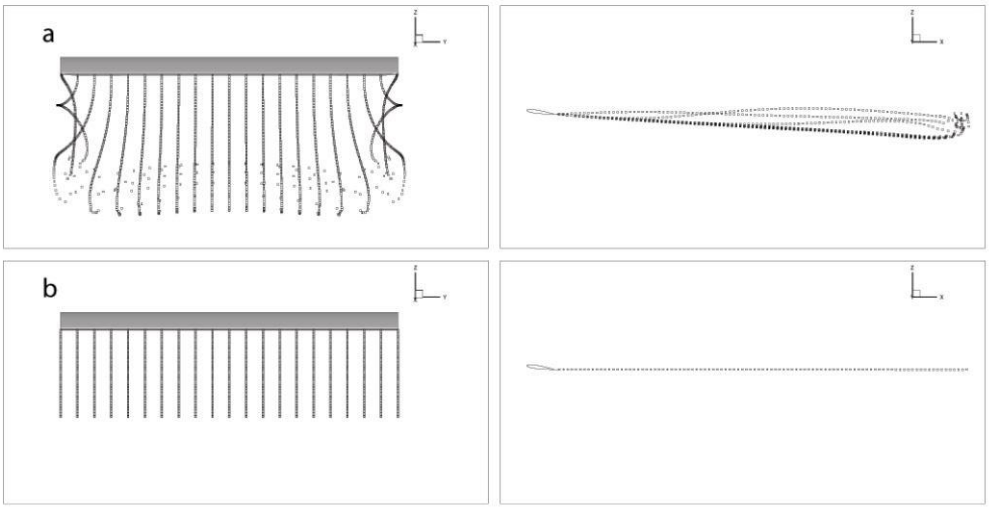

Figure 3. 22: Fixed wing: flexible (a) and rigid (b) wake models.

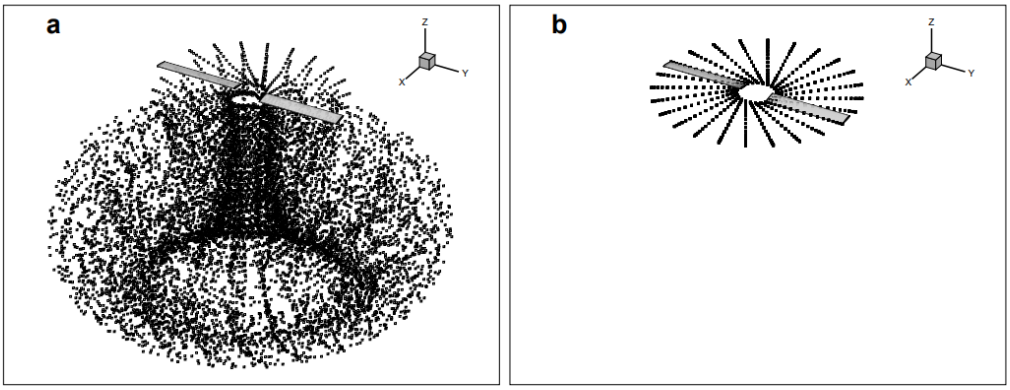

FIGURE 3. 23: Hovering rotor: flexible (a) and rigid (b) wake models.

- *1 D.o.F wake*: this model has been specifically developed for the aerodynamic analysis of fixed-point rotors/propellers as a combination of the two described above. Indeed the radial component of the velocity locally induced by each computational element is neglected and only the axial motion is possible, hence the name *one-degree-of-freedom wake*. Thus it behaves as if was flexible in the axial direction (along the rotor shaft) and rigid in the radial direction. In this case (*xanru*, *yanru*, *zanru*) = (0, 0, 1).

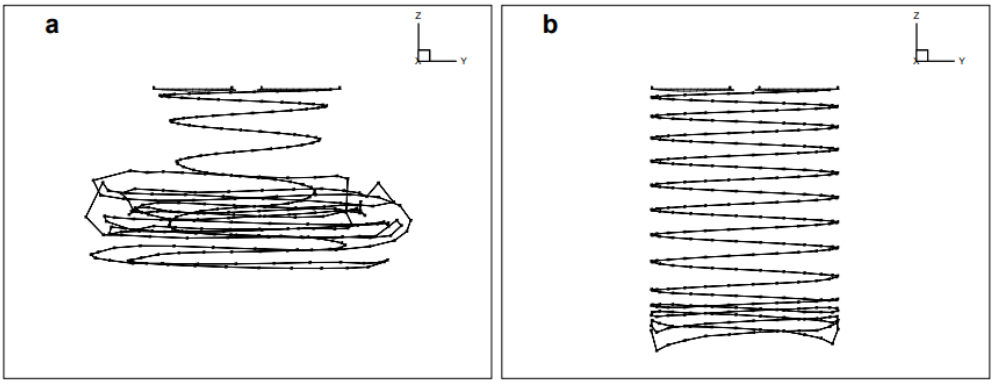

FIGURE 3. 24: Hovering rotor: flexible (a) and 1 D.o.F (b) wake models.

Vortex core radius effect. Both the vortex core radius (*corerad*) and the vortex core function (*coremod*) influence the shape and the evolution of a wake as they affects how far and in which way the core effect occurs.

Considering a Rankine[4] vortex model, for $r_\sigma < 1$ (*i.e.* $r < r_c$[5]), the induced velocity decays linearly with the distance (r) from the point where the singularity is located, whereas for $r > r_c$, the Biot-Savart law rules. Therefore the vortex core effect concerns all the points within a singularity-centred sphere of radius r_c. The greater r_c, the wider the area affected by the linear induction is; as a consequence a lower value of induced velocity is registered on the border of vortex core ($r = r_c$) and a lower average value all over. Comprehensively the wake appears to be less flexible and to the limit of very big r_c, the induced velocities in each point of the wake are small enough to lead towards the rigid wake model (Figure 3. 25). On the contrary, a reduction in r_c results in increasing averaged induction values on the vortex core edge and thus a more flexibility for the wake.

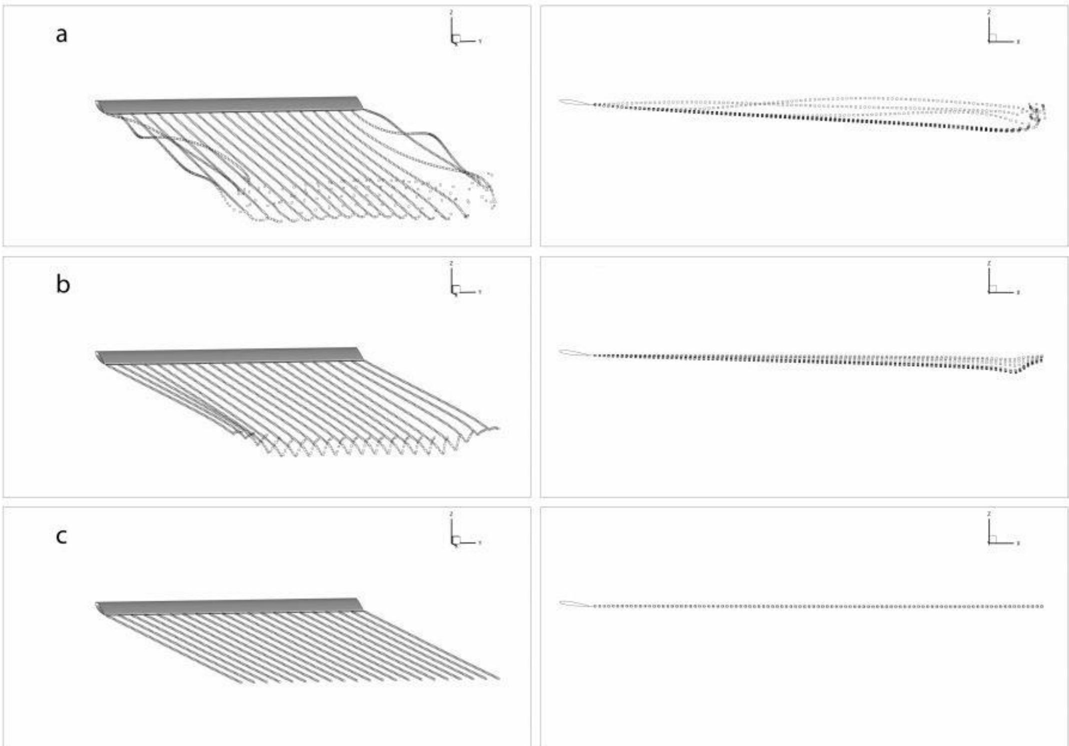

FIGURE 3. 25: Fixed wing, vortex core effect: $r_c/b = 0.01$ (a), $r_c/b = 0.1$ (b), $r_c/b = 1$ (c), where b is the wing span.

[4] Please refer to Figure 3. 12.
[5] Core radius.

A $r_{c,min}$ can be defined as the minimum distance between computational elements such that, if $r_c < r_{c,min}$, the shape and the evolution of the wake are not affected since every computational element is outside of the neighbouring element vortex cores and the Biot-Savart law is the only that counts for the inductions (*i.e.* the vortex core function is not involved).

In hovering, the vortex core radius and model as well are crucial. In Figure 3. 26, it can be observed that for small core radii, the wake may be highly flexible, up to the point that, nearby the root, the fluid is flowing upwards (*fountain effect*); rather, if r_c is significant, the wake stiffening brings to an incorrect evaluation.

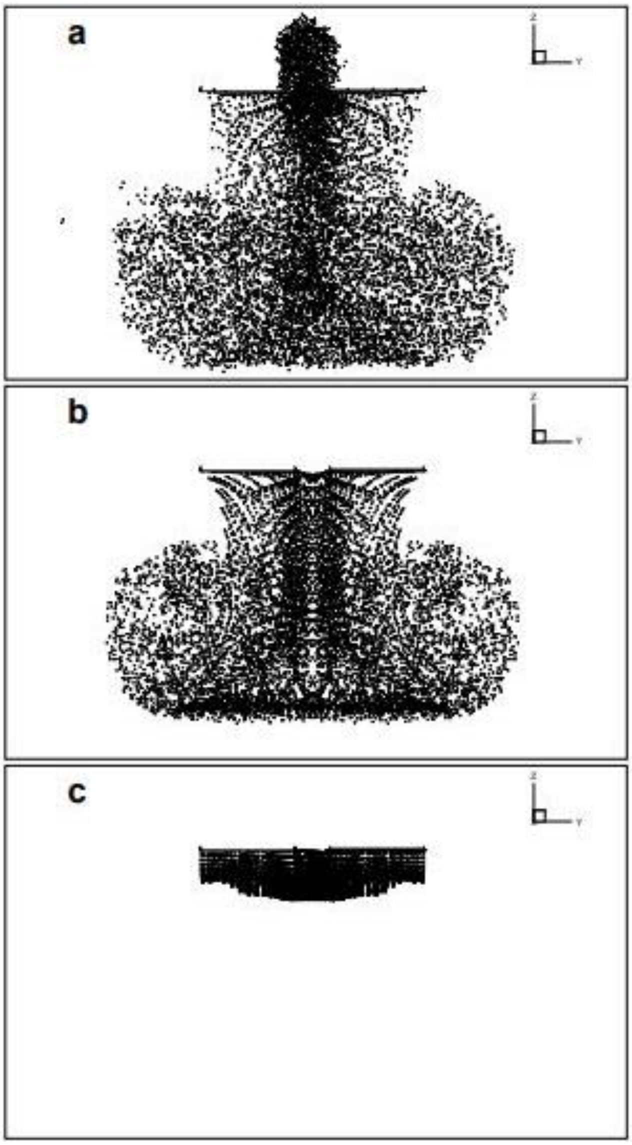

FIGURE 3. 26: Hovering rotor, vortex core effect: $r_c/D = 0.01$ (a), $r_c/D = 0.1$ (b), $r_c/D = 1$ (c), where D is the rotor diameter.

Panel-to-vorton conversion position. As previously stated (paragraph 3.3.2), the part of the wake closer to the TE, the so called near wake – whose extension depends on the time step size (*dt*), is modelled through panels and according to the procedure explained, a minimum of two wake panel rows is required.

In the case of a hovering rotor, the abrupt start and the intense starting vortex may be the cause of instabilities in the numerical wake, so that, keeping in mind the different local flow field induced by vortons, a near wake with more than two panel rows could be preferred. The limits of applicability of this choice coincide with those of the classical panel methods, and therefore no wake-wake nor wake-body interaction has to be expected. Furthermore, it is not advisable to further increase the extension of the panel-modelled wake portion because not only would it reduce the advantage offered by the vorton wake, but the user would risk losing the accuracy of the solution due to an excessive deformation of the panels with a consequent possible divergence of the solution.

Following this remark, a trade-off is found out for the simulations carried out and presented in Chapter 5 that apply to a near wake with as many panel rows as needed to cover the distance between the blade itself and the one that follows during the first revolution.

CHAPTER 4

PROPELLERS: MAIN THEORIES

4.1 Generalities and Definitions

Since this thesis concerns the study of complex rotating objects as propellers with variable rotation axis, in order to provide to the reader with all the instruments needed to achieve a full understanding of the subjects here dealt, it is dutiful to briefly introduce both the definitions and the theories a rotary wing analysis is based on. This is the purpose of the current chapter that is the last one providing theoretical information. However, the contents here reported are far from being thorough, so that for complete argumentations please refer to the authors recommended in the bibliography section.

Slicing a generic propeller blade of radius R at a distance $r_h < r < R$ from its hub (whose radius has been denoted with the symbol r_h) by means of a plane orthogonal to the propeller plane of rotation, one gets a wing section whose chord $c(r)$ forms an angle $\theta(r)$ called either *blade pitch angle* with the plane of rotation itself. As it can be observed in Figure 4.1, the relative motion between this blade element and the surrounding flow is given by a velocity vector $\Omega r = 2\pi n r$ which is due to the revolution of the propeller about its axis (and hence lays in the plane of rotation) and by a vector V_∞ which, on the other hand, is related to the forward translation of the rotor along its symmetry axis. Therefore the effective velocity V_e can be written as

$$V_e = \sqrt{(\Omega r)^2 + V_\infty^2} \tag{4.1}$$

The vector $\underline{V_e}$ forms an angle ϕ, called the *inflow angle*, with $\underline{\boldsymbol{\Omega}} \times \underline{r}$ (*i.e.* with the plane of rotation), whereas, the angle of incidence

$$\alpha = \theta - \phi = \theta - arctan\frac{V_\infty}{2\pi nr} = \theta - arctan\left(J\frac{D}{2\pi r}\right) \qquad 4.\ 2$$

is comprised between $\underline{V_e}$ and the airfoil zero lift line (*z.l.*). In equation 4. 2, $D = 2R$ is the propeller diameter and the dimensionless quantity $J = \frac{V_\infty}{nD}$, called *advance ratio,* refers to the distance covered by the propeller in one revolution.

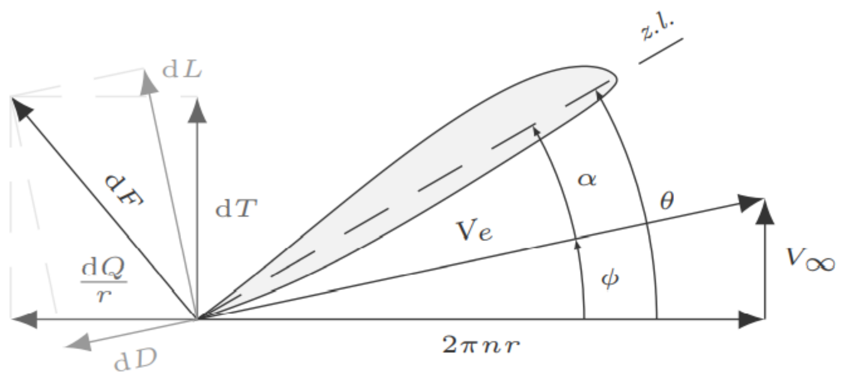

FIGURE 4. 1: References for a blade element.

The airflow at the blade section produces elementary lift and drag forces, $\underline{dL}$ and $\underline{dD}$, which, by definition, are normal to and parallel to the resultant velocity $\underline{V_e}$, respectively. Similarly, if the elementary aerodynamic force $\underline{dF} = \underline{dL} + \underline{dD}$ acting on the wing section is decomposed into its components parallel to and normal to the rotation plane, the elementary

$$dT = dL\cos\phi - dD\sin\phi \qquad \textit{thrust} \qquad 4.\ 3$$

$$\frac{dQ}{r} = dL\sin\phi + dD\cos\phi \qquad \textit{torque over r} \qquad 4.\ 4$$

are found out. Finally, denoting by *N* the number of blades, the overall forces acting on the propeller can be evaluated as *N* times the integral of these differential quantities over the working span of the blade, *i.e.*

$$T = N \int_{r_h}^{R} \frac{dT}{dr} dr \qquad 4.5$$

$$\frac{Q}{r} = N \int_{r_h}^{R} \frac{1}{r} \frac{dQ}{dr} dr \qquad 4.6$$

As every aerodynamic force, the thrust T can be expressed through:

- a dynamic pressure, proportional to $\rho n^2 D^2$)
- a reference surface, related to D^2
- a dimensionless coefficient which depends on the angle of attack (and hence, through equation 4. 2, on the advance ratio J) and on both the Reynolds and Mach numbers.

Therefore, one could formally write:

$$T = C_T \rho n^2 D^4 \qquad 4.7$$

And in a similar fashion, for the torque Q and the power P:

$$Q = C_Q \rho n^2 D^5 \qquad 4.8$$

$$P = C_P \rho n^3 D^5 \qquad 4.9$$

On the basis of these definitions, the propeller efficiency η can be introduced. This quantity is the ratio of the useful power output $V_\infty T$ and the one supplied to the propeller $P = \Omega Q$, *i.e.*

$$\eta = \frac{V_\infty T}{\Omega Q} = \frac{C_T}{C_P} J \qquad 4.10$$

All the dimensionless coefficients here defined depend on the advance ratio J, and their typical behaviour is shown in Figure 4. 2. As J increases, the angles of attack of each blade element decrease. Since the most of the thrust T is given by the sectional lift acting on the propeller airfoils and due to the fact that far away from the stalled regions the lift coefficient C_l is a linear function of α, the thrust coefficient C_T as well is a nearly linear increasing function of α and thus a decreasing function of J. Similarly, as the advance ratio increases, the coefficients C_P and C_Q decrease with a nearly quadratic law since they mostly depend on the sectional drag force and, for a wing section, $C_d \propto \alpha^2$.

As it can be seen in Figure 4. 1, the single blade element produces a positive elementary thrust <u>*dT*</u> when the aerodynamic force <u>*dF*</u> points toward the propeller forward direction. Instead, when <u>*dF*</u> lays on the plane of rotation, the elementary thrust is equal to zero. For greater values of the advance ratio the component <u>*dT*</u> becomes negative, acting as a braking force. It should be noted that this dissertation holds for a single blade element only, even though a similar reasoning can be extended considering the integral values of the aerodynamic force <u>*F*</u>.

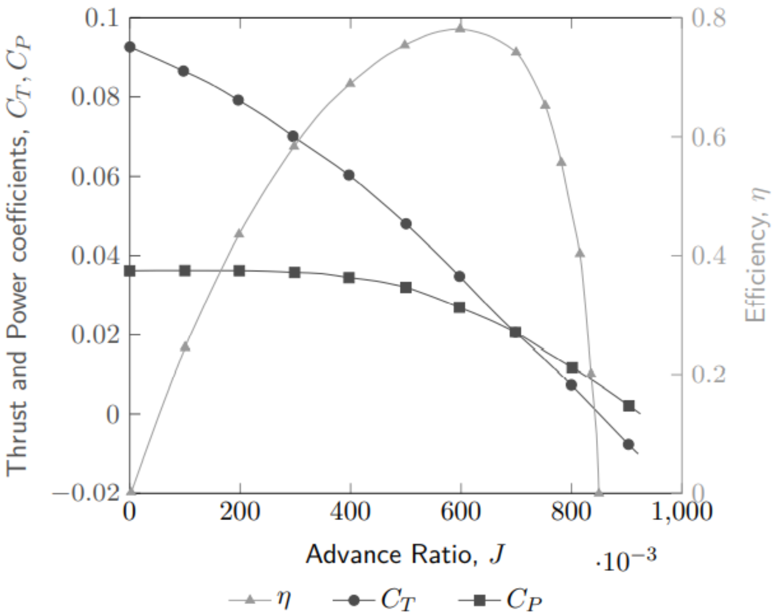

FIGURE 4. 2: Propeller characteristic curves.

4.2 Main Theories

Historically the isolated propeller (*i.e.* the propeller detached from its carrier body, *e.g.* an airplane) has been analysed by means of two different viewpoints: the *Momentum Theory* and the *Blade Element Momentum Theory* (BEMT).

4.2.1 Momentum Theory

The Momentum Theory, also known as *propeller-slipstream theory*, was firstly developed by Rankine (1865) and then extended by R. E. Froude (1889) and adopts a macroscopic point of view to model the behaviour of a column of fluid passing through a propeller. It considers the momentum and the energy of the fluid front of and behind the propeller, applying the basic conservation laws of fluid mechanics to the rotor and fluid as a whole in order to estimate the rotor performance. In fact, the basic idea is that, according to the Newton's third law, since the fluid exerts a force on the rotor disk, this provides a thrust (*i.e.* an equal and opposite reaction on the air). Being the energy level of the fluid flow at the back of the rotor different from the flow external to the wake, a contact discontinuity arises. This variation in the energy level constitutes the induced power loss of a rotary wing and corresponds to the induced drag of a fixed wing.

In the Momentum Theory the propeller is modelled as an actuator disk: a zero-thickness circular surface located in the rotor plane, where a pressure jump is generated across (Figure 4. 3).

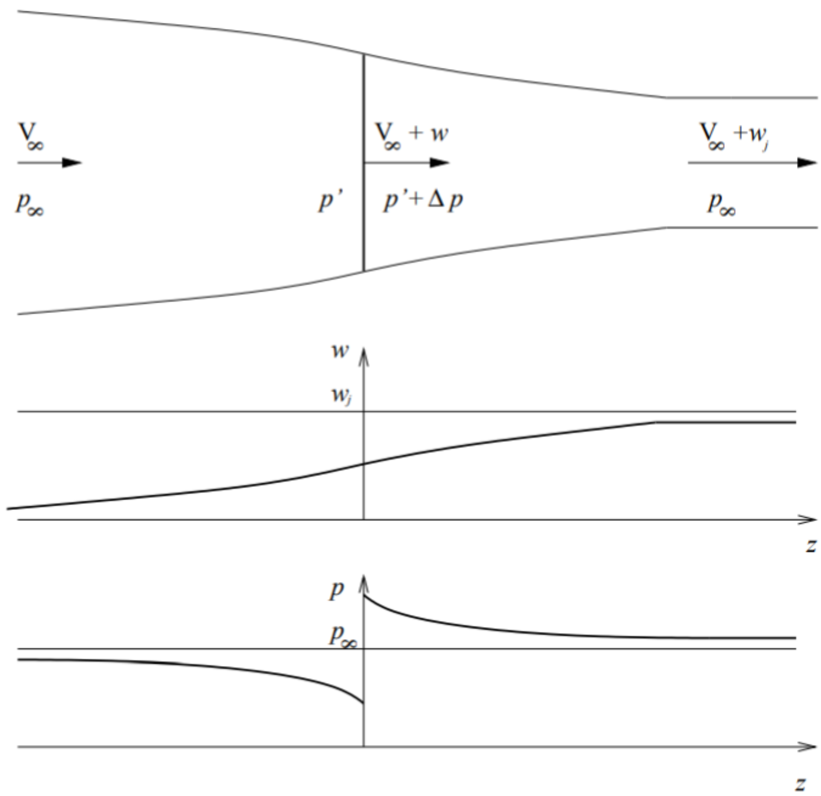

FIGURE 4. 3: Actuator disk model for the simple momentum theory.

In the most general formulation, not only the disk exerts a thrust, but also a torque, which imparts an angular momentum to the fluid.

However, even though the actuator disk is intended to simulate a propeller, strong differences between this model and a real rotor occur. For instance, the disk model corresponds to an infinite number of blades. As a consequence, the induced power loss predicted by the theory is lower since it does not take into account the non-uniform unsteady induced velocity due to a finite number of blades. Therefore this theory is mainly employed to obtain a first estimation of the wake-induced flow.

4.2.2 Blade Element Momentum Theory

A second point of view to describe a propeller performance results from the combination of two theories: the Blade Element Theory (already introduced in paragraph 4.1) and the Momentum Theory. The BEMT, unlike the Rankine's one, does take into account the propeller blade geometry.

It can be observed that the Blade Element Theory can be considered as an application of Prandtl's lifting-line to a rotary wing. In fact, as it has been implicitly alleged in section 4.1, each blade element is a two-dimensional airfoil that produces an aerodynamic force, but the wake vortices are trailed in helical paths rather than straight back as for fixed wings. In the BEM theory, the loading is computed using the two independent methods, by combining a local blade-element consideration, using tabulated two-dimensional airfoil data, with the one-dimensional momentum theorem. So by comparing Figure 4. 1 to Figure 4. 4, it should be noted that the free stream velocity and the tangential speed have been corrected with the motion imparted by the propeller, as predicted by the *slipstream theory* – in its general formulation due to Betz (1919) in order to consider also the rotational loss.

An overall Blade Element Momentum Theory sketch is reported in Figure 4. 4, where the axial and the tangential induced velocities are denoted by $V_\infty a$ and $\Omega r a'$, respectively. Given that both these quantities are positive, a comparison with the results of Figure 4. 1 suggests that, if J is the same, the inflow angle ϕ is greater in the BEMT than in the original Blade Element Theory.

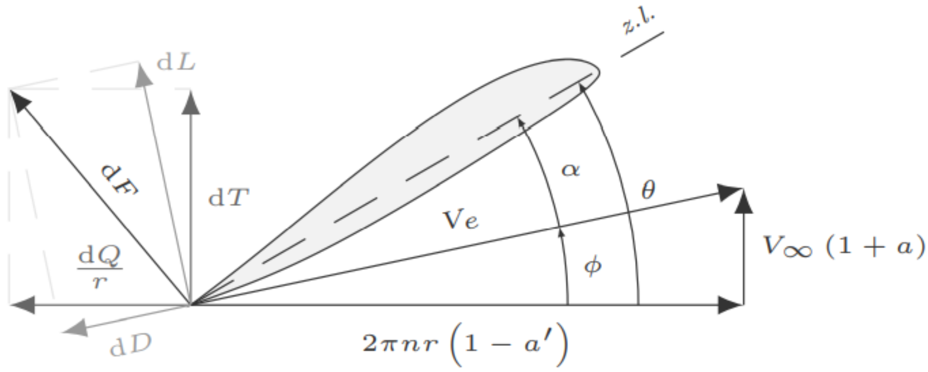

FIGURE 4. 4: References for the BEMT.

The fact that the BEMT takes into account the blade geometry makes it suitable not only for a detailed analysis of the performances of a particular propeller, but also to design a rotor targeting either the wanted thrust or a particular value of the available power. In both cases, this process requires in input some basic parameters, such as: the rotor diameter D, the number of blades N, the hub radius r_h, the number of revolution in the time unit n, the free stream velocity V_∞, the operational altitude H and the spanwise airfoil distribution.

CHAPTER 5

AN ISOLATED PROPROTOR PERFORMANCE

Having laid the theoretical foundations for a complete understanding of the treatment of the aerodynamic problem object of this thesis, the results of some VPM-based analyses carried out through the solver PaMS are reported in the present chapter. After a general overview regarding the experimental test case, *i.e*. the Bell-Boeing V-22 Osprey tiltrotor, with particular focus on its proprotors, there are going to be described in detail all the steps that led to the study of an isolated proprotor model, on purpose conceived, when performing a hovering flight followed by the complex unsteady kinematic phase of conversion from the helicopter mode to the airplane one.

5.1 V-22 Osprey Technical Specifications

The V-22 Osprey is a multiservice, multimission tiltrotor aircraft suitable for military missions and commercial roles. Capable of V/STOL, with forward flight like a conventional fixed-wing aircraft, it can perform such missions as troop/cargo transport, amphibious assault, search and rescue. The operational constraints and unique service requirements imposed a significant challenge to the aerodynamic development of the aircraft. Besides that, the program’s total cost to develop and produce 458 units was (under-) estimated to be about $48 billion, which translates into $105 million per Osprey, excluded research-development cost.

The unconventional design consists of two contrarotating proprotors, with three high-twist tapered blades, mounted at the wingtips that tilt, together with the engines and transmission nacelles, through 97° 30’ between tail-down hover and forward flight. The minimum time to accomplish a full conversion (0-90°) is 12 seconds. The rotors, powered by two *Rolls-Royce* T406-AD-400 engines, are synchronised by means of an interconnect shaft that runs through the wing. This shaft also provides power transmission from one rotor system to the other in the event of engine failure. Auxiliary drives from a centre wing gearbox provide power for hydraulics, oil cooler and electrical generators. The fuselage has been optimised for transport, featuring an upswept rear with loading ramp and two twin fins of moderate sweepback. The high-mounted, constant-chord wing is slightly swept forward, while the horizontal tailplane is unswept.

The aircraft folds compactly for stowage aboard ship: the entire procedure that involves folding blades parallel to the wing leading-edge, tilting the engine nacelles down to horizontal and rotating the whole wing/nacelle/proprotor group clockwise to lie over the fuselage, takes about 90 seconds.

The V-22 uses an advanced digital fly-by-wire control system. In hover, pitch control is provided by longitudinal cyclic pitch of both rotors. Yaw control is obtained with differential longitudinal cyclic and roll control is obtained by differential collective pitch in each rotor. The aircraft is able to maintain a relatively level roll attitude in sideward flight by programming lateral cyclic pitch in the same direction on both rotors in addition to differential collective pitch. In the airplane mode, the V-22 is controlled using conventional aerodynamic surfaces – flaperons for roll control, elevators and rudders on the empennage for pitch. In the transition mode the helicopter and airplane controls are phased for optimum control response.

About 43% of the airframe is made of graphite-epoxy composite materials and a hybrid structure (mainly aluminium frames and composites skins) has been created for the fuselage to reduce cost and weight and simultaneously improve quality.

The V-22 has crashworthy seating for 24 combat troops, two external cargo hooks for carriage of outsized equipment, a rescue hoist, and a cargo winch and pulley system for loading and unloading heavy internal cargo loads through the aft loading ramp which also permits quick egress and exit of troops.

The Osprey is capable of all-weather instrument flight, day or night, and continuous operation in moderate icing conditions at weights up to 27500 kg for self-deployment.

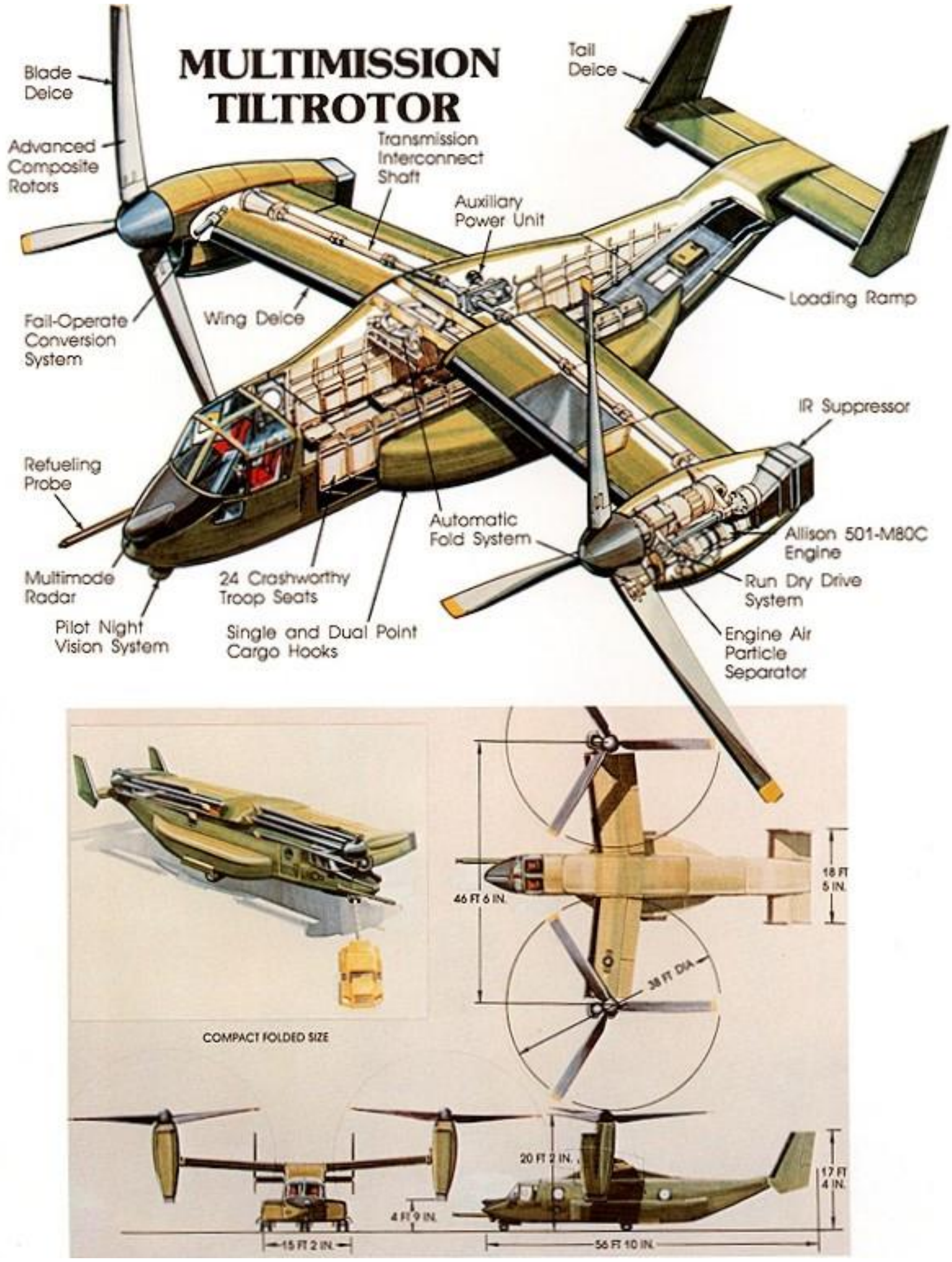

FIGURE 5. 1: V-22's salient design features and dimensions.

The main technical specifications concerning this tiltrotor aircraft are gathered in the following table.

DIMENSIONS				
EXTERNAL		TABULATED DATA		
Length: fuselage, excl probe	17.47 m	Wing: Airfoil section		Bell A821201
stowed	19.20 m	Chord, constant		2.54 m
Height: overall, nacelles vertical	5.56 m	Span, excl nacelles		14.02 m
stowed	6.73 m	Aspect ratio		5.5
Width: rotors turning	25.76 m	Area, total		35.49 m^2
stowed	5.61 m	Twist		0°
Nacelle ground clearance, nacelle vertical	1.32 m	Dihedral		3.5°
		Sweep		– 6°
Proprotor ground clearance, nacelle vertical	6.35 m	Incidence		0°
INTERNAL		Tail:	Horizontal	Vertical
Cabin: Length	7.37 m	Chord	2.28 m	2.08 m
Width	1.80 m	Span	5.61 m	3.40 m
Height	1.83 m	Aspect ratio	2.36	1.89
Usable volume	24.3 m^3	Area	8.22 m^2	12.25 m^2
		Incidence	– 3°	0°

WEIGHTS AND LOADINGS (USMC[1] Configuration)			
Empty weight	15032 kg	Max fuel weight	3493 kg
Design weight	17917 kg	Max internal payload	9072 kg
Combat weight	19374 kg	Cargo hook capacity, single	4536 kg
Self-deployment weight, STO	27500 kg	Rescue hoist capacity	272 kg
Max Take-off weight, VTO	21546 kg	Max disk loading, VTO	111.3 kg/m^2
STO	24948 kg	STO	130.2 kg/m^2

PERFORMANCE	
Max level speed at SL	509 km/h
Max cruising speed at SL, helicopter mode	185 km/h
Max rate of climb at S/L, vertical	332 m/min
inclined	707 m/min
Service ceiling	7925 m
Service ceiling, OEI[2]	3441 m
Hovering ceiling, OGE[3]	4331 m
T-O run at normal mission STO weight	less than 152 m
Range: amphibious assault	953 km
VTO with 4536 kg payload	648+ km
STO with 4536 kg payload	950+ km
g limits	+4/–1

TABLE 5. 1: V-22 Osprey technical specification.

[1] U. S. Marine Corps.
[2] One Engine Inoperative.
[3] Out of Ground Effect.

With regard to the rotor system, a summary of its characteristics is reported as it follows.

Number of blades	3
Rotor diameter	11.58 m
Blade chord, root	0.87 m
tip	0.56 m
Rotor disk area	105.36 m^2
Rotor blade area, each	4.05 m^2
Thrust-weighted solidity	0.110
Blade twist	– 47.5° (non-linear)
Blade airfoils	XN-28 *(r/R=0.2)*, XN-18 *(r/R=0.5)*, XN-12 *(r/R=0.75)*, XN-09 *(tip)*
Design tip speed, hover	240 m/s
cruise	200 m/s
RPM, minimum	316
normal	333 to 397
maximum	417

TABLE 5. 2: V-22 rotor system characteristics.

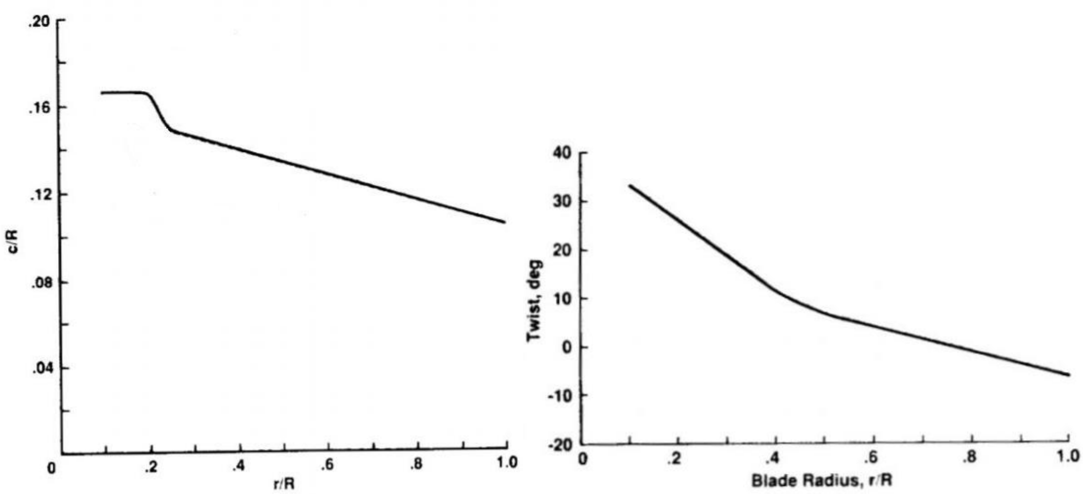

FIGURE 5. 2: V-22's rotor blade chord distribution (on the left) and twist distribution (on the right). Lengths non-dimensionalised to the rotor radius. [Original image is of poor quality].

5.2 Proprotor CAD Model

As previously highlighted, panel methods and vorton methods are appropriate for nearby flow field analyses. So that the body under examination – *i.e.* its shape – plays a crucial role in the setup, totally altering the results on equal input terms, in contrast to the BEMTheory where the geometrical peculiarities of the object are neglected and the rotor radius is the only parameter that counts.

The current simulation concerns a mock-up of the Osprey's isolated proprotor that has been created on purpose. Due to computational cost reasons, only the three blades have been modelled, while the hub and the nacelle have not been taken into account. The proprotor CAD model has been created using CATIA *Wireframe & Surface Design*, considering the technical specifications listed in Table 5. 2 and Figure 5. 2. Having no free database available about the XN-series airfoils, the NACA 64 series, already considered for the XV-15's rotor and for the one of the V-22 before optimisation, has been chosen as blade section. The digital mock-up is shown in Figure 5. 3, while the only blade is represented in Figure 5. 4 in order to appreciate the high twist angle.

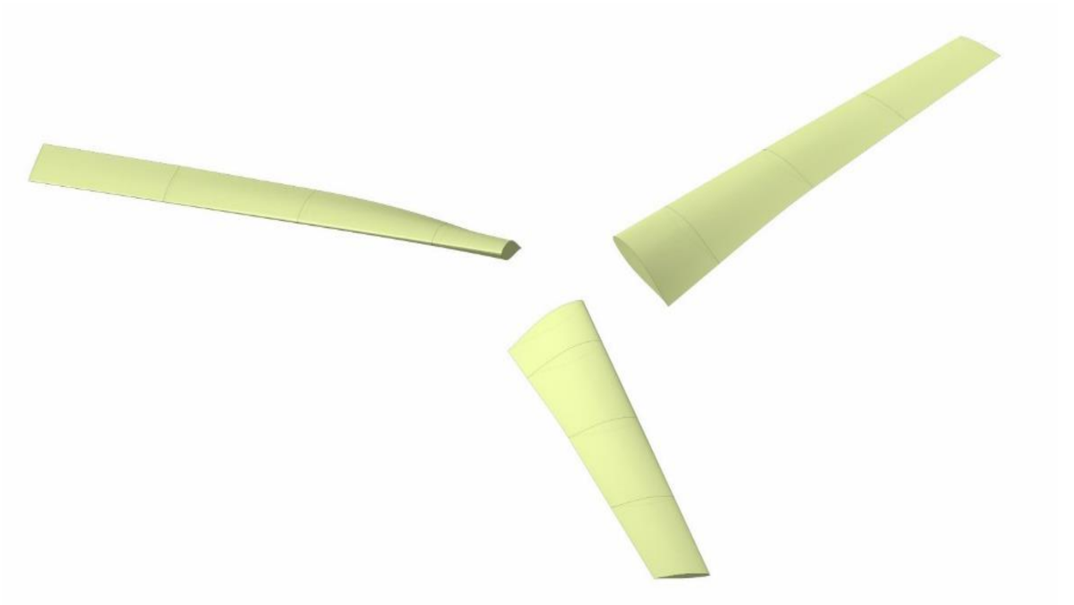

FIGURE 5. 3: Isometric view of the CAD target proprotor [CATIA Wireframe & Surface Design].

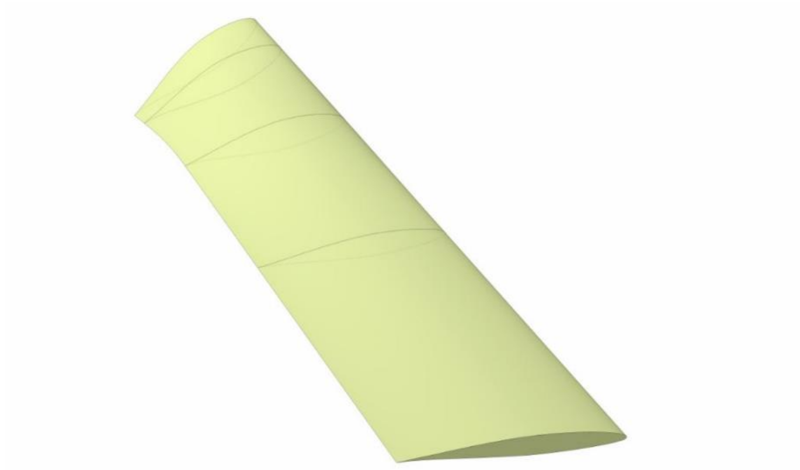

Figure 5. 4: CAD proprotor blade [CATIA Wireframe & Surface Design].

5.3 Geometry discretisation

As outlined in section 3.4.2, the first step aimed at the aerodynamic study of the potential flow-field surrounding a body by means of the VPM concerns the discretisation of its geometry into panels. The meshing strategy is dictated by the fact that the computational cost and the time complexity depend on the overall number of panels the domain has been divided into and the number of time steps the simulation requires. The latter is imposed by both the angular speed of the propeller (which rules the time resolution, and hence the time step amplitude) and the tilting phase duration (which is a design parameter).

Although the conversion takes 12 seconds by the *Osprey* flight manual, in the current work a 4-second tilt has been simulated not to overwhelm the computing machine whose main specifications are listed in Computer Hardware Specifications. Employing a revolution speed among the indicated normal operating range (see Table 5. 1), a time increment about 0.009 seconds long would suffice, amounting to 270 time steps for the simulation of the rotor in hover and 445 time steps for the transition to the airplane mode. Concurrently, the total number of panels has been limited as much as possible, leading to 1091 panels for the three blades – and here comes the compromise between nodes and time intervals.

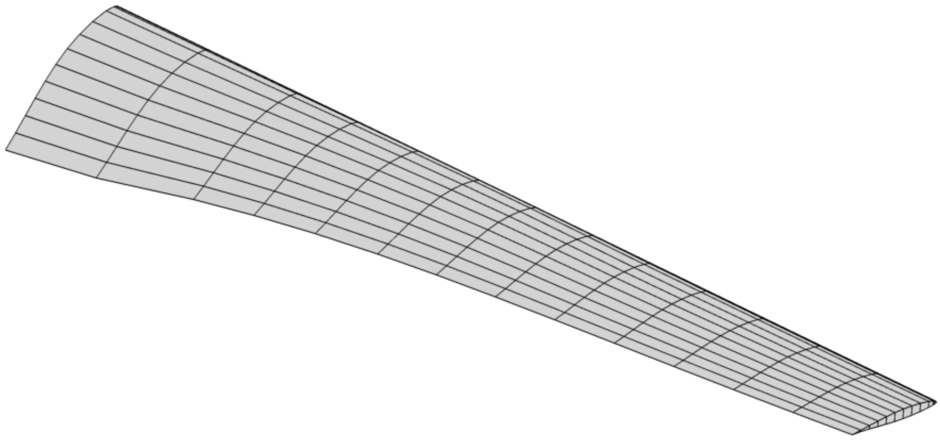

FIGURE 5. 5: Single blade mesh, spanwise panel distribution [MSC Software Patran].

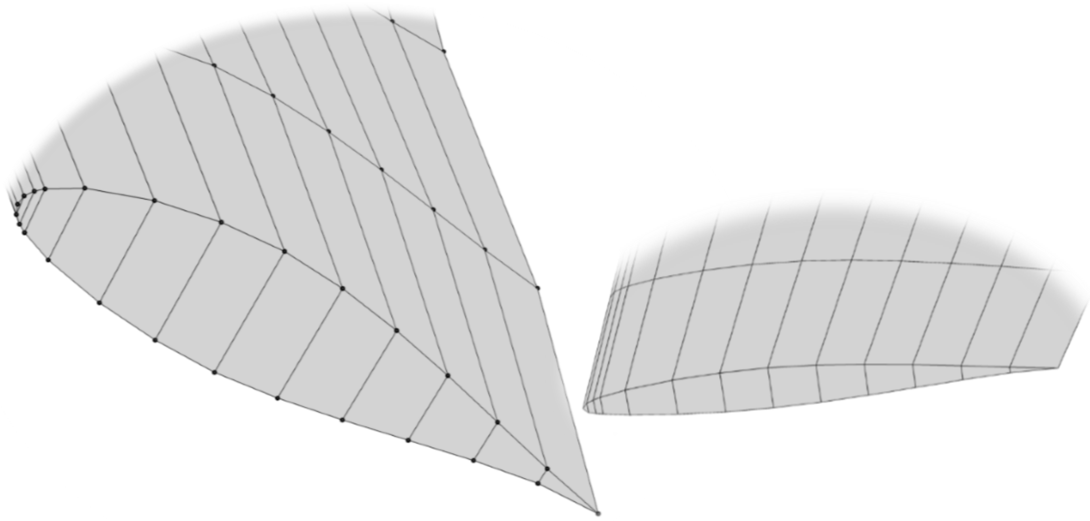

Root section **Tip section**

FIGURE 5. 6: Single blade mesh, streamwise panel distribution: detail view of the root section with highlighted mesh seeds (on the left) and the tip section (on the right) [MSC Software Patran].

Meshing the proprotor blade has represented a considerable challenge due to a high difference in the airfoil thickness along the wingspan. This factor, besides an elevated twist variation, has led to an unsought but unavoidable discretisation dissimilarity between the root and the tip section that has been minimised since, in some cases, it may cause numerical issues in the computation of the inductions. Moreover, the blade taper ratio, although moderate, has emphasized the panels being narrower with a greater aspect ratio the closer they were to the tip. The adopted solution to this issue is depicted in Figure 5. 5 and 5. 6, where the employed chordwise node distribution is highlighted by means of some big marks. As can be observed, the node density is higher in the fore part of the blade (*i.e*. near its LE[4], where the maximum curvature of the airfoil shape is present) up to the 10% of its chord, after which the seed distribution becomes uniform and no tightening is provided to the TE. As for the spanwise discretisation, additional mesh seeds have been arranged toward the blade tip to detect more precise information where higher velocities are obviously expected.

5.4 Computational Analysis of an Isolated Proprotor in Helicopter Mode

One has made use of the geometry and the mesh described lately to carry out a VPM-based analysis concerning the isolated proprotor. Particularly, the study here conducted is aimed to the investigation of the object when in helicopter mode during hovering flight, while the simulation concerning the transition mode will be presented in the paragraph that follows.

In the specific case of a hovering proprotor, a characteristic feature of the wake is the presence of an intense vortex at the blade tip which propagates downstream with a helicoidal trajectory in the first revolutions and then this trend is lost with the age of the wake due to self-induced deformations. According to Helmholtz' theorem, a system of free vortices is released from the blade trailing edges, whose intensity is equal to the variation in circulation along the blade span of the adherent vortices that correspond, as per Kutta-Zhukowsky's theorem, to a spanwise lift distribution. This latter reaches a peak around 85% of the radius, and then it becomes zero at the tip section, so that the tip vortex strength is much like the level of total circulation on the blade and the typical roll-up can be observed. Another main aspect of this flow field is the existence of a strong interdependence between the load distribution on the blades

[4] Leading Edge

and the vorticity distribution in the domain: in fact, in order to calculate the aerodynamic load, it is necessary to have evaluated the velocity induced on the rotor by the distribution of the free swirling elements but their intensity and thus the shape and the evolution of the wake depend in turn on the unknown load distribution. Being null the asymptotic velocity of the flow, an accurate knowledge of the velocity field nearby the body that depends exclusively on the vorticity distribution in the domain plays a crucial role in determining the aerodynamic loads on the blades correctly.

It has been extensively highlighted that the analysis method this work of thesis exploits lies on the hypotheses of non-viscous and incompressible flow, therefore it was decided to carry out some numerical simulations with a –1 *deg* blade pitch angle and a rotational speed of 340 RPM, resulting in a Mach number at 75% blade span ($M_{0.75R} \approx 0.45$) such that the density can be considered constant and a Reynolds number ($Re_{0.75R} \approx 6.5\times10^6$) sufficiently high to assume the viscous effects negligible outside the boundary layer. Thereby, in view of a comparison with report data, the Prandtl-Glauert transformation for compressible flow problems has been deployed:

$$C_{p,comp} = \frac{C_{p,incomp}}{\sqrt{1-M_{0.75R}^2}} \tag{5.1}$$

The analyses have been conducted adopting a *fully-free* wake model whose time evolution is calculated taking the local effect of all computational elements inside the domain into account; in this way it is possible to simulate the deformations a real wake shows, such as the roll-up at the blade extremities.

The *near wake*[5] consists of 6 panels – as many as needed to cover the distance between the blade itself and the one that follows during the first revolution. This number is the result of a trade-off between the computational advantage of moving the conversion zone downstream and the lack of chance to push it any further due to a panel wake – body interference that gives rise to a divergent solution. The scope of the near wake is related to the time step duration: in order to detect a wake of satisfactory-quality, this has to be fixed to roughly 0.009 seconds; and having set a GEOROT(2,3) at 340 RPM and 15 revolutions of the proprotor around its own axis (which means about 2.647

[5] In a vorton method, this indicates that transitional portion of wake modelled through panels that the TE releases, up to the *far wake* made of vortons.

seconds for the whole simulation), the angle the blade encompasses in a single time step is $d\varphi$=20 *deg*.

Moreover, among the parameters already described in Chapter 3 that shape a rotor wake, the model of *vortex core* is of significant importance: the one employed is the Rankine model with a radius that $r_c/D \approx 0.07$.

One has wanted to emphasise the cut-off effect of the wake, demonstrating whether a number of time steps established for the wake less than the number of total time steps causes a considerable loss of information and therefore a reduction in the solution accuracy. Figure 5. 7 shows a comparison among wakes shot at the same time instant, with no cut-off and in case of cut-off respectively after 12, 9, 6 and 3 revolutions.

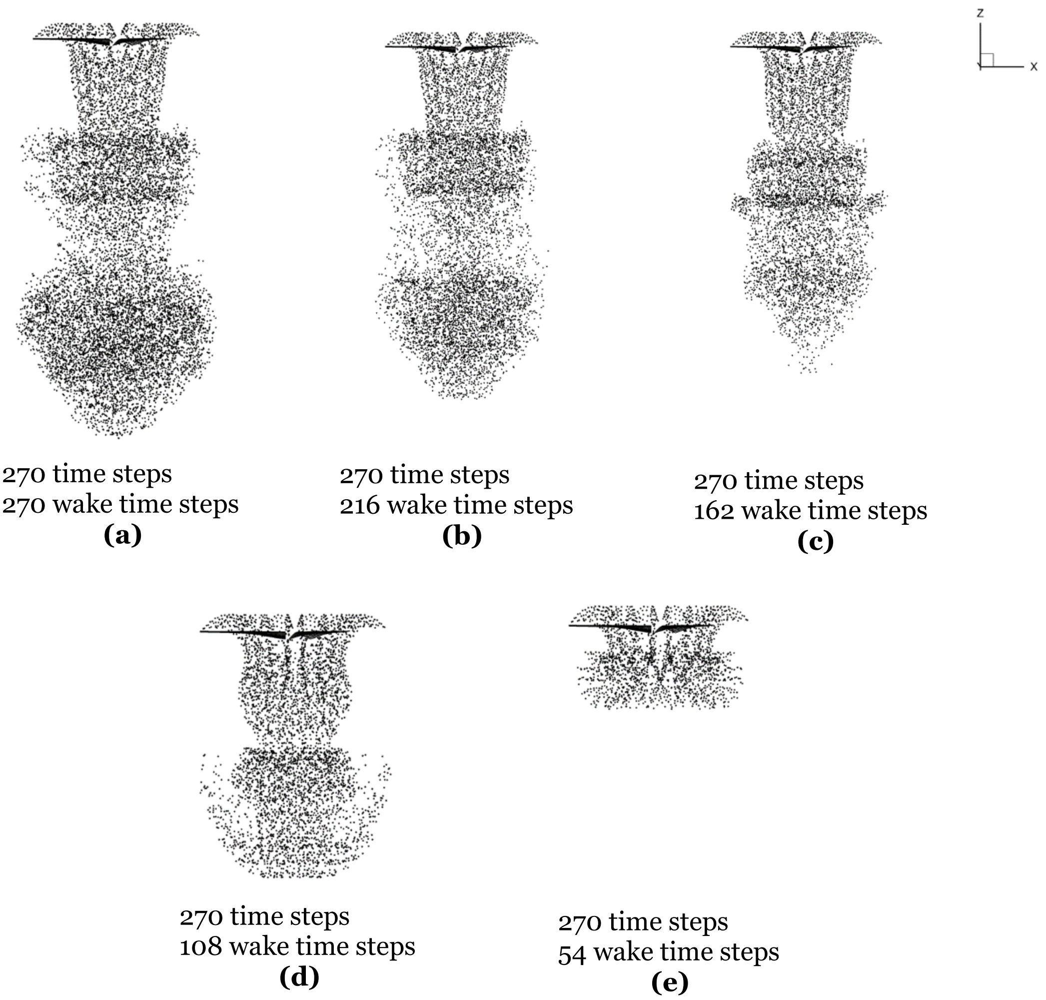

FIGURE 5. 7: Cut-off effect: vorton wake of a proprotor after 15 revolutions with (a) no cut-off; (b) cut-off after 12 revolutions; (c) cut-off after 9 revolutions; (d) cut-off after 6 revolutions; (e) cut-off after 3 revolutions.

Removing computational elements in the domain results in an abrupt variation of the vorticity field and consequently a substantial difference in the shape of the wake can be noted. Obviously short wakes are not appropriate when the far field is relevant for the study, for example when the focus of the analysis is the interference of the propeller wake with tail empennages. Nevertheless this truncation does not reflect a remarkable difference in the values of the forces that act on the proprotor at the steady state. In the light of these results, a less complete – but a less hardware resource and time-consuming – simulation could be suitable for the evaluation of aerodynamic loads on the blades.

Starting from the equation 4. 7, the thrust coefficient C_T is defined as follows, where T is the thrust force that the proprotor is generating (*i.e.* the component of the force F_Z perpendicular to the rotor disk, evaluated through a pressure integral on the body surfaces), A is the actuator disk area ($A = \pi R^2$) and V_{tip} indicates the tangential speed at the tip of the blade ($V_{tip} = \Omega R$):

$$C_T = \frac{F_Z}{\rho A V_{tip}^2} = \frac{T}{\rho \pi \Omega^2 R^4} \qquad 5.\ 2$$

The hover condition is determined by imposing the equality between the aircraft weight and the force generated by the rotary wing devices. As for the configuration under examination, the V-22 *Osprey* features two proprotors symmetrically positioned with respect to the longitudinal plane of the rotorcraft; from the balance of forces and moments acting on it, each rotor must lift an amount equal to half the aircraft weight. In Figures 5. 8 and 5. 9 the C_T that refers to the report has been evaluated taking into consideration the total design weight of the V-22 configured for the USMC, thus validating the VPM-method implemented by means of PaMS in terms of orders of magnitude. Particularly, the percentage errors of the thrust coefficients evaluated from PaMS results with respect to the report-based C_T amount to 3.6 – 4.5%. In Figure 5. 10 a comparison between thrust coefficients respectively computed through pressure integrals and the near-field Trefftz analysis in the case of no cut-off is reported. The results have already been corrected by means of (5. 1).

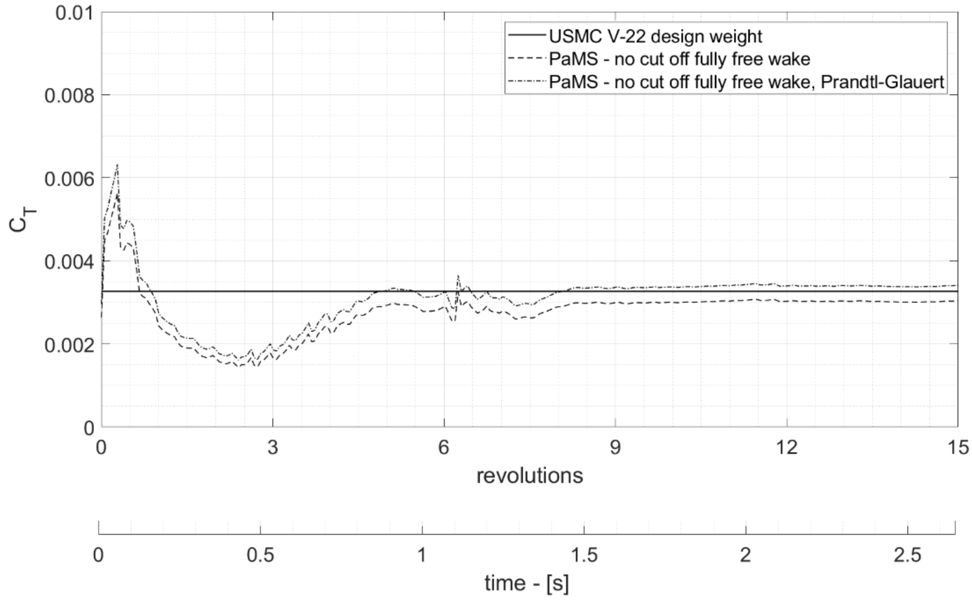

FIGURE 5. 8: Comparison between thrust coefficients: C_T based on PaMS results related to a fully free wake simulation with no cut-off and C_T evaluated from the USMC V-22 design weight.

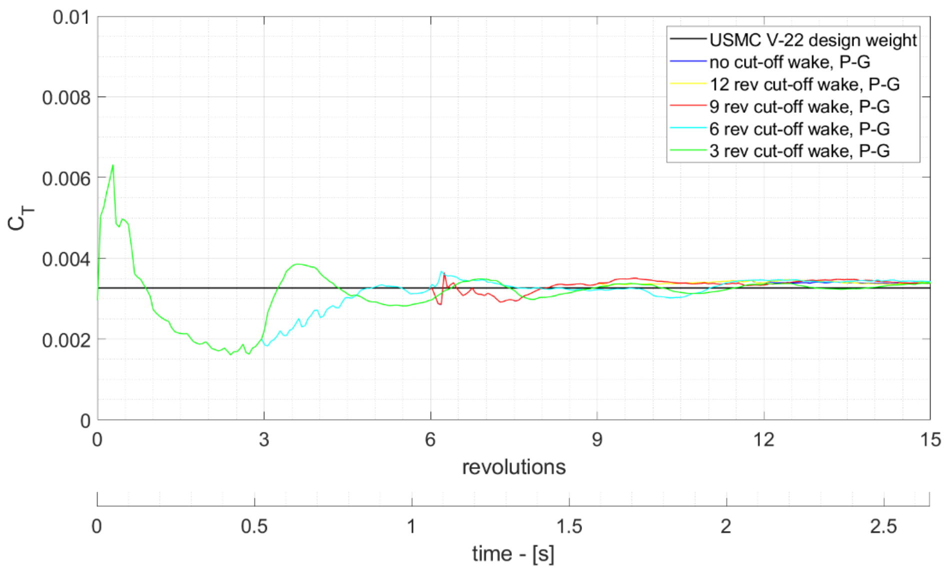

FIGURE 5. 9: Cut-off effect on thrust coefficient. The Prandtl-Glauert correction for compressible flows has been applied to PaMS results.

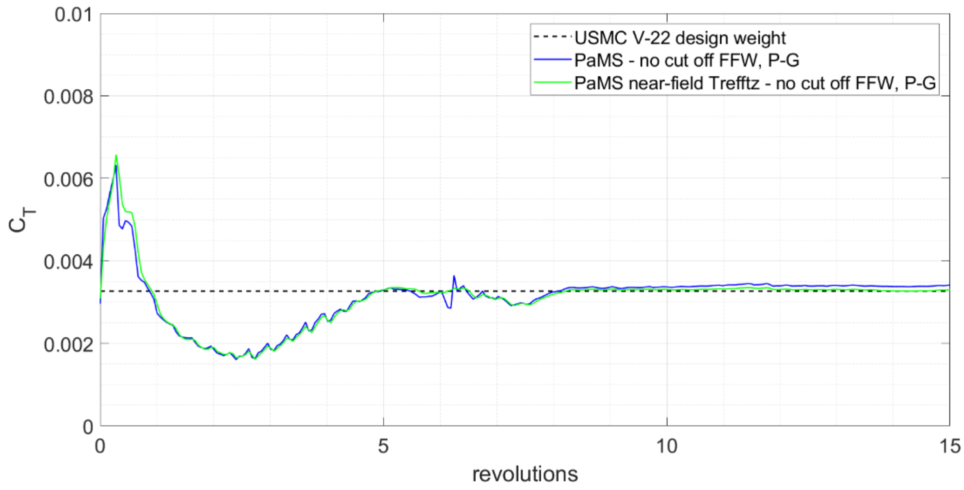

FIGURE 5. 10: Comparison between thrust coefficients related to a fully free wake simulation with no cut-off: the pressure integral based C_T and the near-field Trefftz based C_T. The Prandtl-Glauert correction has been implemented.

The thrust coefficients' trend is characterized by a high initial peak during the early time instants of the simulations. This is caused by start-up vortices, particularly intense for their sudden start that can be explained by means of the fact that the velocity axially induced by each computational element has not been properly calculated yet and the angle of attack of the blades is equal to the blade-twist (function of the radius, *i.e.* 8 $deg|_{0.50R}$) plus the pitch angle the rotor has been set at (– 1 *deg*); as time passes by, the downward-directed induced velocity that convects the wake downstream, reduces the angle of attack actually and therefore, the aerodynamic load along with the thrust coefficient. A steady state is eventually reached when the axial velocity is averagely constant.

Let us focus on the case of fully free wake with no truncation. As previously described, the high variation in load near the tip of the blades determines the release in the domain of very intense free vortices which, due to the rapid roll up of the whirling wake, combine into a particularly vigorous extremity vortex, whose trajectory could be captured through experimental observations. The numerical analysis carried out through the solver PaMS, allows capturing the trajectories of single swirling filaments instead. Figure 5. 11 shows the radial and the axial positions of the free vortices released at the sections pointed out in Figure 5. 11 (a). The tip vortex is the one generally taken into account: being the most intense, on the one hand it determines the greatest effect on the flow field and on the other one, its trajectory is the easiest to be identified. For the sake of clarity, also mid-section swirling lines have been highlighted. Due to the high blade-twist, a marked difference in the radial and axial wake contraction between the probed sections can be observed.

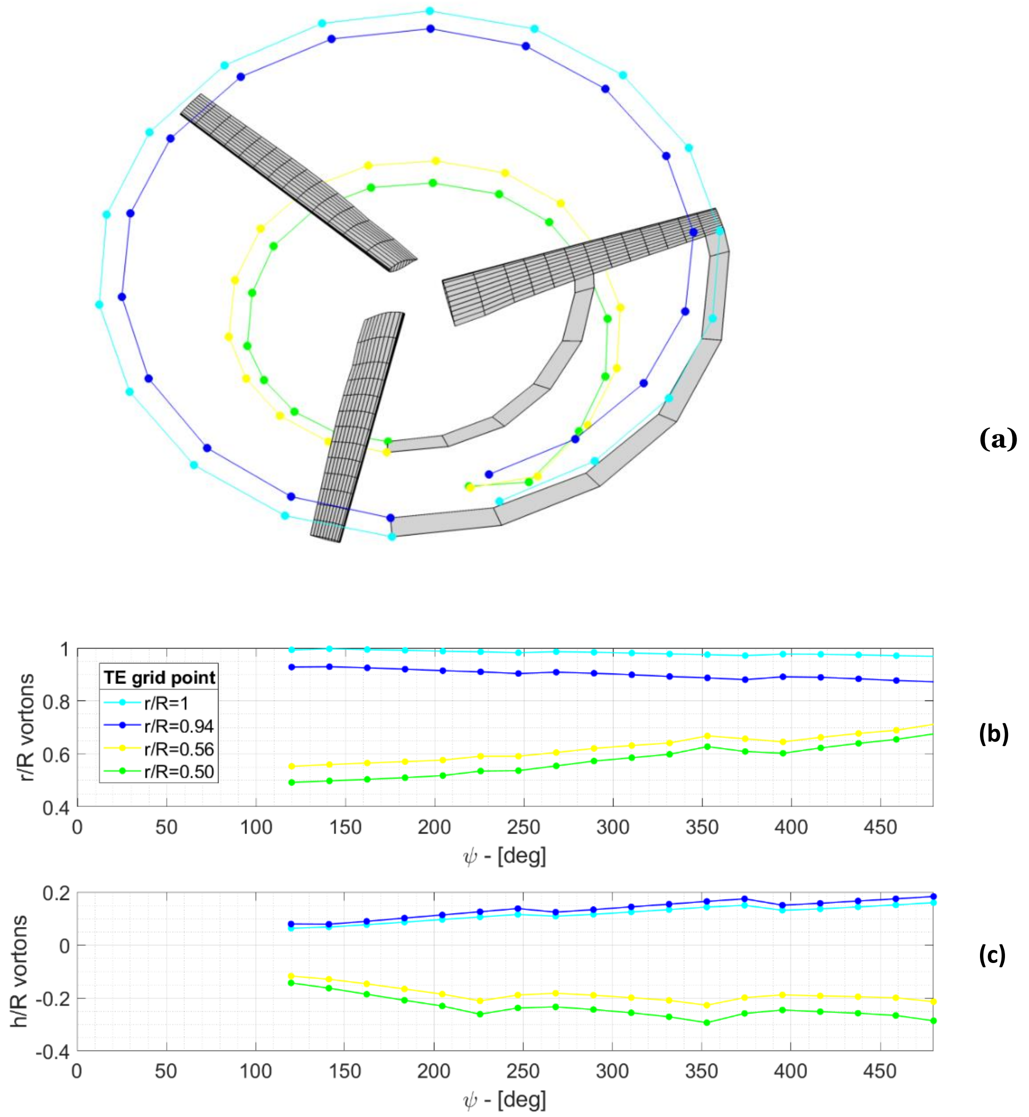

FIGURE 5. 11: Radial (b) and axial (c) positions of vorton wake lines highlighted in (a) during the first revolution after the 6-panel near wake.

Furthermore, in Figure 5. 12 the spanwise lift coefficient distribution has been represented. Precisely, the C_l is evaluated by means of pressure integrals on the chordwise panels and non-dimensionalised with respect to the local dynamic pressure, measured on the centreline, times the area of the blade strip one has been referring to. The spanwise C_l evaluation has been performed through the near-field Trefftz technique too. Also here the Prandtl-Glauert correction has been applied to take compressibility effects into account.

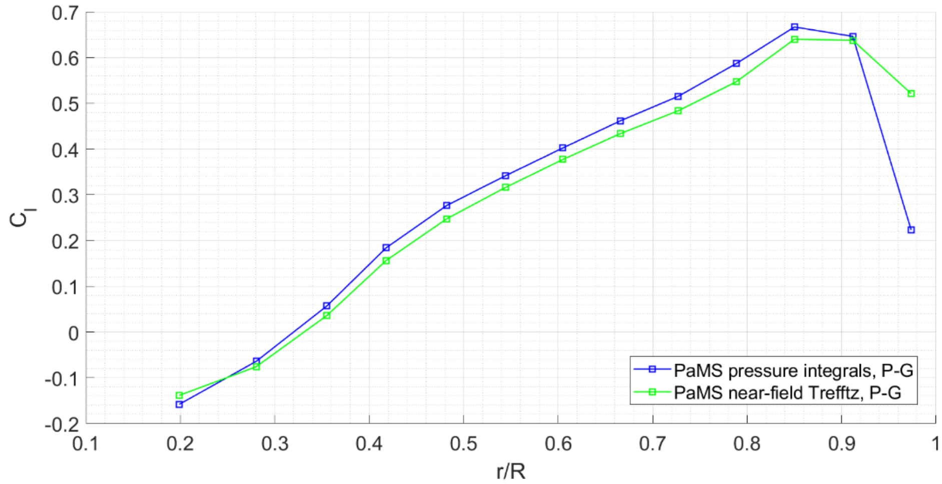

FIGURE 5. 12: Lift coefficient distribution along the blade span obtained by means of both pressure integrals and of the near-field Trefftz analysis. The Prandtl-Glauert correction has been implemented.

5.5 Computational Analysis of an Isolated Proprotor in Pure Tilt Motion

Another numerical investigation on the lone rotor has been performed and pertains to the same isolated proprotor model during a pure tilt motion. By *pure* tilt motion we refer to a longitudinal law of motion obtained by imposing the wing-to-wing rotornacelle axis to stand still. Then considering the reference frames PaMS features (see paragraph 3.4), the proprotor spins around its own axis and tilts around the space-fixed axis at the same time, so that the rotor axis is always contained in the $x - z$ plane ($\equiv X - Z$ plane) and hence it rotates around the Y-axis, describing a perfect quarter of a circle. For clarification purposes, please refer to Figure 5. 13.

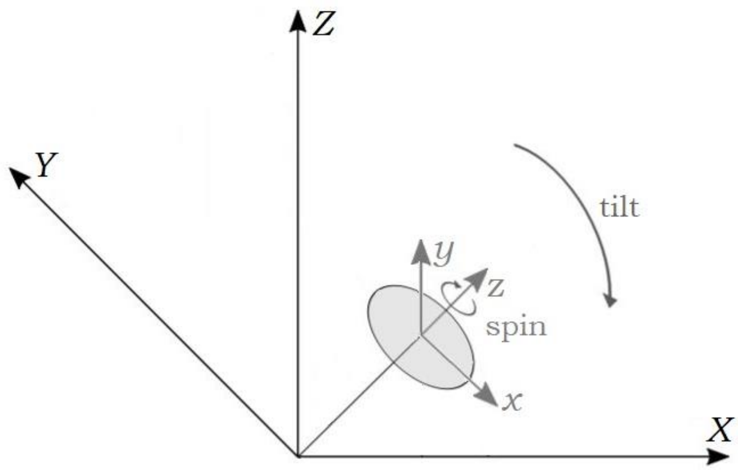

FIGURE 5. 13: Explanation of the motion law applied in Appendix B. In this layout the proprotor is represented by its actuator disk.

A suitable set-up congruent with the input data that PaMS requires has been created (DATAIN file reported in Appendix B). In particular, this peculiar motion has been obtained through combination of an angular speed around the third body-axis (*i.e.* a GEOROT(2,3) for spinning at 370 RPM) and the rotation of the nacelle is provided by a SYSROT(2,2), whose velocity is evaluated imposing that a quarter of revolution has to be covered in the tilting time ($\frac{\pi}{2}/4\ seconds$ = 3.75 RPM in the current work). The observant reader has surely noticed the introduction of a SYSTRA(1,3) that interprets the eccentricity of 1.230 metres with respect to the tilt pivot, derived from geometrical constraints. In Figure 5. 14 a V-22 *Osprey* is ideally depicted in subsequent moments of the tilting phase. Another insight into the kinematics of the motion is provided by Figure 5. 15, where respectively the time history of the proprotor centre coordinates and the angles between namesake axes – belonging to the body reference frame and to the global one – are shown. To conclude the description of the motion, the time evolution in the global (time- and space-fixed) reference system of one point belonging to one of the three blade tips is plotted in Figure 5. 16. As expected, a general sinusoidal trend (whose maximum amplitude is equal to the proprotor radius) can be recognised for the three components. This is obviously due to the revolutions of the proprotor around its own axis. Being the motion planar, the evaluation point *Y*-coordinate is characterised by a simple harmonic oscillation. For the *X*- and *Z*-coordinates, the oscillations are shaped by the tilt rotation: in particular, it can be observed that at $t = 0\ s$, when the rotor shaft is aligned vertically, the probed point third coordinate reflects the tilt eccentricity. This displacement turns into the first coordinate when the nacelle is positioned along the X-axis (at $t = 4\ s$).

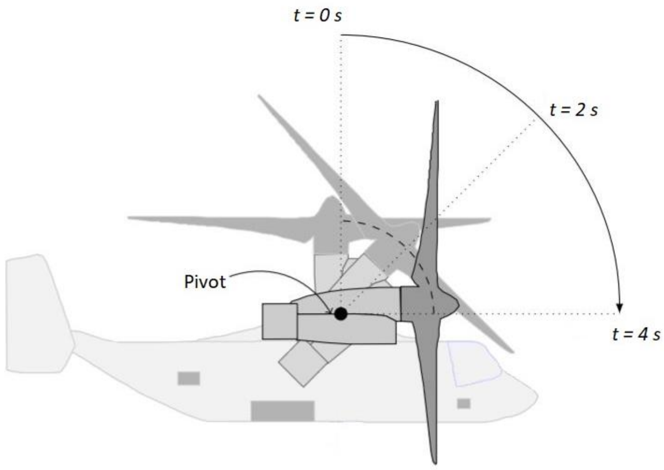

FIGURE 5. 14: Path of the V-22's rotor shaft during a 4-second tilting phase.

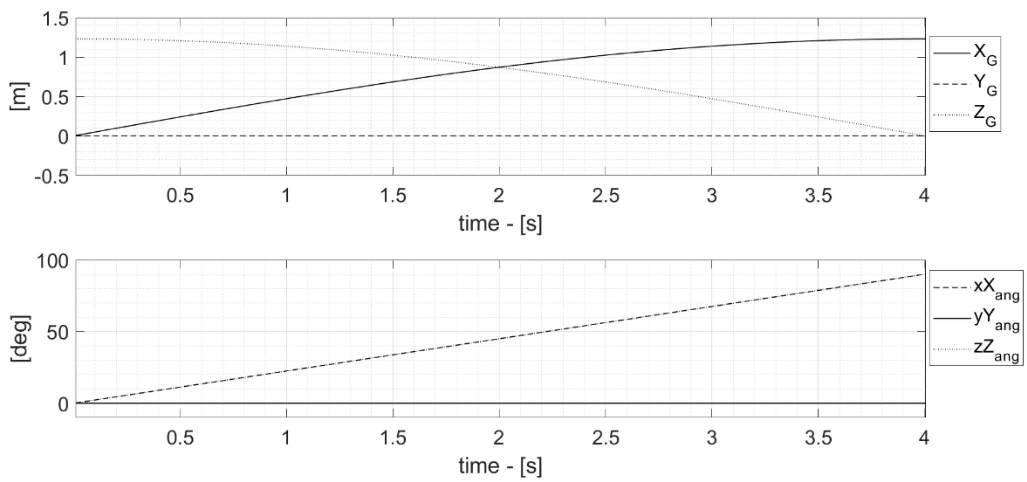

FIGURE 5. 15: Time history of the proprotor centre position and of the angular displacement between the local and the global reference systems.

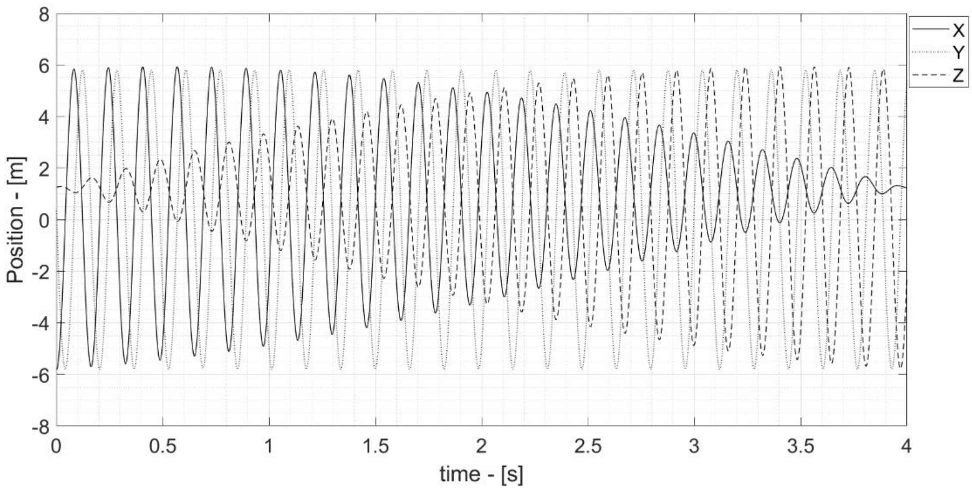

FIGURE 5. 16: Trajectory of a blade tip point in the global reference system during a 4-second tilting phase.

As previously stated, it is dutiful to remark again the motionlessness of the pivot during the conversion mode. Therefore this schematisation does neglect the forward translation generated by the thrust vector that is lying along the flight direction and makes the simulated case a numerical equivalent of a bench test. This choice is related to the fact that the approach in PaMS is purely kinematic and hence the trajectory of the pivot due to the tilting thrust direction is unknown. As a consequence the coupling of the dynamics equations with the VPM is not in the scope of the present dissertation and it is deferred to future works. In addition the superposition of both translations and rotations around multiple axes into a three dimensional environment makes the simple motion instructions present in the DATAIN file insufficient as they are. Although PaMS capabilities can be extended by means of additional support routines whose role is to efficaciously implement general motions.

The computational analysis introduced so far has been carried out by simulating a 3-panel *near wake,* the maximum workable number not to have any body-wake interference at any time instant during the whole analysis. The time evolutions of the components of the force acting on the body and the resultant force are reported in Figure 5. 17. Again, the high peak at the beginning is due to start-up vortices. Once the induced velocities on each element start being calculated, the wake is pushed downstream and the abrupt variations damped out. Since the tilt period is longer than this state and the modulus of the aerodynamic force almost constant, one can conclude that the system makes for a quasi-steady condition. Thereby the curves of interest have to be evaluated at the steady state, so when the transient could be considered as decayed. The small oscillations around the average values can be interpreted as the blade-wake interaction effect. Furthermore, as expected, the major contribution to the thrust vector is given by the F_Z for the first half of the tilting phase, rather than the F_X during the second half. After the tilt has been completed, the F_X-component is the whole thrust.

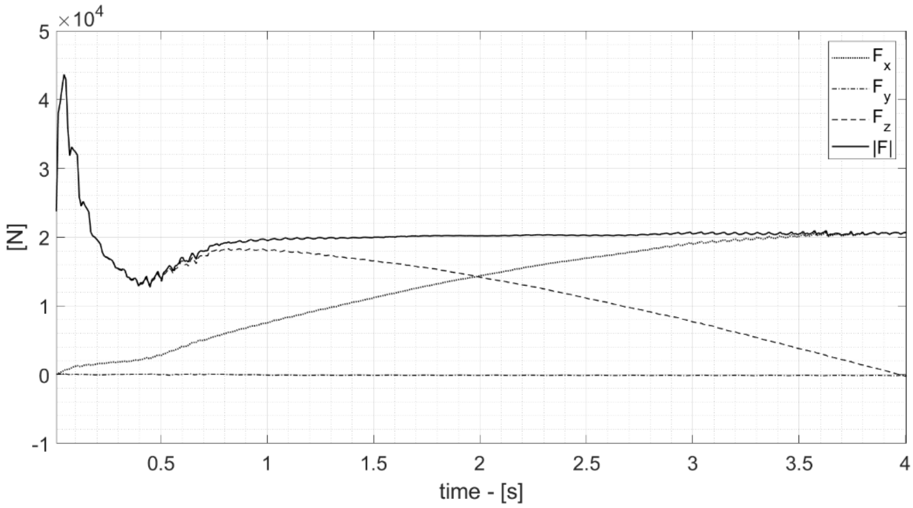

FIGURE 5. 17: Time history of the force components acting on an isolated proprotor during a 4-second tilting phase.

Finally, Figure 5. 18 shows the vorton wake shot at six different moments of the simulation.

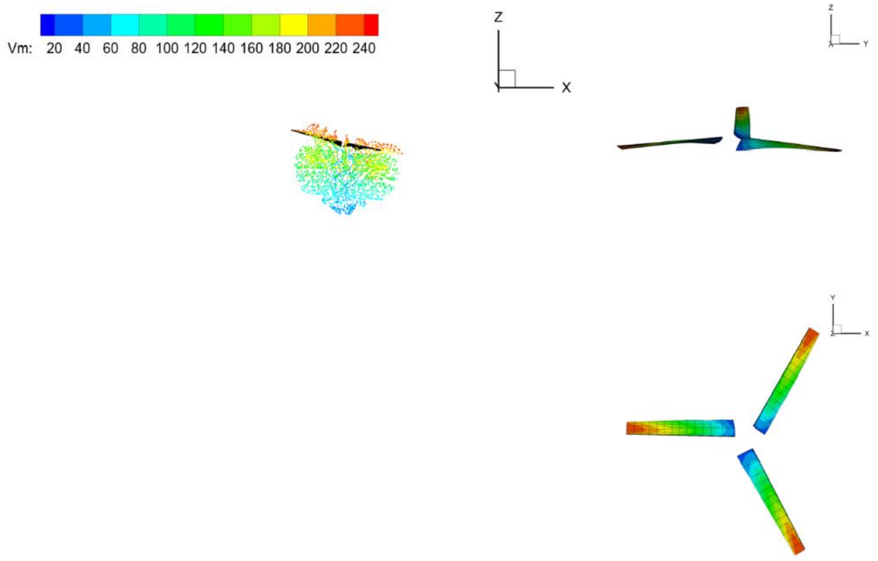

(a) t = 0.54 s

$\theta_t \sim 12^\circ$

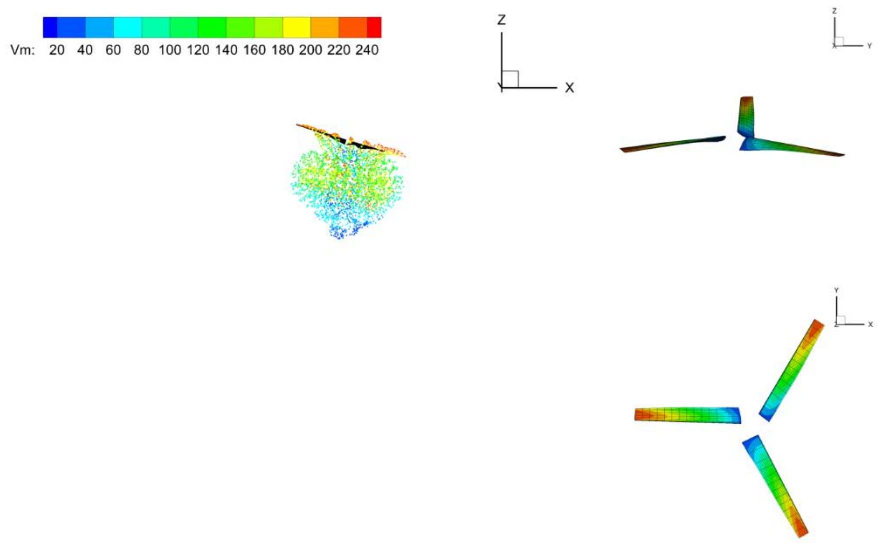

(b) t = 0.756 s

$\theta_t \sim 17^\circ$

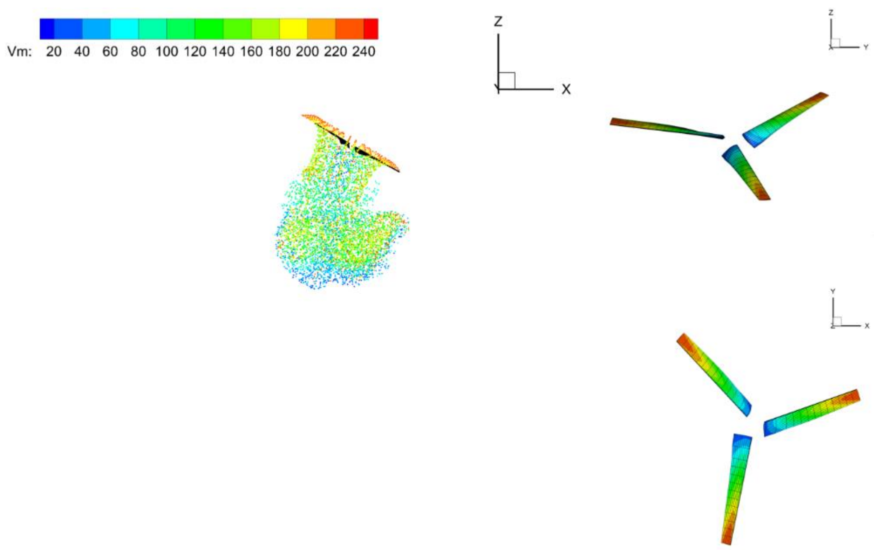

(c) t = 1.332 s

$\theta_t{\sim}30^\circ$

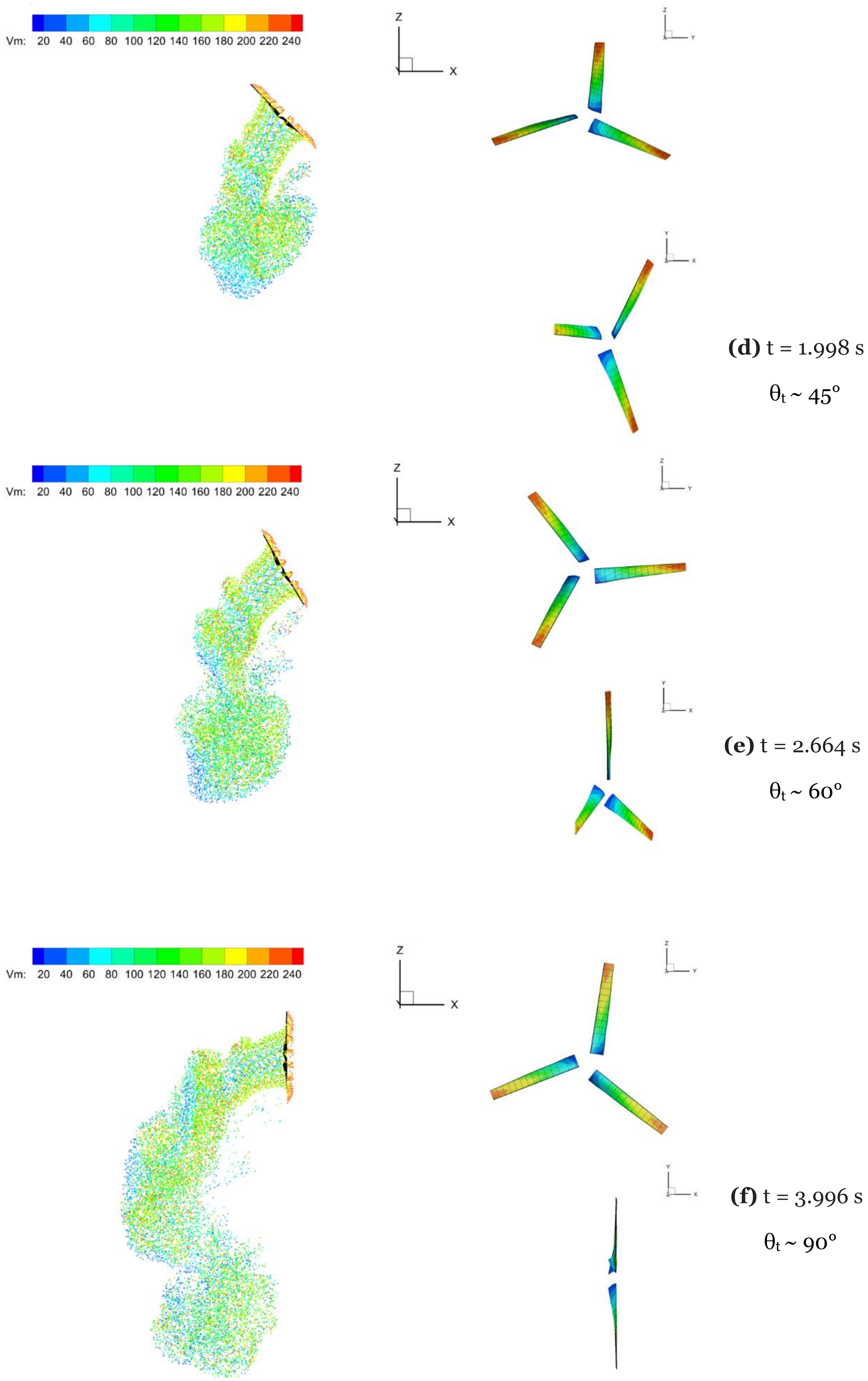

FIGURE 5. 18: Velocity magnitude contoured vorton wake of an isolated proprotor in tilting phase at six different instants. The tilt angle θ_t refers to the ZZ_{ang} of Figure 5. 15.

CHAPTER 6

A Rough Tiltrotor

After some preliminary analyses on the isolated proprotor discussed in the earlier chapter, a rough tiltrotor configuration consisting of the very same proprotor and a model of wing is going to be considered. The steps that lead to the study are the ones previously outlined and quite similar settings, although arranged for multibody simulations, are taken into account for the purpose of examining the rough tiltrotor in a hovering flight and during a pure tilt motion.

6.1 Wing Model and Meshing

While the proprotor geometry file is ready to use, a mock-up of the V-22's wing has to be created on purpose through the *Wireframe & Surface Design* tool in CATIA, considering the technical specification listed in Table 5. 1. The wing airfoil (*Bell* A821201) coordinates are available on the NASA website – Technical Memorandum 102244.

Moreover, it has to be pointed out that due to the aircraft symmetry with respect to the longitudinal plane, only half of the wing has been taken into account. Its dihedral and sweep angle are highlighted in the following front and top view respectively.

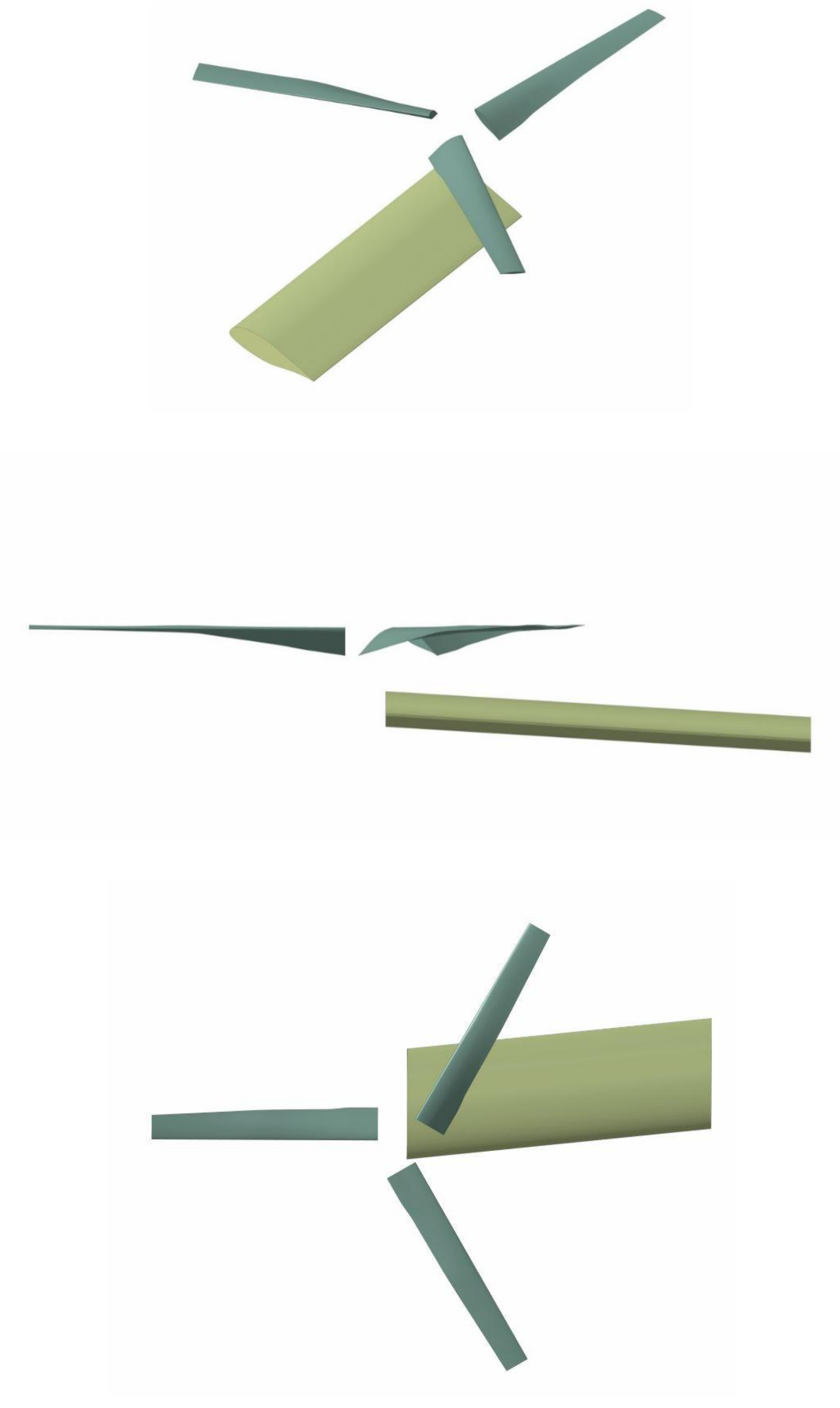

FIGURE 6. 1: (from the top to the bottom) isometric view, front view and plan view of the CAD target rough tiltrotor [CATIA *Wireframe & Surface Design*].

The meshing strategy traces the one employed for the proprotor (see paragraph 5.3) and is based on the need to keep the overall number of panels the bodies are discretised with as limited as possible not to overcharge the computational cost and the time complexity of a simulation. For this reason, the mesh shown in Figure 6. 2 has been chosen as the best fit. The semi-wing has a simpler geometry than the proprotor blade, no taper ratio nor difference in thickness between the root and the tip section have been detected, and hence a more conventional panel distribution is applied. The node distribution has been intensified nearby the wing LE as well as for the proprotor blade, and at the TE too. In the spanwise direction, the panel density has been increased towards the wing tip, that is right where the proprotor is mounted and thus the main propeller-wing interaction is expected.

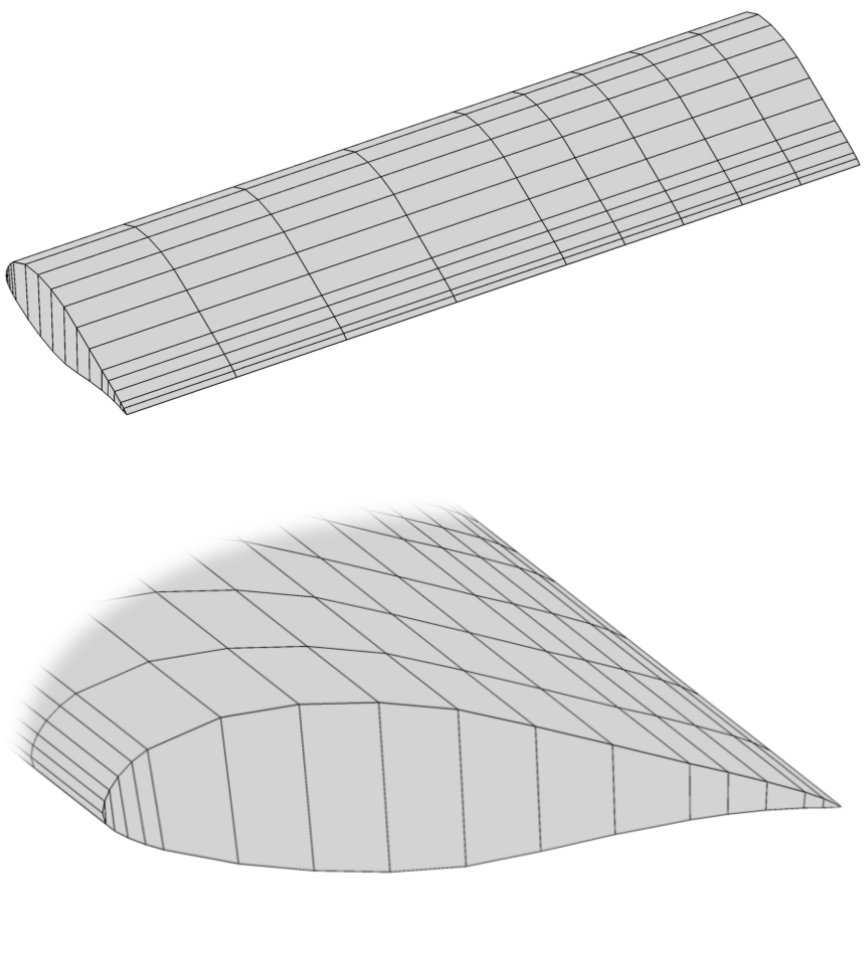

FIGURE 6. 2: Wing mesh, spanwise (above) and chordwise panel distribution (below) [MSC Software Patran].

6.2 Proprotor-Wing Interaction

At this stage it is possible to include the half-wing into the analyses performed in Chapter 5 on the lone proprotor, that for both the hover and the transition phase simulations it has been considered as a non-aerodynamic body, so that it influences the solution being a hindrance to the rotor wake.

Before getting started, in order to thoroughly understand the settings, the complete DATAIN files are reported in Appendix A (for the helicopter mode) and Appendix B (for the conversion phase). Here particular attention is paid to what concerns the definition of a multibody problem. As described in paragraph 3.4.2 related to PaMS architecture, as many *Geometry & Closure* and *Body Motion* sections are required as many bodies (*nbody*) are present. The latter deserves an insight and for this purpose, the one related to the wing and that referring to the proprotor are reported in Listing 6. 1 and 6. 2, both extract from Appendix B for the sake of completeness.

It is obvious that the aim of the two combined *Body Motion* sections is to correctly place the geometries one with respect to the other; the arrangement always pertains to the starting time and particularly this has to be stressed for the current cases where a relative motion between the bodies occurs. In order to implement the pure tilt motion (whose characteristics have already been described in section 5.4), the strategy adopted consists in aligning the wing-wing hinge axis to the global X-axis and – in a longitudinal view – locating the hinge point at the 25% of the tip section blade element. To do so, the wing has been shifted back along Y through `SYSTRA(1,2)=0.100` and down along the Z-axis by means of `SYSTRA(1,3)=-0.426` with respect to the global reference system. On the other hand, the proprotor has been translated to the wing tip so that its own axis is `SYSTRA(1,1)=-7.100` (meters) far from the symmetry plane YZ. At the same time the `SYSTRA(1,3)=-1.230` operation refers to the same eccentricity of the rotor centre with respect to the tilt pivot, already outlined for the isolated proprotor. Figure 6. 3 may help the reader since it shows the target configuration where these lengths have been highlighted. The same disposition has been adopted for the hover (Appendix A); of course, in this case, no `SYSROT(2,1)` has been enforced.

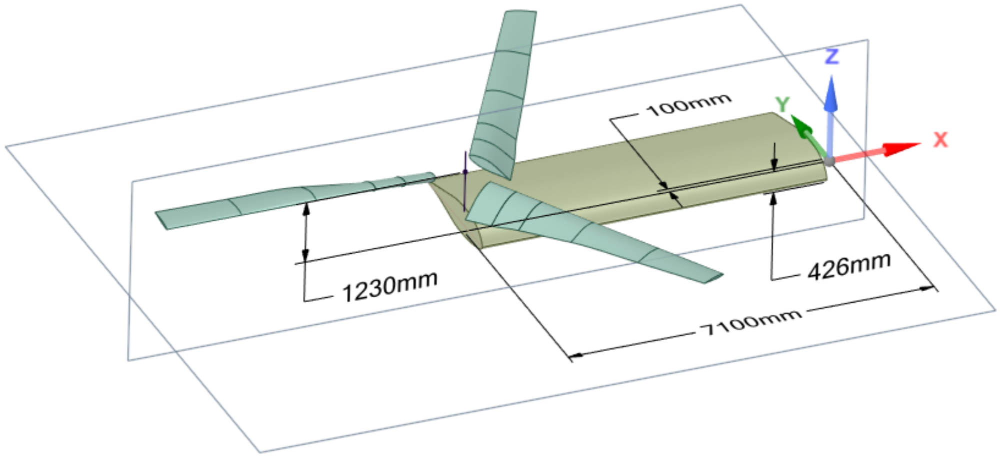

FIGURE 6. 3: Wing-proprotor configuration, reference lengths for the settings.

```
&GEOTRA   GT(1,1)=0.0       GT(1,2)=0.0       GT(1,3)=0.0       &END
&GEOTRA   GT(2,1)=0.0       GT(2,2)=0.0       GT(2,3)=0.0       &END
&GEOTRA   GT(3,1)=0.0       GT(3,2)=0.0       GT(3,3)=0.0       &END
&GEOROT   GR(1,1)=0.0       GR(1,2)=0.0       GR(1,3)=0.0       &END
&GEOROT   GR(2,1)=0.0       GR(2,2)=0.0       GR(2,3)=0.0       &END
&GEOROT   GR(3,1)=0.0       GR(3,2)=0.0       GR(3,3)=0.0       &END
&SYSTRA   ST(1,1)=0.0       ST(1,2)=0.100     ST(1,3)=-0.426    &END
&SYSTRA   ST(2,1)=0.0       ST(2,2)=0.0       ST(2,3)=0.0       &END
&SYSTRA   ST(3,1)=0.0       ST(3,2)=0.0       ST(3,3)=0.0       &END
&SYSROT   SR(1,1)=0.0       SR(1,2)=0.0       SR(1,3)=0.0       &END
&SYSROT   SR(2,1)=0.0       SR(2,2)=0.0       SR(2,3)=0.0       &END
&SYSROT   SR(3,1)=0.0       SR(3,2)=0.0       SR(3,3)=0.0       &END
```

LISTING 6. 1: Semi-wing *Body Motion* section, extracted from the DATAIN file (Appendix B).

```
&GEOTRA   GT(1,1)=0.0       GT(1,2)=0.0       GT(1,3)=0.0       &END
&GEOTRA   GT(2,1)=0.0       GT(2,2)=0.0       GT(2,3)=0.0       &END
&GEOTRA   GT(3,1)=0.0       GT(3,2)=0.0       GT(3,3)=0.0       &END
&GEOROT   GR(1,1)=0.0       GR(1,2)=0.0       GR(1,3)=0.0       &END
&GEOROT   GR(2,1)=0.0       GR(2,2)=0.0       GR(2,3)=370.0     &END
&GEOROT   GR(3,1)=0.0       GR(3,2)=0.0       GR(3,3)=0.0       &END
&SYSTRA   ST(1,1)=-7.100    ST(1,2)=0.0       ST(1,3)=1.230     &END
&SYSTRA   ST(2,1)=0.0       ST(2,2)=0.0       ST(2,3)=0.0       &END
&SYSTRA   ST(3,1)=0.0       ST(3,2)=0.0       ST(3,3)=0.0       &END
&SYSROT   SR(1,1)=0.0       SR(1,2)=0.0       SR(1,3)=0.0       &END
&SYSROT   SR(2,1)=3.75      SR(2,2)=0.0       SR(2,3)=0.0       &END
&SYSROT   SR(3,1)=0.0       SR(3,2)=0.0       SR(3,3)=0.0       &END
```

Listing 6. 2: Proprotor *Body Motion* section, extracted from the DATAIN file (Appendix B).

As a result of the operations implemented above, the final meshes at the starting time of both the hover flight and the tilt motion and at the end of the conversion phase are depicted hereafter.

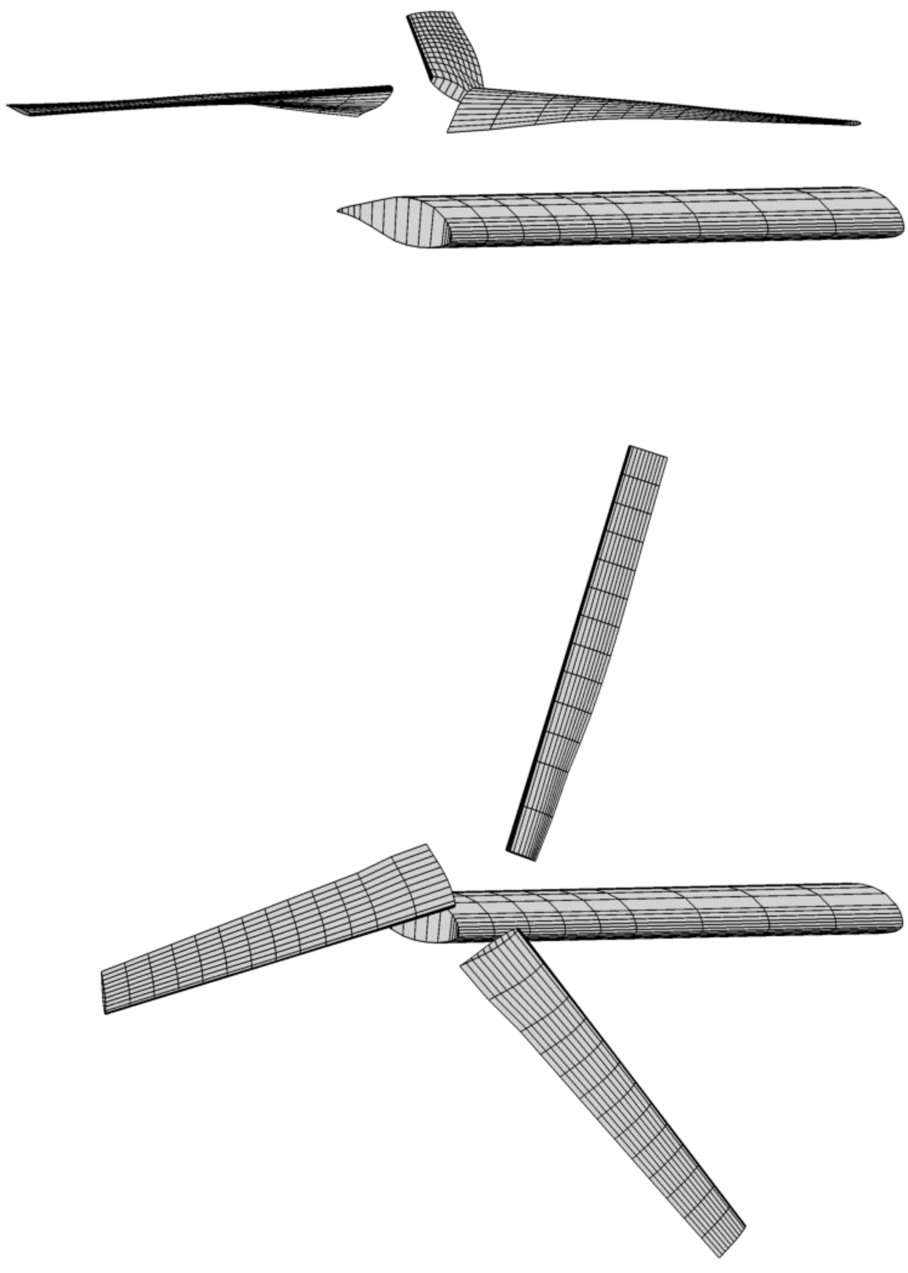

FIGURE 6. 4: Wing-proprotor configuration, assembly meshes: at $t = 0\ s$ for the hover flight and transition motion simulations (above), at $t = 4\ s$ – end of the transition (below).

6.2.1 Helicopter Mode

As far as the helicopter mode is concerned, in hover flight the proprotor performances are expected to be influenced by the presence of the wing underneath, since a considerable portion of this latter is located directly in the proprotor wake. This generates a three-dimensional flow distortion producing competing aerodynamic interactions. Expressly, from Figure 6. 5 it is evident that the rotor thrust coefficient is affected by a partial ground effect provided by the wing surface which is not beneficial in this case, being the proprotor only less than one wing chord beneath.

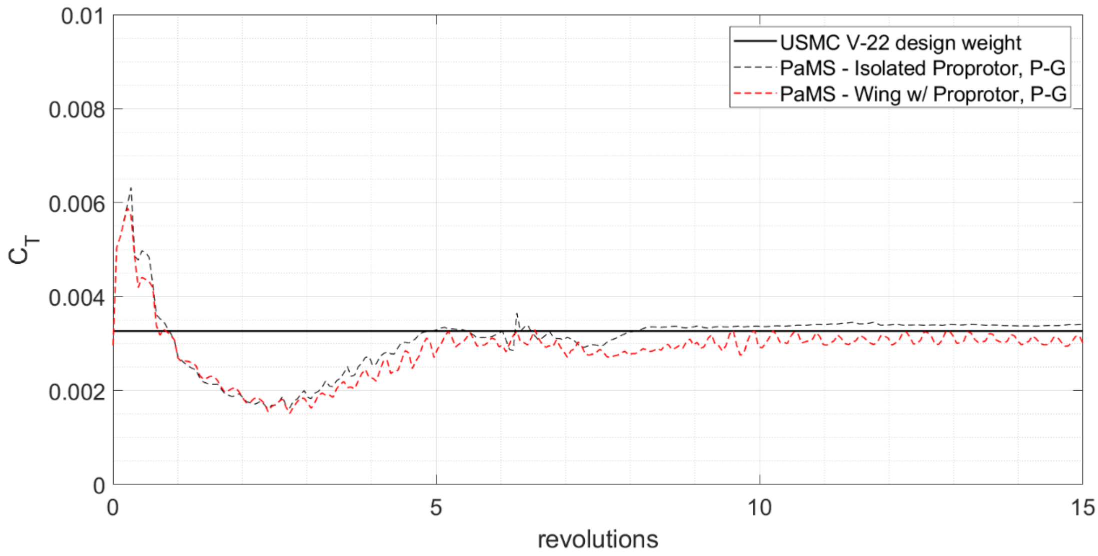

FIGURE 6. 5: Comparison between thrust coefficients: C_T based on PaMS results related to the isolated proprotor and to the rough tiltrotor; C_T evaluated from the USMC V-22 design weight. The Prandtl-Glauert correction for compressible flows has been applied to PaMS results.

Adopting a more general line of argument about the entire symmetrical configuration (see Figure 6. 6), the expansion of the proprotor wake along the upper surface of the wing causes spanwise flows towards the fuselage centre. The spanwise flows from the two wing tips meet at the centreline and give rise to an unsteady fountain flow, which gets recirculated into the proprotors. The momentum change produced from turning the flow from a spanwise to an upward direction causes a downward force on the aircraft. In addition to that, the main source of download is due to the vertical drag on the wing resulting from the fact that the proprotor wake impinges on the wing at an incidence angle of 90°.

For the V-22 *Osprey* and other tiltrotors with conventional aerodynamic layout it has been demonstrated that in hovering the vertical force pointing in the opposite direction of the rotor thrust and acting on the airframe is approximately 10% of the rotor thrust when only the wing is considered and about 15% when also the airframe is modelled.

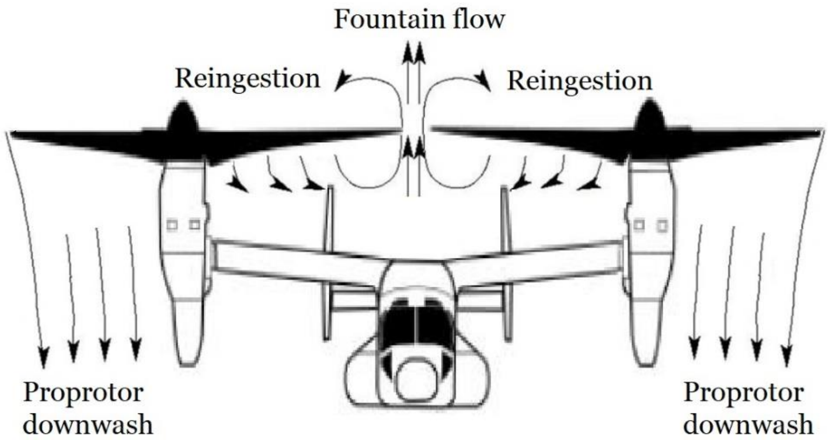

FIGURE 6. 6: Schematisation of a tiltrotor flow-field.

As stated, since during the whole simulation the wing works at very high angles of attack, the Kutta condition does not hold and no closure to the potential problem can be found. Moreover, owing to the fact that flow separation phenomena are beyond the method employed, the forces computed by the solver on the wing lower surface during the hover flight are not physical and hence should not be considered.

Nonetheless, in the perspective of a preliminary design project, for the formulation of a structural analysis to properly dimension the wing beam and of a flight mechanics study to formulate a suitable control law for the two tilting propellers (*i.e.* to find the relation $n = n(t)$ which allows a certain manoeuvre to be performed), it is indispensable to estimate the drag acting on the wing. Therefore, hereunder the application of three engineering methods for the estimation of the pressure drag at these high incidences has been developed. The relative results are reported in Table 6. 1.

1. By approximating the semi-wing object of the study with its mean plane, the computation of the drag force

$$D = \frac{1}{2}\rho V^2 S C_D \qquad 6.1$$

is related to the reference surface (half-span times the chord $S = {}^{b}/_{2} \cdot c$) exposed to the normal flow and a drag coefficient that depends on the geometry (specifically for a two-dimensional rectangle, on the ratio ${}^{b}/_{c}$). For the case of interest, being $1 < {}^{b}/_{c} < 5$, from the tabulated values $C_D = 1.19$. The velocity with which the flow impinges on the flat plate has been calculated as the average of the axial inductions on the wing from PaMS output at the final time instant of the simulation, so that the transient has decayed.

2. The actual gauge pressure distribution over the wing upper surface, shown in Figure 6. 7, has been extracted from PaMS and, for the same reason, also for this method the solution considered is the one at the end of the hovering time. With regard to the lower side, it has previously been pointed out that huge expansion is expected due to the flow separation and hence no valid information can be provided by the solver employed. So, here the pressure P_l has arbitrarily been set to a value such that $C_{p_l} = -0.1$, typical for separated flows behind both flat plates and backward-facing steps, and assumed to be uniformly distributed all over the wing lower surface. Furthermore, it should be noted that, since the flight condition is characterised by a null free-stream velocity, the classical definition of the pressure coefficient (Eq. 2. 81) would not hold and hence a reference speed equal to the one used in the first method has been applied. Then the pressure difference between the lower and the upper side of the wing is numerically integrated over the wing surface projected onto the mean plane.

3. Similar to the second approach, except for the fact that this method proves to be less conservative because it estimates the gauge pressure distribution on the lower side by taking into account this to be maximum near the wing tip where the proprotor is located and the greatest wing-proprotor interference occurs,

and $P - P_\infty$ almost zero at the root section. Intended to be more realistic, the implementation consists of an exponentially modulated sine of the P_l computed through the method (2):

$$\overline{P_l} = \frac{sin\left(\frac{2x}{b}\pi\right)e^{-5x}}{max\left[sin\left(\frac{2x}{b}\pi\right)e^{-5x}\right]}P_l \qquad 6.2$$

where the $\overline{[\cdot]}$ symbol refers to the spanwise pressure distribution and x runs along the spanwise coordinate according to Figure 6. 3.

Method	1	2	3
Description	Flat plate	Uniform distribution on the wing lower surface	Modulated sine distribution on the wing lower surface
Estimated pressure drag [N]	1594	617	473
Percentage by design weight	8.9	3.4	2.6

TABLE 6. 1: Estimation of the pressure drag acting on the test case semi-wing due to the proprotor.

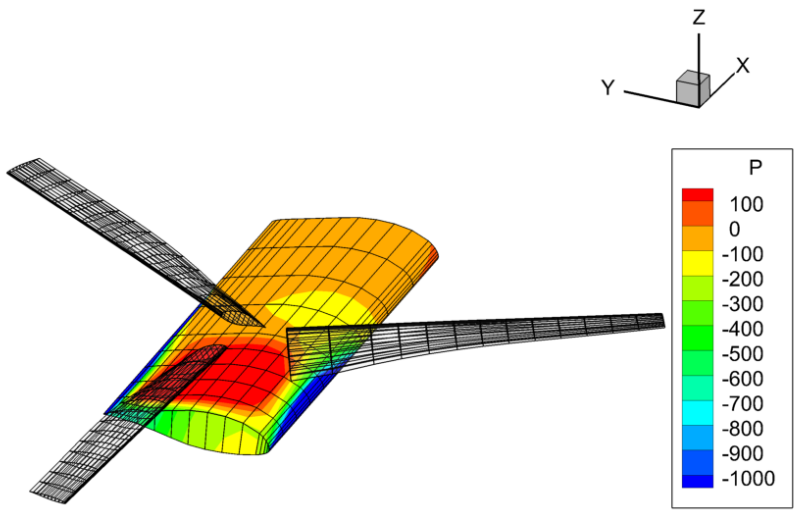

FIGURE 6. 7: Gauge pressure distribution over the wing at the end of the hovering time ($t \approx 2.65\ s$).

At this point of the dissertation, it appears to be clear that the aerodynamic load on the wing due to the rotor has the effect to reduce the net proprotor thrust for a given trim condition. A practical consequence of this fact is that for a given thrust, the power required to hover at the same flight level is obviously greater if compared to the isolated proprotor case. Although beyond the objectives of this thesis, an iterative procedure can be implemented in order to assess the needed revolutions per minute n_h of the proprotors which allow the hover, by adding the estimated drag value to the aircraft weight and finding by means of the proprotor characteristic curves the new n_h until the established convergence criterion is satisfied. As said, a shift of the hovering point towards higher values on n is expected. From a structural point of view, both the uniform and the modulated sine pressure distribution on the lower side of the wing imply a centre of pressure located over half of the semi-wing span ($X = -3.54\ (metres)$ and $X = -3.61\ (metres)$ respectively) and whose chordwise coordinate is $Y = 0.37\ (metres)$ behind the nacelle pivot (reference frame to refer to is the global one depicted in Figure 6. 3). As a result, noteworthy bending and torque moments are expected to act on the wing.

On the other hand, whether the influence of the proprotor on the wing has been demonstrated to be important, the influence of the wing on the proprotor performance is substantially negligible. So the proprotor performance is very similar to the one of the lone hovering proprotor (Figure 6. 5).

With the aim of stressing the wake distortion caused by the presence of the semi-wing and thus the symmetry breaking, Figure 6. 8 shows the vorton wake shot at four different time instants of the simulation.

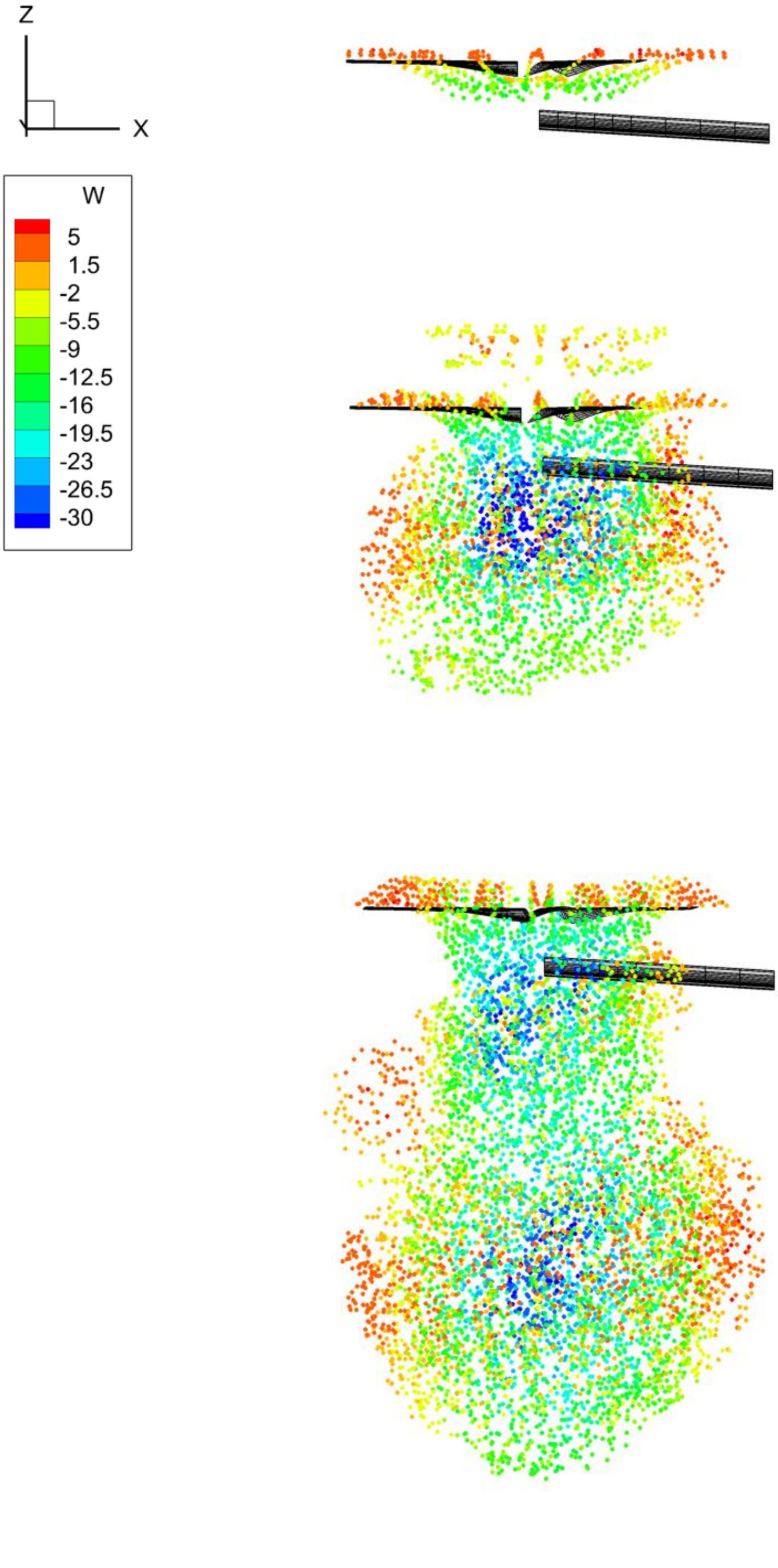

(a) t = 0.118 s

(b) t = 0.882 s

(c) t = 1.696 s

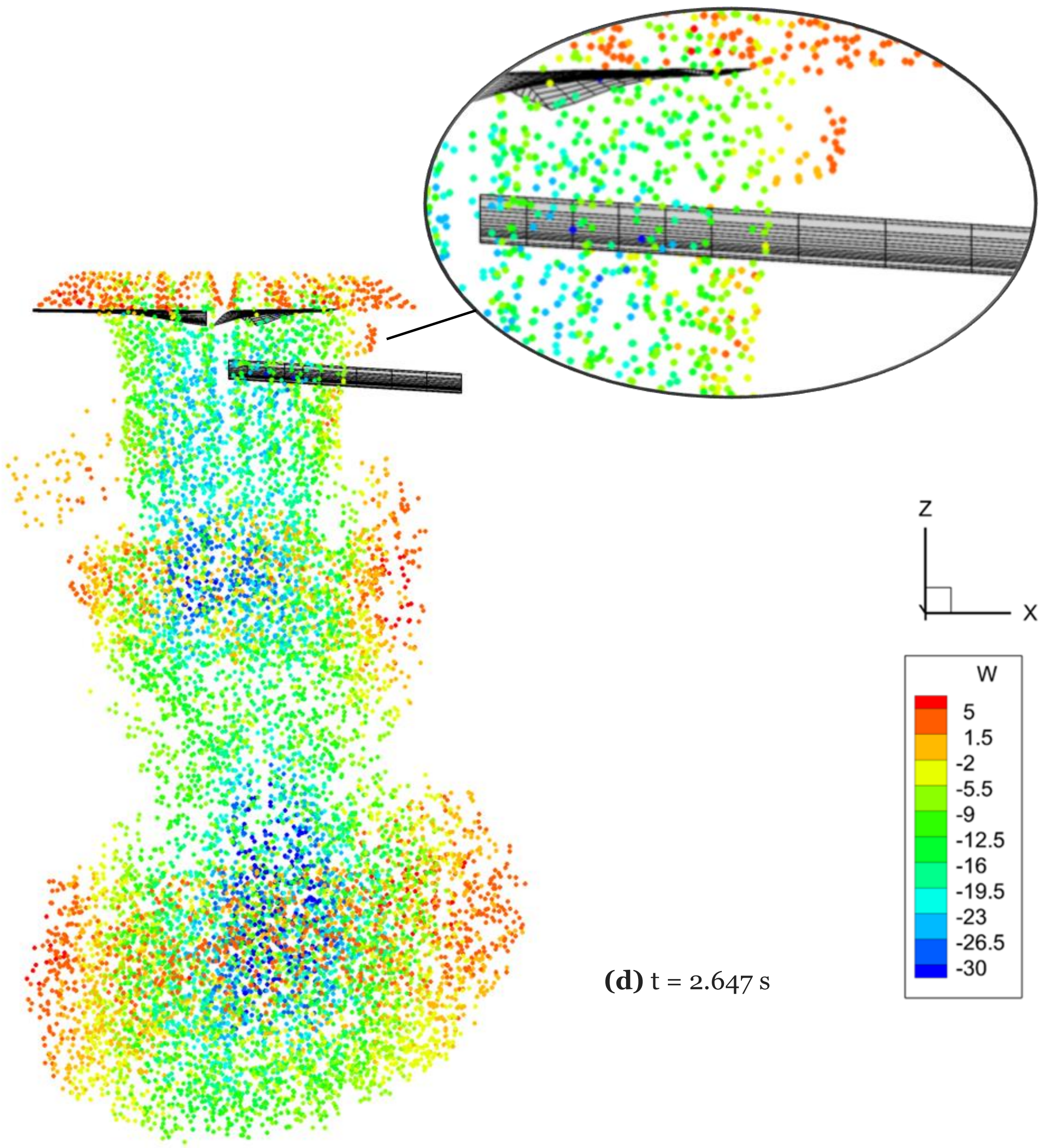

(d) t = 2.647 s

FIGURE 6. 8: Axial-velocity-contoured vorton wake of a rough tiltrotor in hover flight at four different instants.

As can be noticed, the axial velocity contour emphasises a fountain flow effect due to the high difference in element blade pitch along the proprotor radius as well as the isolated case. Besides, this is the result of the angle – as possible as unlikely – with which the blades have been keyed and equal to –1 *deg*, although the reason that led to this choice has been already given in paragraph 5.4.

Moreover, there is evidence of the loss of symmetry in the proprotor wake and the re-circulation generated by the ground effect on the wing side.

6.2.2 Conversion Mode

In the frame of a VPM applied to multibody configurations, a second simulation has been carried out concerning the very same semi-wing together with the proprotor during a 4-second pure tilt motion. Keeping in mind the overview about the setting presented at the beginning of the current chapter, the velocity-magnitude-contoured vorton wake is shown in the following figure, with particular focus on the zone where the interference is more relevant.

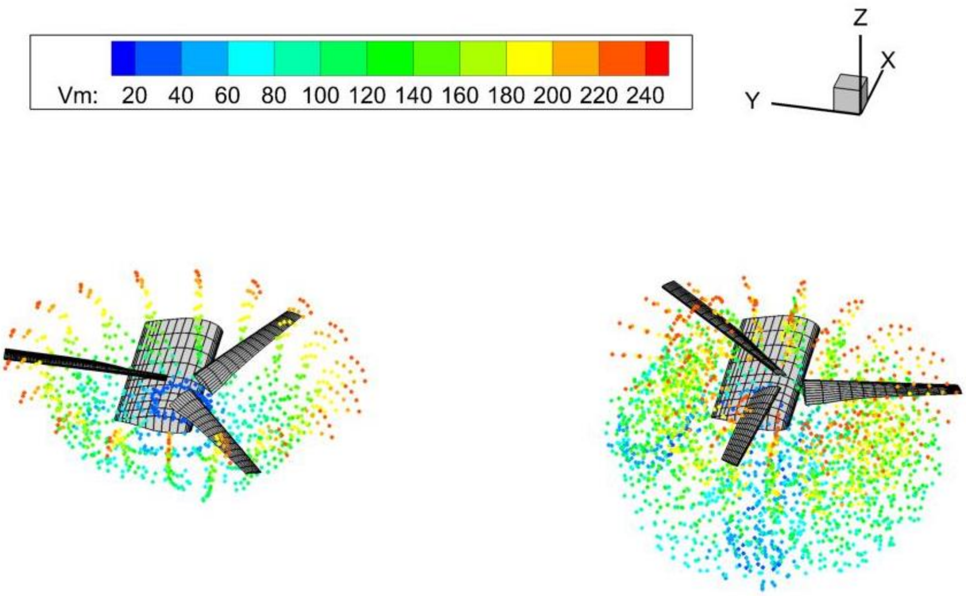

(a) t = 0.243 s

$\theta_t \sim 5.5°$

(b) t = 0.547 s

$\theta_t \sim 16°$

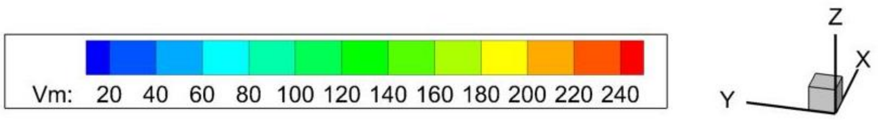

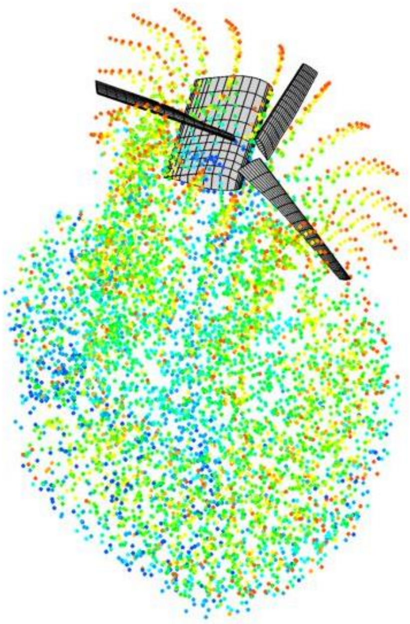

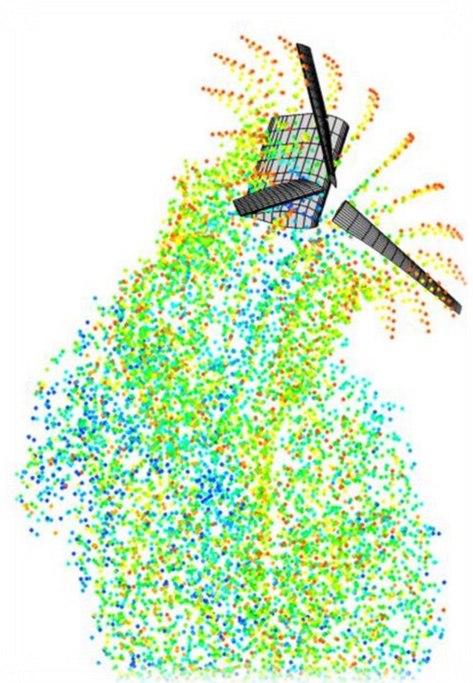

(d) t = 1.44 s

θ_t ~ 32°

(e) t = 1.998 s

θ_t ~ 45°

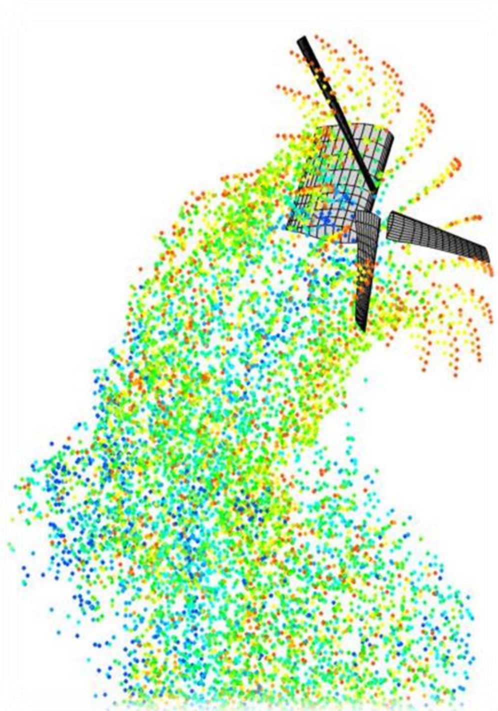

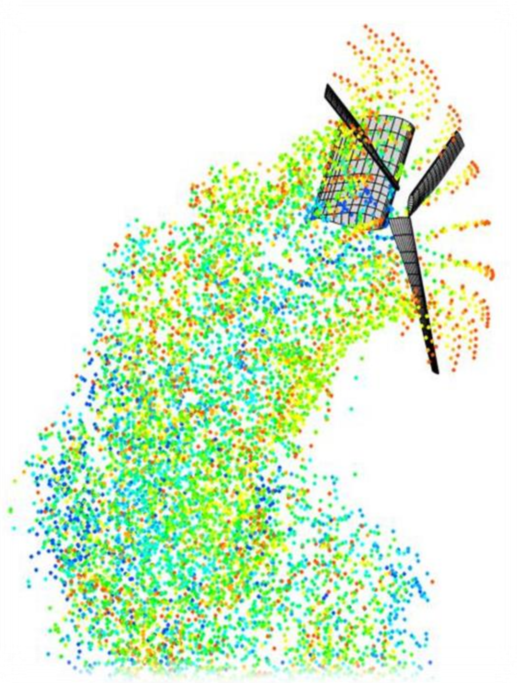

(f) t = 2.448 s

θ_t ~ 55°

(g) t = 2.898 s

θ_t ~ 65°

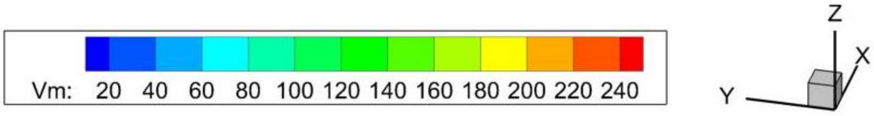

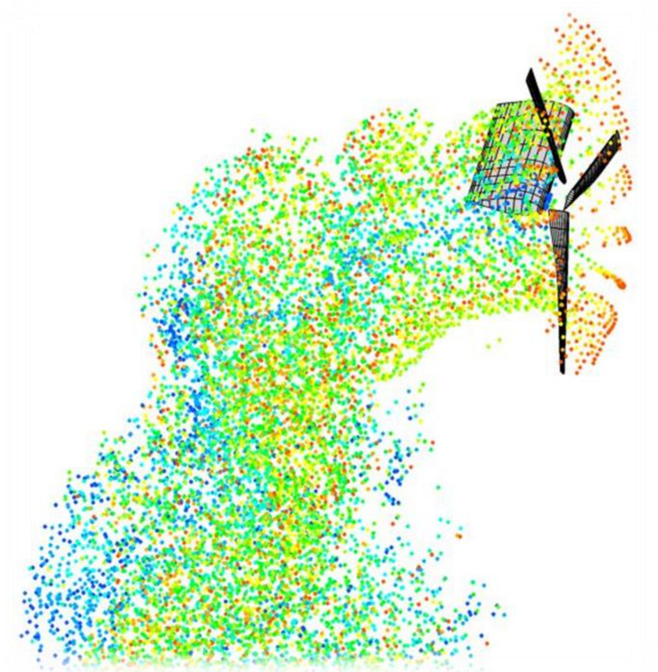

(h) t = 3.6 s

θ_t ~ 81°

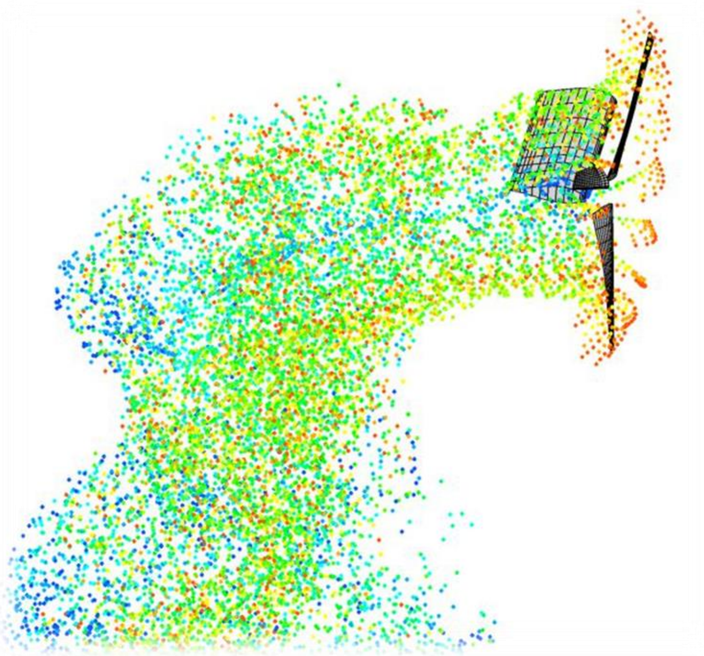

(i) t ~4 s

θ_t ~ 90°

Figure 6. 9: Velocity-magnitude-contoured vorton wake of a rough tiltrotor in tilting phase at eight different instants. The tilt angle θ_t refers to the ZZ_{ang} of Figure 5. 15.

As can be imagined, the presence of the wing is substantial at the early stages of the simulation since it offers the largest area to the flow and it would have been even more considerable if the proprotor had been located at half the span instead of at the wing tip. Compared to the isolated proprotor case (Figure 5. 18), it can be observed that it is harder for the wake to develop. As the tilt time goes by, the area exposed to the flow decreases, being related to the wing thickness rather than its chord thus one can state that the intersection area is an inverse function of the tilt time. This is confirmed by the fact that at the last instants the wake manages to stretch.

The time history of the forces has not been reported for the current case as the differences between these results and those concerning the lone tilting proprotor are minimal. Particularly, for the multibody simulation, harmonic oscillations stand out with a frequency that is associated to the blades passing close to the wing at each revolution, whereas the mean values overlap the results of the isolated proprotor analysis.

Moreover, taking into account the last time step, an approach similar to the one applied in section 6.2.1 has been employed here for the evaluation of the lift. At the considered time instant, the semi-wing is hit by the proprotor flow that is almost parallel to its chord; this condition makes the potential problem well-conditioned and no additional assumptions are needed, so PaMS output data are valid either on the upper and on the lower wing surface. The pressure distributions over the top surface of the wing and over the underside at $t = 4\ s$ are shown in Figure 6. 10; the corresponding pressure profiles at highlighted sections along the wing span are depicted in Figure 6. 11. Not surprisingly, the major influence takes place nearby the wing tip where a positive angle of attack is induced by the rotor spin – according to how it has been conceived – resulting in an overall lift acting on the semi-wing computed to be equal to about 3936 N. As a consequence, a severe torque and a bending moment arise on the structure. Moreover, this latter proves to be beneficial to the wing and helps to lighten it from the bending moment provided by the nacelle-and-rotor system weight. However, it has to be said that no information about the direction of rotation are available, so these considerations should be taken as a source of qualitative speculations only.

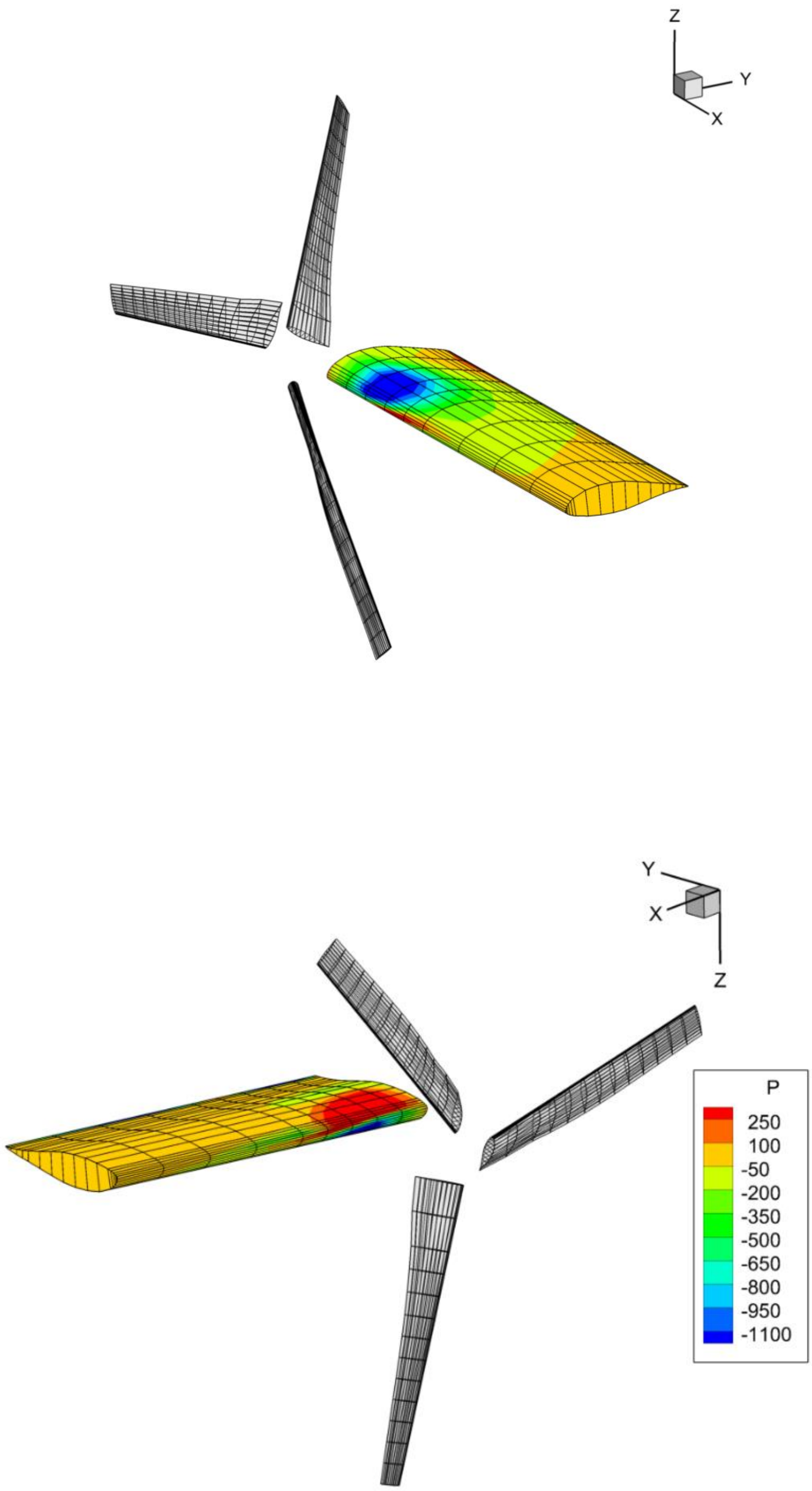

FIGURE 6. 10: Pressure distribution contour on the wing upper surface (above) and on the wing lower surface (below) of a rough tiltrotor at the end of a tilting phase.

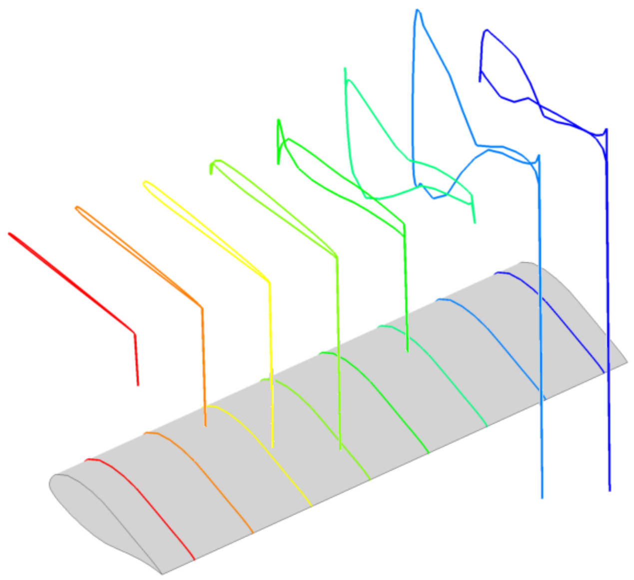

FIGURE 6. 11: Pressure profiles at highlighted wing sections (red – close to the root, blue – close to the tip) at the end of a tilting phase. Proprotor not depicted.

CHAPTER 7

A DESIGN OF EXPERIMENTS

7.1 An UAV Tiltrotor: General Overview

As a general rule, although sharing the same background ideas and technologies, an Unmanned Aerial Vehicle – especially of small dimensions – might be quite different from a similar full-scale aircraft in terms of project. Firstly, safety requirements and overall regulations are less strict than those concerning a manned flight machine. Also, as a consequence, the design of a drone is driven by mission-oriented and strongly cost-dependent key parameters. In the peculiar case of an UAV tiltrotor, the manoeuvrability is an issue of primary importance and the study of the extremely delicate conversion phase plays a crucial role in conceiving its remote control, besides other engineering choices that has to be made. For instance, a full-scale tiltrotor's control systems consist of both cyclic and collective pitches, together with a propeller-driven airplane controls; obviously a different solution which results in a less complex rotor hub and lower costs has to be found and implemented on a drone with tilting technology.

The aim of this chapter is to delineate a Design of Experiments with regard to the tilting propeller of an UAV that, unfortunately, due to Covid-19 restrictions, could not take place within the industrial firm of *Officine Meccaniche Irpine S.r.l.*

7.2 *E-Pteron*: Overall Design

The object of study of this section is the surveillance Vertical Take-Off and Landing Unmanned Aerial Vehicle named *E-Pteron*, where *E* stands for electric, while *Pteron* from the Greek means wing. Jointly developed by University of Naples "Federico II", the Second University of Naples SUN and the *Caltec* consortium – respectively responsible for the aerodynamic and structural analyses, the project of the flight control systems and the end-to-end design and manufacturing, E-Pteron is electrically powered and characterised by two lifting surfaces in a canard configuration. Moreover, as can be observed from Figure 7. 1, it is equipped with three fans targeted to enlarge its range of applicability: particularly, a main ducted rotor submerged in the fuselage and two fore-mounted counter-rotating tilting propellers, located at the canard tips. The former assists those latter when the aircraft is in helicopter mode. Some of its technical specifications are gathered in Table 7. 1.

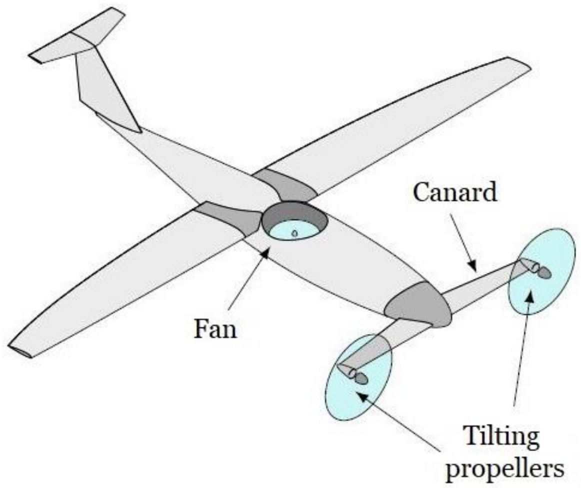

FIGURE 7. 1: E-Pteron's salient design features.

Length:	4.5 m
Wing span:	6.0 m
Maximum TO weight:	50 kg
Cruise speed:	65 km/h
Altitude:	1500 m
Range:	90 km
Tilting propeller diameter	0.32 m

TABLE 7. 1: E-Pteron's main technical specifications.

7.3 Bench Test

A thorough investigation about the conversion phase is essential for the purpose of the aircraft flight mechanics, since its manoeuvrability is strongly related to the time history of the thrust forces the two tilting propellers generate and, as stated, this acts on the project of the joystick by means of which the vehicle is controlled. In fact, in order for this to maintain a certain level altitude, a control law has to be implemented in terms of a power surplus to provide to the body-fan such that the loss in vertical component of the propellers' thrust while converting is counterbalanced.

The bench test would consist of evaluating the time evolution of the force acting on the propeller during the conversion through load cells. As already explained in paragraph 5.4, the conversion from helicopter to airplane mode occurs by means of tie-rods that constrain the axis of the propeller to cover a quarter of a circle, previously defined as pure tilt motion (see Figure 5. 13). A fair level of agreement expected between the experimental results and the solver outputs could enrich the number of test cases that have allowed for the validation of the vorton method.

As it could not be possible to apply a reverse engineering on the actual E-Pteron's fore-mounted propeller, the simulations that follow have been carried out on a generically-shaped 5-bladed propeller, regardless of its geometry at this stage.

First of all, with the intention of assessing the feasibility of computations throughout the entire range of its working angular speeds, some hover flights have been simulated by setting, in a rational way, increasing RPM and by means of pressure integrals the value of the thrust forces are known. The results are collected in Table 7. 2, where it can be noticed that 6 revolutions per minute are excessively low to make the propeller wake develop through the solver.

RPM	6	60	600	6000
Thrust [N]	---	≈ 0.001	≈ 0.117	≈ 11.7

TABLE 7. 2: Thrust force in hover flight at different angular speeds.

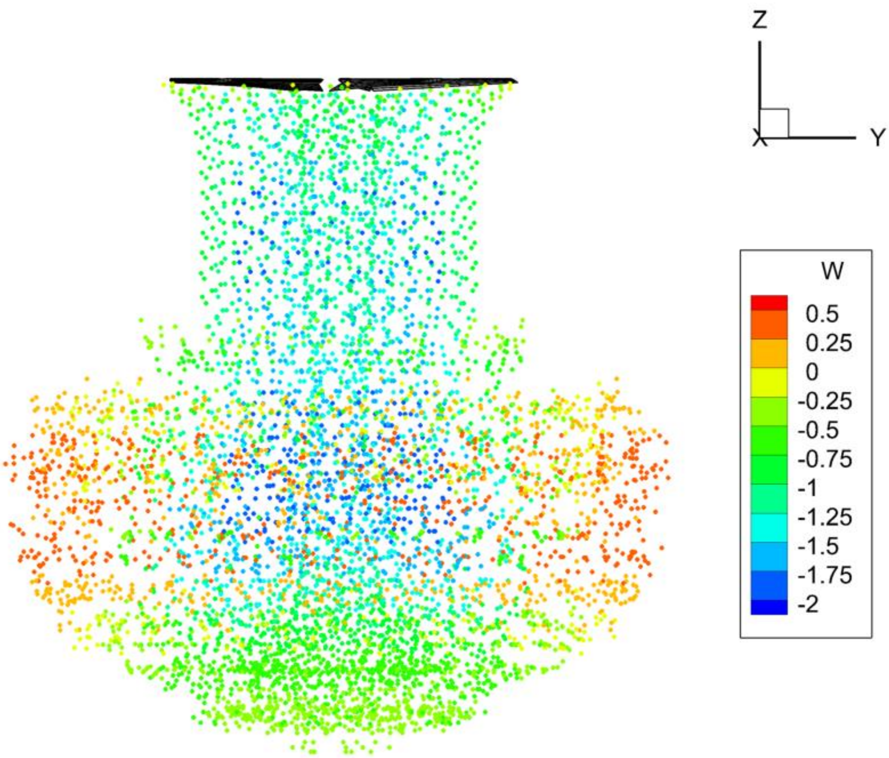

FIGURE 7. 2: Axial-velocity-contoured vorton wake of a 5-bladed propeller in hover flight.

At this point, a 3-second pure tilt motion at 1250 RPM characterised by a 0.20 metre eccentricity has been implemented, according to the E-Pteron geometrical constraints. Short transient aside, which can be considered decayed by a tilt angle of some 7 degrees, the magnitude of the force acting on the propeller is approximately constant. The wake simulated is quite short and thus its development rather unphysical: nonetheless, the choice to cut it off (*nkwts = 100*, *ts = 938*) comes with the need to keep it as steady as possible. In fact, it has been demonstrated that for a longer wake (*nkwts > 120*), an unsafe and breakable situation starts almost at two-thirds of the conversion phase ($t \approx 2\ s$, $\vartheta_t \approx 60\ deg$), when the propeller happens to be working in its own wake, causing noticeable oscillations and a decrease in the force value. At the same time, greater vibrations are expected on the real test case.

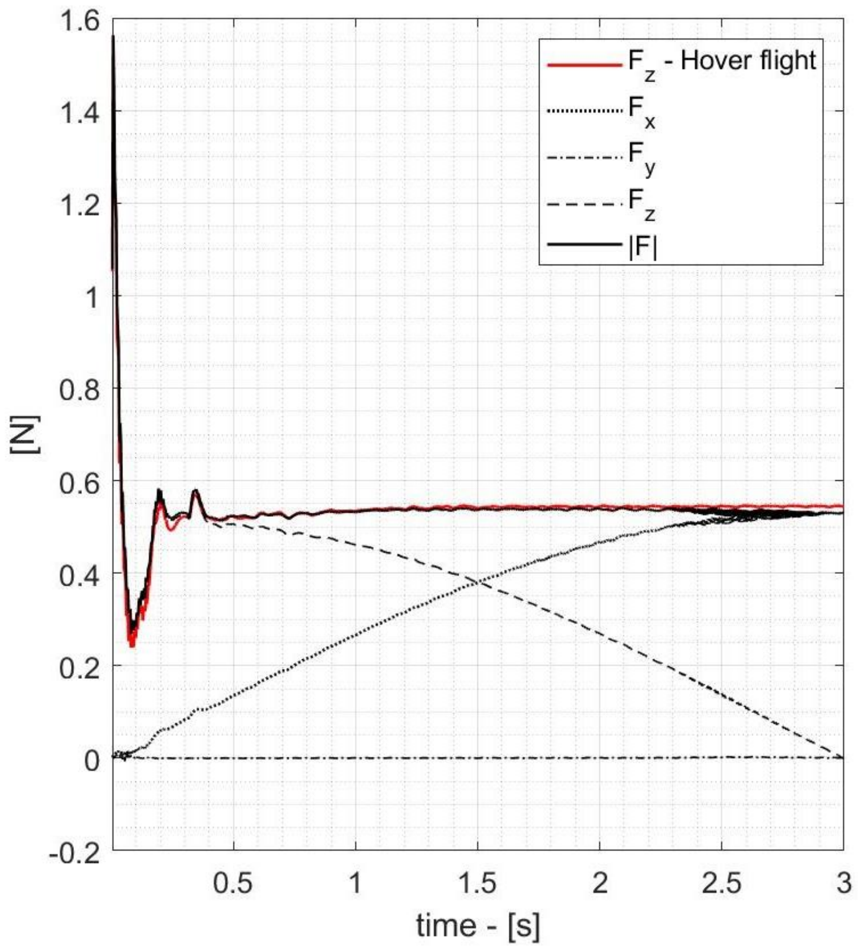

FIGURE 7. 3: Time history of the force components acting on a 5-bladed propeller spinning at 1250 RPM during a 3-second tilting phase (wake cut-off at 100 time steps). Comparison with the axial force during a hover flight simulated at the very same revolutions per minute and same wake truncation.

In the light of these results, it has to be highlighted that this propeller is not suitable for the UAV under examination, implying the need of a design process aimed at the achievement of a blade geometry optimised for the required performances through the Blade Element Momentum Theory.

Going back to the helicopter mode, in hover flight one could suggest that the central rotor assists the tilting propellers generating a thrust roughly amounting to the 60% of the E-Pteron maximum take-off weight, and thus each propeller contributes with a vertical thrust amounting to:

$$T = \frac{30\% \cdot W_{max,TO}}{2} = 0.15 \cdot\ 50\ kg_f = 73.57\ N \qquad 7.1$$

A proposal of inputs for the design process is reported in Table 7. 3.

R	r_{hub}	H	N	Airfoil	V_∞	n	C_l	T
0.16 m	0.04 m	SL	5	NACA 4412	1 m/s	3000 RPM	0.6	73 N

TABLE 7. 3: Design parameters of the Epteron fore propellers: a proposal.

The geometrical parameters are the same as those concerning the generic propeller on which the above-mentioned computations have been performed: blade radius $R = 0.16\ m$, propeller hub radius $r_{hub} = 0.04\ m$ and a number of blades $N = 5$. Then, since the low values of the advanced ratio represent a criticality for the BEMT, the design airspeed V_∞ has been shifted from the hovering 0 m/s to a slow ascent value of 1 m/s. This change implies the presence of a safety margin, since typically, the thrust T is a decreasing function of the airspeed. Similarly, the computed value of the thrust has been rounded to 73 N. Sea level conditions and a constant C_l distribution could be taken into account.

7.4 Ground Roll Test

Another test that could take place in O.M.I.'s hangar – which would be fitting for – involves the system ground roll just after the propeller has concluded the tilt.

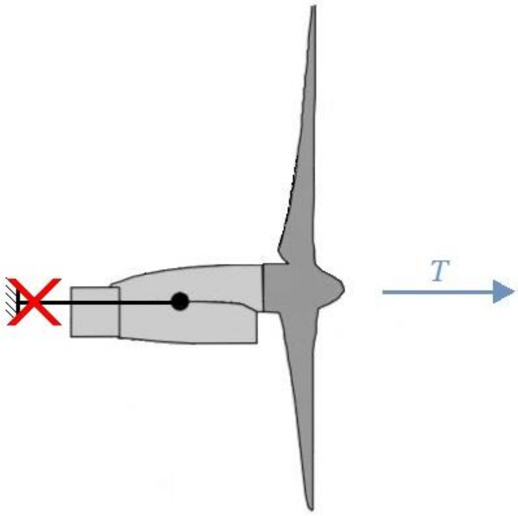

FIGURE 7. 4: Schematisation of a ground roll test.

When the propeller has reached the airplane mode, the brakes that have been keeping the pivot motionless during the tilting phase are removed. In this way, an appraisal of Newton's second law and an evaluation of the take-off run – when the velocities are far lower than those of minimum control of the aircraft surfaces – can be obtained.

CONCLUSIONS

In the context of acceptance of CFD as an equal partner of the wind tunnel and flight tests for the analysis and design of commercial aircraft, it has proven to be processor-intensive, which leads to substantial computational time and modelling cost, not suitable for the actual hardware capabilities in the case of complex configurations. Notwithstanding, panel methods are able to solve – even unsteady – fluid flows around 3-D objects with relative ease, bridging the gap between virtual simulations. That ease comes at a price of stronger basic assumptions (*i.e.* incompressibility and non-viscosity) that reduce the BEM’s flexibility and thus their scope of applicability compared to CFD calculations. Despite this, in some cases those effects are not significant and potential flow solvers reveal to be a useful engineering tool that perform best when modelling fully-attached, high-Reynolds-number, subsonic flows.

In this regard, the purpose of the present thesis was to prove the possibility of exploiting a Vortex Particle Method that stems from panels in order to predict the time evolution of the thrust generated by a V-22 Osprey proprotor digital mock-up while tilting, with and without the presence of the wing acting as an obstacle to the development of the proprotor wake. After having investigated the hover flight on the lookout of the pertaining balance condition between generated thrust and aircraft weight, a target simulation involving the rotation of the proprotor shaft around the wing-wing axis has been performed. Particularly, a virtual bench test has been considered, that is to say that the tilt pivot is motionless in the three-dimensional space hence the free-stream velocity is null. Moreover, the isolated proprotor has been supplemented with the fixed semi-wing to understand how the airframe affects its performance and vice versa. Due to their closeness, a strong interaction between this latter and the proprotor wake occurs, shielding the vortons that float around. As said, since potential methods do not apply to separated flows, three engineering methods have been implemented aiming to an estimation of the drag force acting on the wing – treated as a non-aerodynamic body – due to the propeller action. In a similar manner, when the rough tiltrotor is in airplane mode, the lift distribution over the wing has been computed, just by making use of the solver results, then with no additional assumption. Inherently, considerations about the flight mechanics and the structures have sprung, remarking the successful outcome of employing the VPM in the early stages of the design process of an aircraft.

The present work, far from being complete, is intended to be extended by several future investigations. Firstly, it could be useful to repeat the analyses performed in hover flight for a wider range of angular speeds, in vertical ascent and descent to assess the target tiltrotor performance in helicopter mode. With the aim to draw the flight envelope, other simulations than the bench test ones should be carried out: for this purpose, it could be extremely valuable to equip the potential flow solver with the capability to take into account the dynamic evolution of the object of study.

PaMS DATAIN files

APPENDIX

A

Case: Multibody in hovering flight

```
------------------------------------------------------------------------------------
&RUN     runname="PaMS-simulation"            ver='BS'   &END
------------------------------------------------------------------------------------
&INFTY   velinf(1,1)=0.0         velinf(2,1)=0.0          velinf(3,1)=0.0          &END
&INFTY   omginf(1,1)=0.0         omginf(2,1)=0.0          omginf(3,1)=0.0          &END
&INFTY   density( 1)=1.225       stpress( 1)=0.0          soundsp( 1)=340.3        &END
------------------------------------------------------------------------------------
&TIME   dt=0.0098039215686       tstart=0.0       tend=2.6470588235            &END
&TIME   nsubi=2                                                                 &END
------------------------------------------------------------------------------------
&INVERTER   omegainv=0.0      convinv=1.E-6     maxiter=100                     &END
&INVERTER   maxblkiter=5      nblkmin=1         mfile='Y'                       &END
------------------------------------------------------------------------------------
&CUTOFF    RFF(1)=1.E+9      RFF(2)=1.E+9                                       &END
------------------------------------------------------------------------------------
&BODY    nbody=2        relmot='Y'       symplane=0                             &END
&BODY    cbdgap=0.0                                                             &END
------------------------------------------------------------------------------------
&MOTION    nsubimot=2       onlymot='N'                                         &END
------------------------------------------------------------------------------------
&FILEOUT  fofreq = 1                                                            &END
&FILEOUT  tecplotgp = 'Y'     tecplotpn = 'N'     tecplottm = 'Y'               &END
&FILEOUT  tecpress  = 'N'                         tecpresstm = 'N'              &END
&FILEOUT  tectreff  = 'Y'                         tectrefftm = 'N'              &END
&FILEOUT  patran = 'N'                            patrantm = 'N'                &END
&FILEOUT  vtk ='Y'                                                              &END
&FILEOUT  tecplot3d = 'N'                         tecplot3dtm = 'N'             &END
&FILEOUT  vtk3d = 'N'                                                           &END
&FILEOUT  sfo = 'Y'     sfoname = 'pams.tgz'                                    &END
------------------------------------------------------------------------------------
&OUT3D    out3dcen(1)=0.        out3dcen(2)=0.          out3dcen(3)=1.          &END
&OUT3D    out3ddim(1)=0.25      out3ddim(2)=4.          out3ddim(3)=0.25        &END
&OUT3D    ngpout3d(1)=50        ngpout3d(2)=1           ngpout3d(3)=50          &END
------------------------------------------------------------------------------------


------------------------------------------------------------------------------------
&GEOIN    geoname = "HALF.geo"          icb = 1                                 &END
&GEOIN    orient = +1      orignumb = 'N'     maxang = 60.0                     &END
```

```
&SCALE    sclfac(1) = 0.001    sclfac(2) = 0.001    sclfac(3) = 0.001    &END
&KWAKE    ang = 180.           tmsfac = 1.0         kwnumb = 'N'         &END
&KWAKE    nkwts = 400          nkwtsrig = 0         nkwtspan = 3         &END
&KWAKE    xanru = 0.           yanru = 0.           zanru = 0.           &END
&BC       bctype(1) = 'D'      bctype(2) = 'R'      bctype(3) = 'I'      &END
&BC       bcnvel = 0.0         bcidou = 'N'                              &END
&BCLIM    corerad = 0.3        coremod = 'R'        pt2wknd = 0.         &END
--------------------------------------------------------------------------------
&GEOTRA   GT(1,1)=0.0          GT(1,2)=0.0          GT(1,3)=0.0          &END
&GEOTRA   GT(2,1)=0.0          GT(2,2)=0.0          GT(2,3)=0.0          &END
&GEOTRA   GT(3,1)=0.0          GT(3,2)=0.0          GT(3,3)=0.0          &END
&GEOROT   GR(1,1)=0.0          GR(1,2)=0.0          GR(1,3)=0.0          &END
&GEOROT   GR(2,1)=0.0          GR(2,2)=0.0          GR(2,3)=0.0          &END
&GEOROT   GR(3,1)=0.0          GR(3,2)=0.0          GR(3,3)=0.0          &END
&SYSTRA   ST(1,1)=0.0          ST(1,2)=0.100        ST(1,3)=-0.426       &END
&SYSTRA   ST(2,1)=0.0          ST(2,2)=0.0          ST(2,3)=0.0          &END
&SYSTRA   ST(3,1)=0.0          ST(3,2)=0.0          ST(3,3)=0.0          &END
&SYSROT   SR(1,1)=0.0          SR(1,2)=0.0          SR(1,3)=0.0          &END
&SYSROT   SR(2,1)=0.0          SR(2,2)=0.0          SR(2,3)=0.0          &END
&SYSROT   SR(3,1)=0.0          SR(3,2)=0.0          SR(3,3)=0.0          &END
--------------------------------------------------------------------------------
&GEOIN    geoname = "ROTOREmeno1deg.geo"            icb = 2              &END
&GEOIN    orient = +1          orignumb = 'N'       maxang = 180.0       &END
&SCALE    sclfac(1) = 1.000    sclfac(2) = 1.000    sclfac(3) = 1.000    &END
&KWAKE    ang = 140.           tmsfac = 1.0         kwnumb = 'N'         &END
&KWAKE    nkwts = 400          nkwtsrig = 0         nkwtspan = 3         &END
&KWAKE    xanru = 0.           yanru = 0.           zanru = 0.           &END
&BC       bctype(1) = 'D'      bctype(2) = 'R'      bctype(3) = 'P'      &END
&BC       bcnvel = 0.0         bcidou = 'N'                              &END
&BCLIM    corerad = 0.40       coremod = 'R'        pt2wknd = 0.         &END
--------------------------------------------------------------------------------
&GEOTRA   GT(1,1)=0.0          GT(1,2)=0.0          GT(1,3)=0.0          &END
&GEOTRA   GT(2,1)=0.0          GT(2,2)=0.0          GT(2,3)=0.0          &END
&GEOTRA   GT(3,1)=0.0          GT(3,2)=0.0          GT(3,3)=0.0          &END
&GEOROT   GR(1,1)=0.0          GR(1,2)=0.0          GR(1,3)=0.0          &END
&GEOROT   GR(2,1)=0.0          GR(2,2)=0.0          GR(2,3)=340.0        &END
&GEOROT   GR(3,1)=0.0          GR(3,2)=0.0          GR(3,3)=0.0          &END
&SYSTRA   ST(1,1)=-7.100       ST(1,2)=0.0          ST(1,3)=1.230        &END
&SYSTRA   ST(2,1)=0.0          ST(2,2)=0.0          ST(2,3)=0.0          &END
&SYSTRA   ST(3,1)=0.0          ST(3,2)=0.0          ST(3,3)=0.0          &END
&SYSROT   SR(1,1)=0.0          SR(1,2)=0.0          SR(1,3)=0.0          &END
&SYSROT   SR(2,1)=0.0          SR(2,2)=0.0          SR(2,3)=0.0          &END
&SYSROT   SR(3,1)=0.0          SR(3,2)=0.0          SR(3,3)=0.0          &END
```

APPENDIX B

Case: Multibody in pure tilt motion

```
-------------------------------------------------------------------------------
&RUN     runname="PaMS-simulation"            ver='BS'   &END
-------------------------------------------------------------------------------
&INFTY   velinf(1,1)=0.0       velinf(2,1)=0.0       velinf(3,1)=0.0       &END
&INFTY   omginf(1,1)=0.0       omginf(2,1)=0.0       omginf(3,1)=0.0       &END
&INFTY   density( 1)=1.225     stpress( 1)=0.0       soundsp( 1)=340.3     &END
-------------------------------------------------------------------------------
&TIME   dt=0.009      tstart=0.0      tend=4 &END
&TIME   nsubi=2                                                            &END
-------------------------------------------------------------------------------
&INVERTER   omegainv=0.0     convinv=1.E-6     maxiter=100                 &END
&INVERTER   maxblkiter=5     nblkmin=1         mfile='Y'                   &END
-------------------------------------------------------------------------------
&CUTOFF   RFF(1)=1.E+9     RFF(2)=1.E+9                                    &END
-------------------------------------------------------------------------------
&BODY    nbody=2       relmot='Y'       symplane=0                         &END
&BODY    cbdgap=0.0                                                        &END
-------------------------------------------------------------------------------
&MOTION   nsubimot=2       onlymot='N'                                     &END
-------------------------------------------------------------------------------
&FILEOUT  fofreq = 1                                                       &END
&FILEOUT  tecplotgp = 'Y'    tecplotpn = 'N'    tecplottm = 'Y'            &END
&FILEOUT  tecpress  = 'N'                       tecpresstm = 'N'           &END
&FILEOUT  tectreff  = 'Y'                       tectrefftm = 'N'           &END
&FILEOUT  patran = 'N'                          patrantm = 'N'             &END
&FILEOUT  vtk ='Y'                                                         &END
&FILEOUT  tecplot3d = 'N'                       tecplot3dtm = 'N'          &END
&FILEOUT  vtk3d = 'N'                                                      &END
&FILEOUT  sfo = 'Y'    sfoname = 'pams.tgz'                                &END
-------------------------------------------------------------------------------
&OUT3D   out3dcen(1)=0.       out3dcen(2)=0.       out3dcen(3)=1.          &END
&OUT3D   out3ddim(1)=0.25     out3ddim(2)=4.       out3ddim(3)=0.25        &END
&OUT3D   ngpout3d(1)=50       ngpout3d(2)=1        ngpout3d(3)=50          &END
-------------------------------------------------------------------------------


-------------------------------------------------------------------------------
&GEOIN   geoname = "HALF.geo"          icb = 1                             &END
&GEOIN   orient = +1      orignumb = 'N'     maxang = 60.0                 &END
```

```
&SCALE   sclfac(1) = 0.001   sclfac(2) = 0.001   sclfac(3) = 0.001   &END
&KWAKE   ang = 180.          tmsfac = 1.0        kwnumb = 'N'        &END
&KWAKE   nkwts = 400         nkwtsrig = 0        nkwtspan = 3        &END
&KWAKE   xanru = 0.          yanru = 0.          zanru = 0.          &END
&BC      bctype(1) = 'D'     bctype(2) = 'R'     bctype(3) = 'I'     &END
&BC      bcnvel = 0.0        bcidou = 'N'                            &END
&BCLIM   corerad = 0.3       coremod = 'R'       pt2wknd = 0.        &END
--------------------------------------------------------------------------------
&GEOTRA  GT(1,1)=0.0         GT(1,2)=0.0         GT(1,3)=0.0         &END
&GEOTRA  GT(2,1)=0.0         GT(2,2)=0.0         GT(2,3)=0.0         &END
&GEOTRA  GT(3,1)=0.0         GT(3,2)=0.0         GT(3,3)=0.0         &END
&GEOROT  GR(1,1)=0.0         GR(1,2)=0.0         GR(1,3)=0.0         &END
&GEOROT  GR(2,1)=0.0         GR(2,2)=0.0         GR(2,3)=0.0         &END
&GEOROT  GR(3,1)=0.0         GR(3,2)=0.0         GR(3,3)=0.0         &END
&SYSTRA  ST(1,1)=0.0         ST(1,2)=0.100       ST(1,3)=-0.426      &END
&SYSTRA  ST(2,1)=0.0         ST(2,2)=0.0         ST(2,3)=0.0         &END
&SYSTRA  ST(3,1)=0.0         ST(3,2)=0.0         ST(3,3)=0.0         &END
&SYSROT  SR(1,1)=0.0         SR(1,2)=0.0         SR(1,3)=0.0         &END
&SYSROT  SR(2,1)=0.0         SR(2,2)=0.0         SR(2,3)=0.0         &END
&SYSROT  SR(3,1)=0.0         SR(3,2)=0.0         SR(3,3)=0.0         &END
--------------------------------------------------------------------------------
&GEOIN   geoname = "ROTORE.geo"                  icb = 2             &END
&GEOIN   orient = +1         orignumb = 'N'      maxang = 180.0      &END
&SCALE   sclfac(1) = 1.000   sclfac(2) = 1.000   sclfac(3) = 1.000   &END
&KWAKE   ang = 140.          tmsfac = 1.0        kwnumb = 'N'        &END
&KWAKE   nkwts = 400         nkwtsrig = 0        nkwtspan = 3        &END
&KWAKE   xanru = 0.          yanru = 0.          zanru = 0.          &END
&BC      bctype(1) = 'D'     bctype(2) = 'R'     bctype(3) = 'P'     &END
&BC      bcnvel = 0.0        bcidou = 'N'                            &END
&BCLIM   corerad = 0.40      coremod = 'R'       pt2wknd = 0.        &END
--------------------------------------------------------------------------------
&GEOTRA  GT(1,1)=0.0         GT(1,2)=0.0         GT(1,3)=0.0         &END
&GEOTRA  GT(2,1)=0.0         GT(2,2)=0.0         GT(2,3)=0.0         &END
&GEOTRA  GT(3,1)=0.0         GT(3,2)=0.0         GT(3,3)=0.0         &END
&GEOROT  GR(1,1)=0.0         GR(1,2)=0.0         GR(1,3)=0.0         &END
&GEOROT  GR(2,1)=0.0         GR(2,2)=0.0         GR(2,3)=370.0       &END
&GEOROT  GR(3,1)=0.0         GR(3,2)=0.0         GR(3,3)=0.0         &END
&SYSTRA  ST(1,1)=-7.100      ST(1,2)=0.0         ST(1,3)=1.230       &END
&SYSTRA  ST(2,1)=0.0         ST(2,2)=0.0         ST(2,3)=0.0         &END
&SYSTRA  ST(3,1)=0.0         ST(3,2)=0.0         ST(3,3)=0.0         &END
&SYSROT  SR(1,1)=0.0         SR(1,2)=0.0         SR(1,3)=0.0         &END
&SYSROT  SR(2,1)=3.75        SR(2,2)=0.0         SR(2,3)=0.0         &END
&SYSROT  SR(3,1)=0.0         SR(3,2)=0.0         SR(3,3)=0.0         &END
```

Computer Hardware Specifications

Processor	Intel® Core™ i7-4500U
	CPU @ 1.80GHz, 2.40 GHz – 2 cores, 4 threads
RAM	8.00 GB
System Type	x64-based PC
ROM	500 GB
Graphics Card	NVIDIA GeForce 840M
Resolution	1920 x 1080 x 60 Hz
Bit	32

References

BIBLIOGRAPHY

Abbott, I. H. and A. E. von Doenhoff
[1959] *Theory of wing sections: Including a Summary of Airfoil Data*, Dover Books on Aeronautical Engineering. Dover Publications.

Acree, C. W.
[2012] *Integration of rotor aerodynamic optimization with the conceptual design of a large civil tiltrotor*. Technical Report 562061, NASA Ames Research Center, Moffett Field, California 94035, USA.

Alkemade, F., Nieuwstadt, F.T.M., Van Groesen, E.
[1993] *The vorton method*, Delft University of Technology and University of Twente.

Anderson, J.
[1982] *Fundamentals of Aerodynamics*, McGraw-Hill Book Company.

Apostolo, G.
[1984] *The Illustrated Encyclopedia of Helicopters*, Bonanza, New York.

Balayn, F., Magre, E.
[1999] *Convertible Aircraft with Tilting Rotors*, United States Patent.

Berliner, E.
[1908] *The Berliner Helicopter*, Aeronautics, Vol. 3.

Betz, A.
[1922] *The theory of screw propeller*. NACA Report.

Burrage, R.
[2009] *Tilt-Rotor Aircraft*, United States Patent.

Caccavale, P.
[2006] *Un moderno metodo a potenziale per analisi fluidodinamiche*
DIAS, Università di Napoli Federico II.

Caradonna, F. and C. Tung
[1981] *Experimental and analytical studies of a model helicopter rotor in hover*. NASA Technical Memorandum NASA-TM-81232, NASA.

Chorin, A. J. and P. S. Bernard
[1973] *Discretization of a vortex sheet, with an example of roll-up*. Journal of Computational Physics.

Cottet, G.-H. and P. D. Koumoutsakos
[2000] *Vortex Methods: Theory and Practice*. Cambridge University Press.

De Nicola, C.
[2014] *Appunti per un corso di aerodinamica degli aeromobili.*

Felker, F., Maisel, M., Betzina, M.
[1986] *Full-scale tilt-rotor hover performance*. J Am Helicopter Soc.

Felker, F., Shinoda, P., Heffernan, R., Sheehy, H.
[1990] *Wing Force and Surface Pressure Data from a Hover Test of a 0.658-Scale V-22 Rotor and Wing*. NASA Technical Memorandum 102244.

Froude, R. E.
[1889] *On the part played in propulsion by differences of fluid pressure*. Transactions of the Institution of Naval Architects.

Froude, W.
[1878] *On the elementary relation between pitch, slip and propulsive efficiency*. Transactions of the Institution of Naval Architects.

Gunston, B.
[1983] *Helicopters of the World*, Crescent, New York.

Gustafson, F. B.
[1971] *A History of NACA/NASA Rotating-Wing Aircraft Research, 1915-1970*, American Helicopter Soc., Alexandria, VA.

Hirsch, C.
[2007] *Numerical Computation of Internal and External Flows: Fundamentals of Computational Fluid Dynamics*, 2nd edition.

Johnson, W.
[1994] *Helicopter Theory*. Dover Publications.

Johnson, W.
[2013] *Rotorcraft Aeromechanics*, Cambridge Aerospace Series. Cambridge University Press.

Karen, A.
[2010] *Wing Efficiency for Tilt-Rotor Aircraft*, United States Patent.

Katz, J. and A. Plotkin
[1991] *Low Speed Aerodynamics: from wing theory to panel methods*.

Kellogg, O. D.
[2010] *Foundations of Potential Theory*, Dover Books on Physics. Dover Publications.

Klemin, A.
[1925] *An Introduction to the Helicopter*, NACA TM 340.

Kutta, M. W.
[1902] *Lifting forces in flowing fluids*, Illustrierte Aeronautische Mitteilungen.

Lau, B., Wadcock, A., Heineck, J.
[1997] *Wake visualization of a full-scale tilt rotor in hover*. An American Helicopter Society technical specialists' meeting for rotorcraft acoustics and aerodynamics, VA. Alexandria: AHS International.

Leishman, G.
[2000] *A Hystory of Helicopter Flight*, Cambridge University Press.

Leishman, G.
[2000] *Principles of Helicopter Aerodynamics*, Cambridge University Press.

Leishman, G.
[2007] *Is there a case for the tiltrotor?*, RUSI defence systems.

Losito, V.
[1983] *Fondamenti di aeronautica generale*. Accademia Aeronautica.

Maisel, M. D., D. J. Giulianetti, and D. C. Dugan
[2000] *The History of the XV-15 Tilt Rotor Research Aircraft: From Concept to Flight*, The NASA History Series, NASA SP-2000-4517 edition. Office of Policy and Plans, NASA History Division.

Meola, C. and G. de Felice
[1996] *Fondamenti lineari per la fluidodinamica numerica*.

Montgomerie, B.
[1996] *Drag coefficient distribution on a wing at 90 degrees to the wind*. Technical report, Netherlands Energy Research Foundation.

Monti, R. and R. Savino
[2003] *Aerodinamica*.

Peng, L., Qijun, Z.
[2013] *Calculations on the interaction flow-field and aerodynamic force of tiltrotor/wing in hover*. Acta Aeronaut Astronaut Sin.

Peng, L., Qijun, Z., Qiuxian, Z.
[2015] *CFD calculations on the unsteady aerodynamic characteristics of a tilt-rotor in a conversion mode*, Chinese Society of Aeronautics and Astronautics & Beihang University, Chinese Journal of Aeronautics.

Ross, B.
[2016] *Tiltrotor Aircraft with Inboard Wing Mounted Fixed Engine Arrangement*, United States Patent.

Potsdam, M., Strawn, R.
[2002] *CFD simulation of tiltrotor configurations in hover*. An American helicopter society 58th annual forum. Alexandria: AHS International.

Rajasekaran, J.
[2011] *On the flow characteristics behind a backward-facing step and the design of a new axisymmetric model for their study*. Master's thesis, University of Toronto.

Rankine, W. J. M.
[1865] *On the mechanical principle of the action of propellers*. Transactions of the Institution of Naval Architects.

Rosenstein, H., Clark, R.
[1986] *Aerodynamic Development of the V-22 Tilt Rotor*, Boeing Vertol Company, Philadelphia, USA.

Strickland, J. H. and R. S. Baty
[1994] *A three-dimensional fast solver for arbitrary vorton distributions*. Technical Report SAND93-1641, Sandia National Laboratories.

Strickland, J. H., G. F. Homicz, V. L. Porter, and A. A. Gossler
[2002] *A 3-D vortex code for parachute flow predictions*. Technical Report SAND2002-2174, Sandia National Laboratories.

Tognaccini, R.
[2011] *Lezioni di Aerodinamica dell'Ala Rotante*. Eliche, rotori ed aeromotori.

Warner, E. P.
[1920] *The Problem of the Helicopter*, NACA TN 4.

Willis, D. J.
[2006] *An unsteady, accelerated, high order panel method with vortex particle wakes*. Master's thesis, Massachusetts Institute of Technology.

Wimperis, H. E.
[1926] *The Rotating Wing in Aircraft*, ARC R & M 1108.

Winckelmans, G. S.
[1989] *Topics in vortex methods for the computation of three- and two-dimensional incompressible unsteady flows*. PhD thesis, California Institute of Technology.

Winckelmans, G. S. and A. Leonard
[1993] *Contributions to vortex particle methods for the computation of three-dimensional incompressible unsteady flows*. Journal of Computational Physics.

WEBOGRAPHY

http://www.fluere.it/

https://en.wikipedia.org/wiki/Tiltrotor

https://rotorcraft.arc.nasa.gov/Publications/files/Young_2018_TechMx.pdf

https://en.wikipedia.org/wiki/Bell_Boeing_V-22_Osprey

https://www.globalsecurity.org/military/systems/aircraft/v-22-design.htm

http://www.agustawestland.com/news/aw609-tiltrotor-perform-first-ever-customer-demonstration-flights-heli-expo

https://www.boeing.com/defense/v-22-osprey/

https://bharatshakti.in/tilt-rotor-technology-and-development/

http://halfdome.arc.nasa.gov/Research/Programs/LCTR.html

https://www.britannica.com/science/Navier-Stokes-equation

https://potentialflow.com/definitions

https://www.sciencedirect.com/topics/engineering/panel-method

https://www.researchgate.net/publication/266161455_The_vorton_method_Theory_and_applications_to_fluid_mechanics

https://en.wikipedia.org/wiki/Successive_over-relaxation

http://web.mit.edu/drela/Public/web/xfoil/

http://www.math.nyu.edu/faculty/tabak/vorticity.pdf

ACKNOWLEDGEMENT

Quando ero a Nottingham, gli incontri con persone che - già sapevi - non si sarebbero fermate nella tua vita cominciavano con quattro domande di circostanza, in ordine come da copione: *Come ti chiami? Da dove vieni? Quanti anni hai? Cosa fai nella vita?* Distintamente ne ricordo una che non mostrò lo stesso stupore degli altri, mi chiese: *Qual è il tuo piano B?* Se in quel momento non ho tremato, se anche solo per quell'attimo l'agitazione non mi ha sfiorata, lo devo a voi, mamma, papà, nonna e nonno. Il mio piano A è al sicuro con voi e di uno di riserva non ne ho bisogno. Vi prometto che non mi lascerò travolgere. Sarò imperturbabile.

Grazie a te Berry mio, sei ispirazione ed energia positiva.

To my Resnicks. Our paths crossed in the darkest period of my life, you met the worst version of me and nonetheless you are still by my side. I am extremely grateful for your unconditional love; never will I forget what you have done for me.

Grazie Rossella e Francesca per i vostri consigli sinceri.

A Mariangela e Lucia Brac, la magistrale non è stata la stessa senza di voi.

A Paolo e alle virate illegali.

Grazie a Marco, a Nunzio e ai vostri padri, siete amici veri su cui posso contare.

A Paqo, Giuseppe, Francesco e Gigante. Grazie, siete stati angeli custodi e fonte superlativa di confronto.

Infine, vorrei ringraziare il prof. de Nicola per la sua consueta professionalità, per lo sprone, ma soprattutto per i rimproveri. Grazie per aver fatto orbitare attorno a questo lavoro una squadra di professionisti eccezionali: l’Ing. Piccolo, l’Ing. Di Giorgio e il Dott. Giuliani. Un ringraziamento particolare al Dott. Caccavale per la pazienza e il tempo dedicatomi.